UC Irvine

UC Irvine Electronic Theses and Dissertations

Title

Insights into the Molecular and Epigenetic Mechanisms Involved in Tissue Regeneration and Infections

Permalink

https://escholarship.org/uc/item/9cj4d4s6

Author

Urban, Lauren Ashley

Publication Date

2022

Copyright Information

This work is made available under the terms of a Creative Commons Attribution License, available at https://creativecommons.org/licenses/by/4.0/

Peer reviewed|Thesis/dissertation

eScholarship.org Powered by the California Digital Library
University of California

UNIVERSITY OF CALIFORNIA,
IRVINE

“Insights into the Molecular and Epigenetic Mechanisms Involved in Tissue Regeneration and Infections”

DISSERTATION

submitted in partial satisfaction of the requirements
for the degree of

DOCTOR OF PHILOSOPHY

in Microbiology & Molecular Genetics

by

Lauren Ashley Urban

Dissertation Committee:
Associate Professor Timothy Downing, co-Chair
Associate Professor Albert Siryaporn, co-Chair
Professor Michael McClelland
Assistant Professor Rosa Andrade
Assistant Professor Trina Norden-Krichmar

2023

Figure in Introduction © 2020 Wiley Online Library
Chapter 2 © 2021 Elsevier
Chapter 3 of this dissertation will be published in Advanced Biology in 2023 with the same title. The text is used in this dissertation with permission from Wiley Online Library
© 2023 Lauren Ashley Urban

DEDICATION

I dedicate this dissertation to my family, amazing friends (Hemisha Bhatpuria, Hannah Blumberg, Heena Gupta, John Le, Gina Vento, Sarah Wright & Waamene Yowika), and wonderful partner, John Carmack. Thank you for your love and support throughout my life and during my Ph.D. I am inspired by your kindness, passion, and wisdom, and I thank God for putting each of you in my life. Thank you to the staff, professors, and peers who helped me along the way – your kindness truly made a difference in my life, and I will pass it forward to those I meet in the future. I wanted to share some quotes that helped me during the hardest times of my life:

"*No matter what gets done and how much is left undone, I am enough. Yes, I am imperfect and vulnerable and sometimes afraid, but that doesn't change the truth that I am also brave and worthy of love and belonging*".
(Brene Brown, The Gifts of Imperfection).

"*I am driven by two main philosophies, know more today about the world than I knew yesterday. And lessen the suffering of others. You'd be surprised how far that gets you*."
(Neil Degrasse Tyson)

"*The function of mindfulness is, first, to recognize the suffering and then to take care of the suffering. The work of mindfulness is first to recognize the suffering and second to embrace it. A mother taking care of a crying baby naturally will take the child into her arms without suppressing, judging it, or ignoring the crying. Mindfulness is like that mother, recognizing and embracing suffering without judgement.*

So the practice is not to fight or suppress the feeling, but rather to cradle it with a lot of tenderness. When a mother embraces her child, that energy of tenderness begins to penetrate into the body of the child. Even if the mother doesn't understand at first why the child is suffering and she needs some time to find out what the difficulty is, just her action of taking the child into her arms with tenderness can already bring relief. If we can recognize and cradle the suffering while we breathe mindfully, there is relief already."
(Thích Nhất Hạnh, No Mud, No Lotus: The Art of Transforming Suffering)

"*This is my commandment, that you love one another as I have loved you."*
(John 15:12)

TABLE OF CONTENTS

LIST OF FIGURES

LIST OF TABLES

ACKNOWLEDGEMENTS

I would like to express the deepest appreciation to my committee co-chairs, Dr. Timothy Downing and Dr. Albert Siryaporn for their support during my PhD studies. I would like to thank my committee members, Dr. Michael McClelland, Dr. Rosa Andrade, and Dr. Trina Norden-Krichmar who have helped me improve my dissertation work and refine my thesis project. I would also like to thank Dr. Ilona Foik for her guidance and mentorship in my research and for her continued support for our neutrophil-*fro* project even in the middle of the COVID-19 pandemic. I will always be grateful for support during my PhD work and scientific research. It has been an amazing opportunity to have access to these wonderful science mentors.

I thank the Wiley Online Library for permission to include a copyrighted figure and Human Protein Atlas for permission to include histological images as part of my thesis/dissertation. I also thank Elsevier for permission to include Chapter 2 of my dissertation, which was originally published in Trends in Immunology. Financial support was provided by the University of California, Irvine, the Stanley Brehens Fellowship, and the ARCS foundation.

Aging-related inflammation associated with loss of DNA methylation. Chapter 2 is a minimally modified reprint of the published work: Urban, Lauren A et al. “The impact of age-related hypomethylated DNA on immune signaling upon cellular demise.” *Trends in immunology* vol. 42,6 (2021): 464-468. doi:10.1016/j.it.2021.04.005. This article was published in *Trends in immunology* vol. 42,6, Urban LA, Trinh A, Pearlman E, Siryaporn A, Downing TL. The impact of age-related hypomethylated DNA on immune signaling upon cellular demise, 464-468, Copyright Elsevier (2021).

DNA methylation dynamics during esophageal regeneration following surgical repair with acellular graft implants in rats. Chapter 3 is a minimally modified reprint of material formally committed to future publication in *Advanced Biology*. I would like to acknowledge my co-authors, and especially, the lab of Dr. Josh Mauney for overseeing and performing the animal experiments.

Bacterial-sensing of hypochlorous acid from stimulated neutrophils. Chapter 5 is a reprint of material that is part of an article under preparation. The co-author listed in this publication, Ilona Foik, directed and supervised research which forms the basis for the thesis/dissertation. I thank Albert Siryaporn and the Gitai lab for their inspiring previous work that identified the flow-sensor *fro* in *P. aeruginosa* and creation of a Δ*froR* mutant. I would like to acknowledge my co-author, Ilona Foik, for her contribution to the experimental work and valuable mentorship during my PhD studies. I am very grateful to Andy Huang who performed follow-up experiments in the lab during the COVID-19 pandemic. I would also like to thank Runhang Shu and Leora Duong who will be performing additional experiments for this project including RNA-seq analysis and *in vivo* wound experiments. https://www.biorxiv.org/content/10.1101/2022.02.01.478687v1

VITA
Lauren Ashley Urban

EDUCATION & WORK EXPERIENCE

B.S. in Biophysics, Brown University 2015
Alan & Marianne Schwartz Brown Annual Scholarship Recipient
Brown University Scholarship Recipient

Senior Research Associate, Gerson Lehrman Group 2015-2017

Ph.D. in Microbiology & Molecular Genetics, University of California, Irvine 2023
Recipient of the Biological Sciences Dean's Graduate Fellowship Award
Recipient of Stanley Behrens Fellowship Award

FIELD OF STUDY

Microbiology, epigenetics, innate immunology, bacterial infections, bioinformatics

PUBLICATIONS

Foik, IP, and Urban, LA, et al. Activation of a bacterial flow sensor by stimulated neutrophils (manuscript in preparation). https://doi.org/10.1101/2022.02.01.478687

Urban, LA. et al. DNA methylation dynamics during esophageal epithelial regeneration following repair with acellular silk fibroin grafts in rat. *Advanced Biology*. (manuscript accepted for publication)

Urban et al. "The impact of age-related hypomethylated DNA on immune signaling upon cellular demise." *Trends in immunology*. vol. 42,6 (2021): 464-468. https://doi.org/10.1016/j.it.2021.04.005

Doolin et al. "Mammalian histones facilitate antimicrobial synergy by disrupting the bacterial proton gradient and chromosome organization." *Nature communications*. vol.11,1 (2020): 3888.4. https://doi.org/10.1016/j.it.2021.04.005

ABSTRACT OF THE DISSERTATION

"Insights into the Molecular and Epigenetic Mechanisms Involved in Tissue Regeneration and Infections"

By

Lauren Ashley Urban

Doctor of Philosophy in Microbiology & Molecular Genetics

University of California, Irvine, 2023

Professor Timothy Downing, co-Chair

Assistant Professor Albert Siryaporn, co-Chair

Thousands of patients require esophageal replacement annually. While immune activation is critical for wound-healing processes and tissue regeneration, chronic non-resolving inflammation can cause fibrosis, tissue damage, and disease. Given recent evidence that immune regulation becomes dysfunctional with aging, there is a vital need to better understand the host immune responses involved in tissue regeneration and inflammation. Previous studies identified signaling pathways involved in tissue regeneration with acellular graft implants such as the phosphatidylinositol 3-kinase (PI3K), protein kinase B (Akt), and hepatocyte growth factor receptor (c-MET) signaling pathways. However, whether and how epigenetic mechanisms influence tissue regeneration has not been studied. A better understanding of the epigenetic mechanisms involved in regeneration and how they are connected to disease can help identify novel therapeutic targets and improve our ability to determine when these biological systems have gone awry.

In chapter 2, we discuss a potential novel mechanism for how the loss of DNA methylation during aging could contribute to immune dysfunction through a novel analysis of previously published epigenetic data and a review of the literature. In chapter 3, we characterized DNA methylation dynamics during tissue regeneration and present novel findings that suggest epigenetic mechanisms influence key signaling pathways involved in growth, inhibition of apoptosis, and immune activation in regenerating esophageal epithelial tissues. Our results showed that hypomethylation of CpGs occurs within the promoters of genes associated with immune activation, while hypermethylation of CpGs occurs in the promoters of genes involved in PI3K-Akt activation.

Taken together, the findings in chapter 2 and chapter 3 provide insights into how epigenetics changes are important regulators of immune responses and may influence immune dysfunction during aging when cells exhibit a notable loss in regenerative potential. The results of this work can help identify novel opportunities to improve the efficacy of biomedical implants by manipulating epigenetic mechanisms involved in immune activation to promote wound healing and tissue regeneration.

Finally, in chapter 4, we discuss findings from a collaborative project that showed the gram-negative bacteria, *Pseudomonas aeruginosa*, responds to the presence of stimulated neutrophils by activating the *fro* system, which regulates the expression of antioxidative genes to mitigate the bactericidal effects of HOCl. Our results suggest that *fro* activation could function as a bacterial defense mechanism against a neutrophil attack mechanism which could promote colonization in human tissues.

Chapter 1

Introduction

1.1 Epigenetics and DNA methylation

Epigenetics describes the set of reversible chemical modifications that influence the expression of genes inside cells which do not involve alterations in the DNA sequence [1]. The main epigenetic mechanisms include DNA methylation, histone modifications, and noncoding RNA. DNA methylation is one of the best-studied epigenetic modifications in eukaryotes in which a methyl group is covalently added to a cytosine and occurs most frequently in regions of DNA where a cytosine is followed by a guanine (CpG) [1]. Numerous studies have investigated how these epigenetic modifications regulate gene expression during cellular processes including stem cell renewal, differentiation, and regeneration [2].

Previous studies have found that epigenetic dynamics contribute to wound healing and regenerative processes following graft implantation. Previous research found a critical role for DNMT3a in regulating T cell alloreactivity and revealing pathways that control T cell tolerance in acute graft-versus-host disease (aGVHD). De novo DNA methylation by DNMT3a has been shown to control early effector T-cell fate decisions following activation and DNMT3a activation is required for effector T cells differentiation [3]. There is evidence that the hypomethylating agent azacitidine (AzaC) can be used to mitigate systemic inflammatory in acute graft-versus-host disease (aGVHD) in both murine preclinical transplant models and in human clinical trials [4,5]. Hypomethylation corresponded with changes in gene expression in several pathways of

T cell signaling and differentiation and reduced disease severity and improved survival in aGVHD [6].

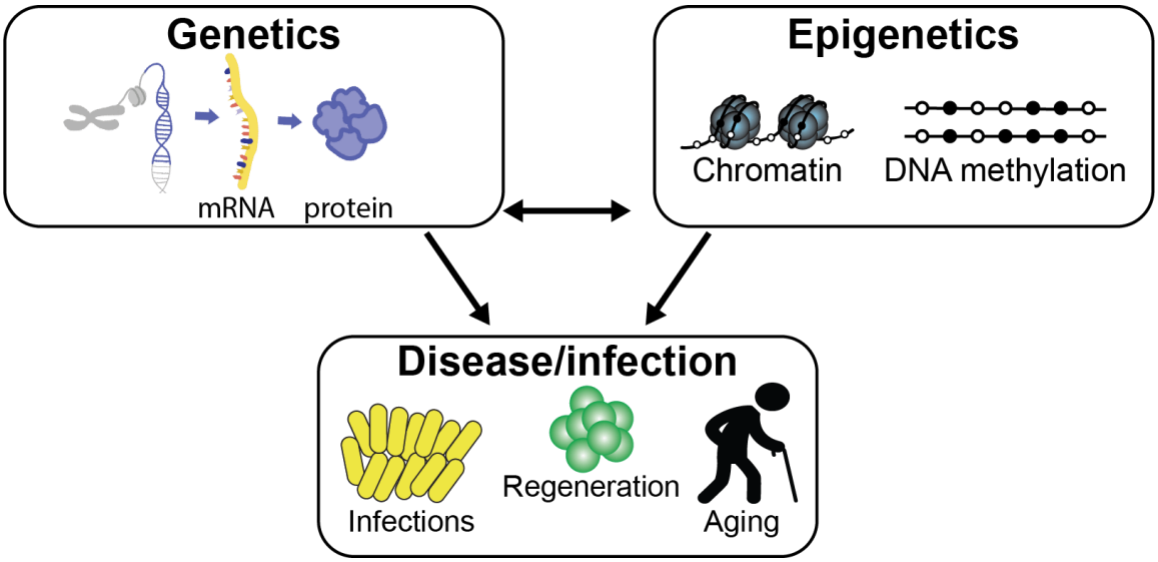

Figure 1: Schematic diagram representing the genetic-epigenetic interaction and its impact on human health. Genetics and epigenetics play a role in diseases and infections. Epigenetic changes during aging may contribute to disease and the loss of regenerative potential in aged tissues.

Anatomy of the esophagus and esophageal diseases

The esophagus is a multi-layered tube that is lined by a stratified squamous epithelial that helps protect the underlying tissue from food abrasion, acidity, and invading pathogens [7] (Fig. 2). The esophagus is composed of four layers (proximal to distal): the mucosa, submucosa, muscularis propria, and tunica adventitia. The mucosal layer is composed of stratified squamous nonkeratinized epithelium [7]. Basal cells in the mucosa are responsible for cell proliferation and differentiation of daughter cells which migrate to and repopulate the native tissue architecture after injury [8]. The submucosa contains loose connective tissue, small blood vessels, and lymphocytes. Next, the muscularis propria is composed of muscle fibers. The outer layer of the esophagus is the tunica adventitia which is composed of connective tissue that covers

the esophagus and connects it with neighboring structures [7]. Patients with malignancies or congenital disorders of the esophagus, such as Barrett's esophagus and atresia, require surgical reconstruction of tubular esophageal segments with graft implants to restore tissue function [9–12].

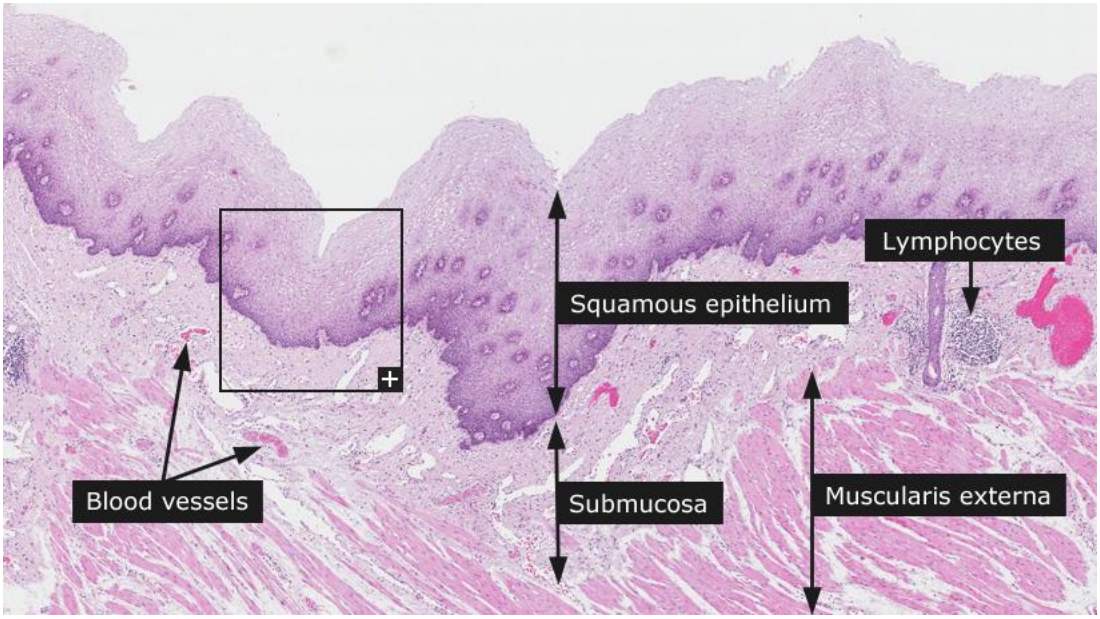

Figure 2: Histological image of the human esophagus. Image credit: Human Protein Atlas. Image available from https://v15.proteinatlas.org/learn/dictionary/normal/esophagus.

Barrett's esophagus (BE) is a condition where the normal stratified squamous esophageal epithelium is replaced by the specialized intestinal epithelium. BE is the only known precursor for esophageal adenocarcinoma (EAC). The incidence of EAC is rising in Western countries. Epigenetic studies found global methylation changes in eosinophilic esophagitis [13], BE and ECA [14] esophagus tissues compared to normal squamous esophagus tissues**.** The loss of DNAme at a CpG island associated with the activation of oncogene PIK3CA expression, which encodes a catalytic subunit of PI3K, is thought to play a part in activating the PI3K/Akt pathway and contributing to tumorigenesis in esophageal cancer patients [15]. It has been found that epigenetic

profiles differ across subclasses of EAC tumors which corresponds to variable phenotypic, clinical behaviors, and therapeutic targets [16]. Notably, gene set enrichment analysis (GSEA) of differentially methylated CpGs among the BE, BE with high-grade dysplasia, ECA, and normal squamous esophagus revealed an enrichment in KEGG pathways such MAPK, neurotropin, and VEGF signaling pathways, and GO terms such as locomotory behavior, regulation of cell size, regulation of cell growth, and response to molecule of bacterial origin. KEGG [14]. The involvement of DNAme in these pathways, which are also essential to regenerative and wound healing responses [17–19], alludes to the potential role of DNAme in facilitating cell fate and lineage decisions in esophageal neotissues.

Tissue-engineered silk-fibroin graft implants

Silk fibroin (SF) is a fibrous protein obtained primarily from Bombyx mori cocoons that can be isolated and used for biomedical applications such as tissue engineering, skin grafts, and implantable biomaterials since the 1990s [20]. Numerous studies have demonstrated that SF biomaterials have excellent biocompatibility and are degraded *in vivo* by host proteases which allow host cells to repopulate the wound which promotes tissue homeostasis and function [21]. Recent studies have found that SF implants improve tissue regeneration following surgical repair in porcine and rat models [22,23], and SF implants were shown to improve survival in a rat model of abdominal aortic replacement compared to expanded polytetrafluoroethylene control grafts [24]. How do SF grafts promote tissue regeneration? Previous work demonstrated that SF grafts induce the expression of cyclin D1, vimentin, fibronectin, and Vascular endothelial growth factor (VEGF) which are important for cell growth [22]. Previous work found that

the wound healing processes induced by SF grafts are dependent on Nuclear factor kappa B (NF-κB) activation [25]. Inhibition of NF-κB by a pharmacological inhibitor Bay 11-7082 or knockdown of NF-κB using siRNA of IκB kinase alpha (IKKα) and IκB kinase beta (IKKβ) inhibited SF-induced wound healing processes [25].

Immune responses shapes non-resolving verses resolving inflammation

The immune system plays a critical role in tissue regeneration. Upon injury, innate immune cells such as circulating monocytes and neutrophils are rapidly recruited to the site of injury [26]. Studies have found that the innate immune response induced within the first week of surgery plays a critical role in tissue regeneration and wound healing processes [27,28]. The early immune response depends primarily on macrophages which can be polarized into pro-inflammatory (M1) or wound healing (M2) phenotypes depending on environmental cues such as substrate stiffness and soluble mediators (cytokines and chemokines) [29,30] (Table 1). This process of changing the cell phenotype in response to environmental stimuli is termed reprogramming.

Biomedical implants has been local inflammatory phenomena known as the foreign body reaction (FBR) which occurs whenever a foreign material is implanted into the body [31]. Macrophages are considered the primary regulators of FBR and wound healing processes. Studies have showed that SF implants induce a mild inflammatory response, macrophage activation, and FBR that can last for several weeks or months *in vivo* [32,33]. Previous studies have identified several important signaling pathways involved in the differentiation and polarization of macrophages, such as interferon-regulatory factors (IRFs) and Akt kinases [34–36]. The balance of M1 versus M2 macrophages is a strong predictor of medical outcomes.

	M1 Macrophages	M2 Macrophages
Activators	IFN-γ, LPS, GMCSF, TLR4	IL-4, IL-10, IL-13
Markers	HLA-DR, CD11c, CD86, iNOS, pSTAT1	CD163, CD204, CD206, VEGF
Upregulates	IL-1β, IL-6, TNF-α	IL-10, IL-4, TGF-β
Functions	Inflammation, killing pathogens, anti-tumoral	Wound healing, tissue regeneration

Table 1: Macrophage polarization. Abbreviations: IFN-γ, Lipopolysaccharides (LPS), Granulocyte-macrophage colony-stimulating factor (GMCSF), Toll-like receptor 4 (TLR4), Major histocompatibility complex (MHC) II cell surface receptor (HLA-DR), Cluster of Differentiation 11c (CD11c), Cluster of Differentiation 86 (CD86), Inducible nitric oxide synthase (iNOS), phosphorylated signal transducer and activator of transcription 1 (pSTAT1), Interleukin 1-beta (IL-1β), Interleukin 6 (IL-6), Tumour necrosis factor alpha (TNF-α), Interleukin 4 (IL-4), Interleukin 10 (IL-10), Interleukin 13 (IL-13), Cluster of Differentiation 163 (CD163), Cluster of Differentiation 204 (CD204), Cluster of Differentiation 206 (CD206), Vascular endothelial growth factor (VEGF), Interleukin 4 (IL-4), Transforming growth factor beta (TGF-β).

Immune responses to biomedical implants

Following surgical injury, macrophages are initially classically activated (M1) and secrets pro-inflammatory cytokines, such as IL-1β, IL-6, and TNF-α and chemokines to recruit additional immune cells [37]. After several days or weeks, macrophages are polarized towards a wound-healing (M2) phenotype and secrete IL-10, IL-4, and TGF-β that promote matrix remodeling and angiogenesis [27]. Macrophages and dendritic cells secrete cytokines and chemokines which influence adaptive immune responses in the proliferation and remodeling phases of tissue regeneration (Fig. 3). Thymus-derived (T) lymphocytes can be polarized into either Th1 or Th2 effector subsets. Th1 effector cells secrete pro-inflammatory cytokines, such as IFN-γ, TNF-α, and IL-2, that stimulate macrophages, natural killer cells, and CD8+ cytotoxic T cells. Th2 effectors secrete IL-4 which is required for Th2 differentiation and inhibits Th1 cell-specific factors [37].

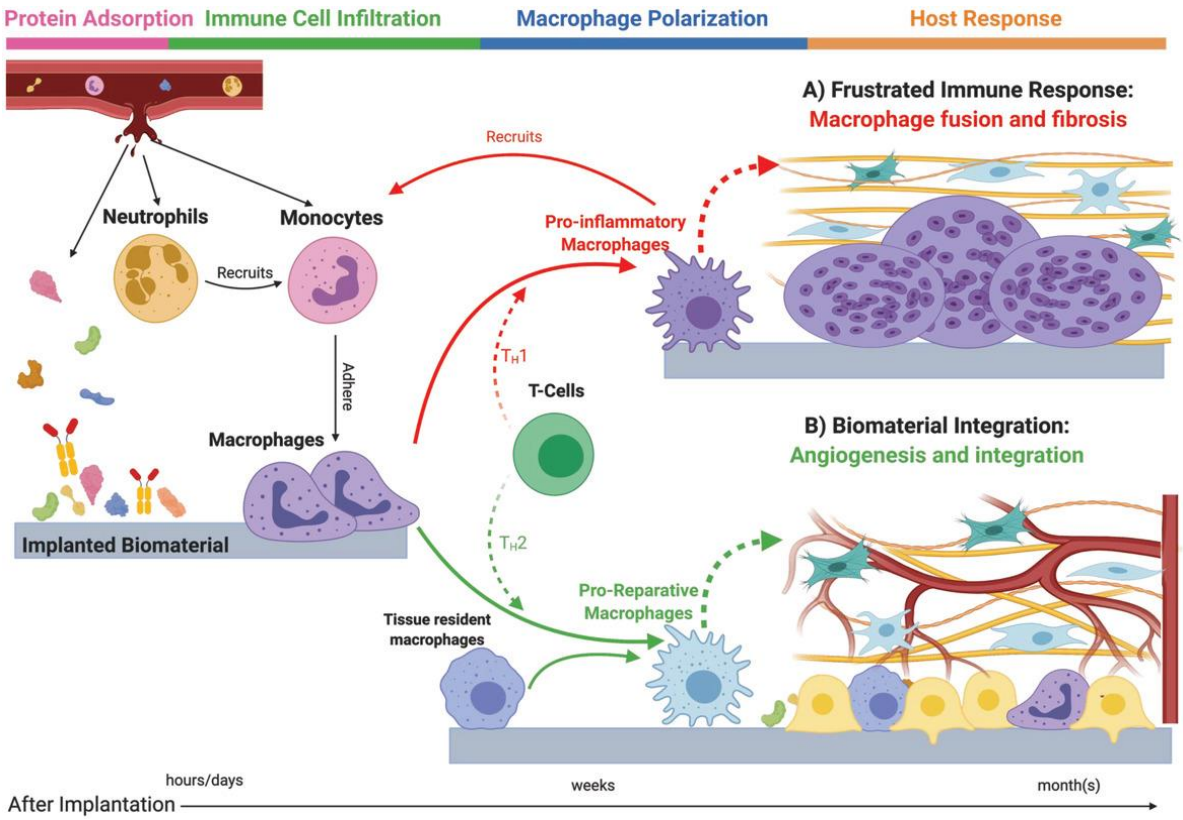

Figure 3: Schematic diagram of the immune response following biomedical implantation. Plasma proteins adhere to biomedical implant. Circulating monocytes and neutrophils are first recruited to the implant site and secrete chemokines and cytokines. Macrophages can be polarized into M1 or M2 phenotypes and influence downstream adaptive immune response mediated by T-cells. Th1 cells secrete pro-inflammatory cytokines and stimulate macrophages. Th2 cells suppress Th1 polarization and contribute to wound healing and tissue regeneration processes. Reproduced with permission [37]. Copyright 2020, Wiley Online Library.

P. aeruginosa infections

P. aeruginosa is a gram-negative opportunistic bacterial pathogen and one of the leading causes of hospital-acquired infections (HAIs) and infections in immunocompromised patients. The WHO reported that HAIs are a major cause of morbidity, mortality, and financial costs due to prolonged hospital stays and treatments. Approximately 1 in 20 patients acquire infections in hospitals which results in millions of HAIs every year. Reports by European Centre for Disease Prevention and Control

(ECDC) showed that the cumulative burden, as estimated in disability-adjusted-life-years (DALY), associated with HAIs was higher than that of all other communicable diseases [38,39]. Several studies have found a strongly correlated between medical implant failure rates and patient age. Evidence suggests that chronic inflammation and HAIs are the leading causes of implant failure and tissue damage [39–41].

Chapter 2

Aging-related inflammation associated with loss of DNA methylation

2.1 Aging is associated with immune system dysfunction

Aging is associated with decreased antigen-specific immunity and increased chronic inflammation. While DNA-sensing pathways might be involved, the molecular factors underlying these age-related aberrancies in immune signaling are unclear. Here, we consider the potential role of aging-induced hypomethylated DNA as a putative stimulant of age-associated inflammation. Emerging evidence from pathology, epidemiology, and animal studies conducted in mice, rats, and non-human primates alludes to a close relationship between aging and immune dysregulation [42,43]. However, the molecular underpinnings behind this relationship remain a mystery. A better understanding of how aging contributes to inflammation is needed to ideally improve the treatment and diagnosis of age-related diseases (ARDs) such as cancer, rheumatoid arthritis, and Alzheimer's disease (AD).

While advances in DNA sequencing have shown that age-dependent epigenetic changes can impact gene regulation, there is little understanding of how these altered epigenetic patterns may impact cells of the mammalian immune system when nuclear DNA and chromatin are released into the extracellular space upon cellular demise. In this forum article, we provide a perspective on how hypomethylated DNA, arising during aging, can stimulate the immune system by activating immune receptors thought to be involved in detecting foreign (viral and bacterial) DNA. We discuss evidence supporting

the hypothesis that aged hypomethylated DNA might be immunogenic and perhaps act as an overlooked, but key regulator of immune signaling during aging.

2.2 Misplaced self-molecules can activate immune responses following cell death

The mammalian immune system recognizes molecular patterns indicative of infection, injury, or tissue dysfunction through a common set of pattern recognition receptors (PRRs)**,** which detect conserved molecular structures known as pathogen-associated molecular patterns (PAMPS) and damage-associated molecular patterns (DAMPs)**.** Recently, the term DAMPs was expanded to include self-derived biomolecules that are damaged, misfolded, or displaced into the extracellular space, collectively termed 'altered or misplaced self-molecules' [44]. While cellular repair and protein degradation mechanisms exist to combat molecular damage to DNA, proteins, and lipids, a key feature of aging is the accumulation of altered and misplaced self-derived molecules due to an aging-dependent decline of such molecular pathways [44].

In addition, a decline in proteolytic activity is also observed in aged cells; this results in impaired autophagy and efferocytosis [42,44]. Defects in autophagy are linked to accelerated aging phenotypes and several ARDs, including AD and age-related retinal degeneration [3]. Inefficiently cleared apoptotic cells (ACs) arising during impaired efferocytosis undergo secondary necrosis, releasing intracellular DAMPs into the extracellular space [e.g., nuclear DNA, high mobility group-box 1 (HMGB1) protein, mitochondrial DNA (mtDNA), and chromatin] [45,46]. As mtDNA has been shown to be lowly methylated [47] and to prime the antiviral innate immune response in mice upon cytosolic escape [45], it is plausible that aged hypomethylated nuclear DNA might also be a key contributor to inflammation during aging. The disposal of cell debris and

damaged organelles slows down during aging in tandem with the accumulation of high amounts of altered and misfolded proteins within aged cells [44]. In this scenario, the tissue-specific 'education' received by immune cells [48] following the release of endogenous material from young cells early in an organism's life may not be compatible to carry out immune surveillance during advanced aging (Fig. 4A). If the 'rules' for healthy maintenance of the organism grow outdated with age and the immune system fails to adapt, the result might resemble the chronic low-grade inflammatory state typically observed during aging [44].

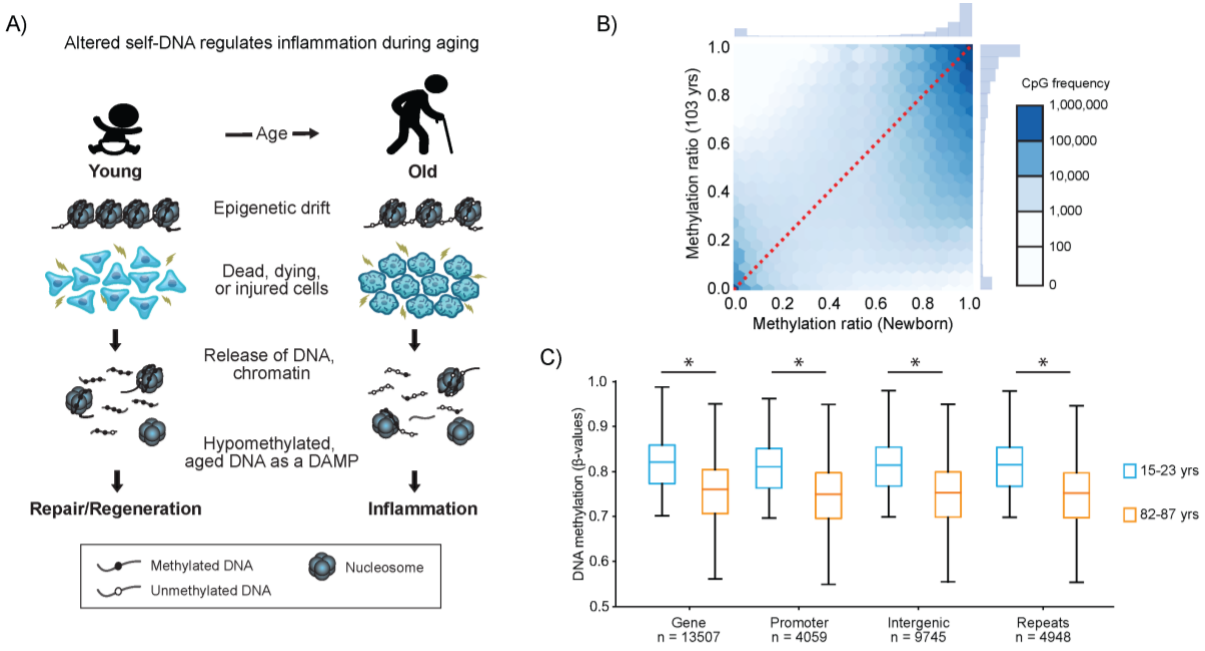

Figure 4. Aging is associated with global DNA hypomethylation. (A) Schematic illustrating the "altered self" hypothesis. DNA methylation patterns progressively diverge across the genome from highly conserved postnatal patterns over a lifetime due to a phenomenon known as epigenetic drift. The aged epigenome is characterized by deviations in global DNA methylation patterns and global DNA hypomethylation. These aging-associated epigenetic changes may generate "altered self" molecules such as unmethylated DNA and chromatin fragments that are released into the extracellular space when cells die or are stressed. During aging, higher levels of unmethylated genomic DNA fragments may stimulate PRRs and contribute to chronic inflammation seen in elderly populations. (B) Whole Genome Bisulfite Sequencing of a newborn (NB) and a centenarian (Y103) individual. Illustrative CpG methylation levels (%) of 9,272,050 CpGs in the DNA from newborn (NB) and centenarian sample (Y103) from

GEO Accession GSE31438. (C) Methylation levels are quantified as Beta-values (i.e. ratio of intensities of methylation and unmethylated alleles). Boxplots show average ß-values across four genomic features (promoters, exons, introns, and intergenic regions) from twenty-four samples. DNA methylation at 476,366 sites throughout the genome of white blood cells from two cohorts ranging in age from 15 to 23 years old (n=12) and 82 to 87 years old (n=12). Methylation array data from GEO Accession GSE87571.

2.3 Age-related epigenetic drift and the 'altered self' hypothesis

Epigenetics describes the set of reversible chemical modifications that govern the functional use of genetic information. Our cells' ability to maintain epigenetic patterns also declines over a lifetime, resulting in epigenetic drift. Here, we propose a potential role for age-related DNA hypomethylation in generating altered self-DNA molecules that can stimulate PRRs when released during cell death. In mammalian genomes, methylation commonly occurs in a CpG dinucleotide context. Several reports have found genome-wide losses in CpG methylation during aging (Fig. 4B-C, shown for illustration purposes), most notably at repetitive DNA sequences [49,50]. As DNA methylation is known to contribute to key transposon-silencing mechanisms, hypomethylation at substantially CpG-dense transposable elements (TEs) can trigger reactivation of TEs and subsequent aberrant activation of immune signaling pathways [43,51]. Reactivation of TEs due to epigenetic drift was previously observed in a study reporting the reactivation of TEs in human fibroblasts passaged until cellular senescence, leading to the accumulation of cytoplasmic DNA, and the direct activation of type I interferon signaling in these cells [51]. Given the high occurrence of repetitive elements across mammalian genomes, changes in methylation in these regions would generate high numbers of unmethylated DNA fragments with highly conserved sequence motifs, potentially rendering them strong candidates for proinflammatory biomolecules during aging (Fig 4B-C, shown for illustration purposes) [49,50]. In the

case of retrotransposons, it is possible that the amplification of transposable sequences might exacerbate the downstream effects of released unmethylated DNA on immune signaling, although this remains speculative. Indeed, it will be interesting to further explore this idea by comparing retrotransposon expression amounts between cells from young and aged individuals.

2.4 Widespread loss of cytosine methylation can increase DNA immunogenicity

CpG methylation, a common feature of mammalian genomes, is largely absent in immunogenic bacterial and viral DNA. During aging, the loss of CpG DNA methylation in genomic DNA may generate unmethylated DNA fragments that can trigger PRR activation in phagocytes during AC clearance, including Toll-like receptor 9 (TLR9) [52]. As discussed, phagocytes dispose of ACs via noninflammatory efferocytosis. One report indicated that DNA methylation regulated the suppressive versus inflammatory responses of dendritic cells (DCs) during AC efferocytosis [53]. It is known that phagocytes secrete wound-healing cytokines such as TGF-β during the disposal of ACs. However, upon treatment of ACs with the global demethylating agent 5-azacytidine, hypomethylated ACs induced inflammatory IL-6 signaling in mouse DCs. The authors restored the immunosuppressive properties of ACs by remethylating the hypomethylated DNA using a CpG methyltransferase [53]. Additionally, others have found that DNA from human DCs can become progressively more immunogenic with aging, as measured by IFN-α expression amounts, and this effect was dependent on DNA hypomethylation associated with aging [54]. These findings support the notion that DNA hypomethylation during aging can beget immunogenic self-derived DNA to trigger inflammatory signaling. To reinforce the notion that hypomethylated self-DNA might

trigger immune responses, we elaborate on the connection of PRRs and DNA-sensing pathways with immune system dysfunction.

2.5 Crosstalk between DNA-sensing pathways and age-associated inflammation

Several cytosolic DNA-sensing (CDS) pathways activate an adaptor protein named stimulator of interferon genes (STING)**,** which regulates the expression of type I interferons (IFNα and IFNβ) through activation of NF-κB and interferon regulatory factor (IRF3) (Table 2). IFN activation may synergistically enhance TLR-induced cytokine transcription by inducing chromatin remodeling (i.e., histone acetylation and transcription factor binding) at promoters and enhancers of target genes. In one of the largest multitissue analyses of aging in mice, researchers found that aging was associated with IFN activation, at both the transcriptional and chromatin levels, along with induction of CDS genes [55].

Ligand(s)	DNA sensor	Signaling pathway -> immune response	Methylation sensitive
Unmethylated CpG motifs	**TLR9**	MyD88-dependent IRF7 activation -> Type I IFNs; MyD88-dependent NF-κB signaling via IKK -> IL-6, TNF-α.	Yes
Sugar-phosphate backbone of dsDNA >15bp, CDNs, ssDNA duplex structures	**cGAS**	STING-dependent activation of TBK1/IRF3 & IKK/NF-κB -> Type I IFNs, IL-6 & TNF-α.	No
AT-rich B-DNA, viral, bacterial and mammalian gDNA 500 bp >> 100 bp > 75 bp	**DAI**	NF-κB activation (via adaptor proteins RIP1 & RIP3) & STING-dependent TBK1-IRF3 activation -> Type I IFNs and necrosis.	Unknown
Poly (I:C), CpG-B	**DHX9**	MyD88-dependent NF-κB signaling ->TNF-α, IL-6.	Yes

CpG-A	**DHX36**	DHX36 forms a complex with TRIF which activates NF-κB & IRF-3/7 -> Type I IFN production.	Yes
dsDNA, bacterial CDNs, cGAMP, poly (dA:dT) & poly(dG:dC)	**DDX41**	STING-dependent activation of TBK1-IRF3 -> Type I IFNs.	Unknown
ssDNA & RNA, dsDNA sequence-independent, 150bp>>70bp>>50bp	**IFI16**	STING-dependent activation of TBK1-IRF3 & NF-κB -> Type I IFNs. Viral DNA in nucleus activates inflammasome.	No
Sugar-phosphate backbone of dsDNA, poly(dA:dT)	**AIM2**	AIM2 bound to dsDNA recruits ASC to form inflammasome complex and activate caspase-1. Active caspase-1 -> IL-1β, IL-18 & pyroptosis.	No
Viral and Alu-RNA, oxidized mtDNA, ATP, cardiolipin, MSU crystals	**NLRP3**	NLRP3 oligomerizes with AIM2 and recruits ASC to form inflammasome which activates pro-caspase-1. Active caspase-1 -> IL-1β & IL-18.	Unknown

Table 2: Characteristics of DNA sensors. Abbreviations: AIM2, Absent In Melanoma 2; ASC, adaptor protein apoptosis speck-like protein; CDNs, Cyclic dinucleotides; cGAMP, Cyclic guanosine monophosphate–adenosine monophosphate; cGAS, Cyclic GMP-AMP synthase; CpG-A, Class A CpG ODNs (characterized by a central, phosphodiester, CpG-containing palindromic motif and a 3' phosphorothioate poly-G string); CpG-B, Class B CpG ODNs (contain a full phosphorothioate backbone with one or more CpG dinucleotides); DEAD, aspartate-glutamate-alanine-aspartate; DDX41, DEAD-Box Helicase 41; DHX9, DEAH-Box Helicase 9 ; DHX36, DEAH-Box Helicase 36; dsDNA, double-stranded DNA; HIN-200, hematopoietic expression, interferon-inducible nature, and nuclear localization; IFI16, Interferon Gamma Inducible Protein 16; IFN, Interferon; IKK, IκB Kinase; IL-1β, interleukin-1 beta; IL-6, interleukin-6; IL-18, interleukin-18; IRF3, Interferon regulator factor 3; IRF7, Interferon regulator factor 7; MAPKs, mitogen-activated protein kinases; MSU, monosodium urate; mtDNA, mitochondrial DNA; MyD88, Myeloid differentiation primary-response protein88; NF-κB, Nuclear factor kappa-light-chain-enhancer of activated B cells; NLRP3, nucleotide-binding oligomerization domain (NOD)-like receptor protein 3; Poly(dA-dT)•poly(dT-dA), a synthetic 45-bp non-CpG DNA oligomer; Poly(dA,dT), homopolymeric stretches of deoxyadenosine nucleotides (A's) on one strand of double-stranded DNA; Poly(I:C): mismatched double-stranded RNA with one strand being a polymer of inosinic acid, the other a polymer of cytidylyl acid; RIP1, receptor interacting proteins 1; RIP3, receptor interacting proteins 3; ssDNA, single-stranded DNA; STING, Stimulator of interferon genes; TBK1, TANK binding kinase 1; TIR, Toll-IL receptor; TLR9, Toll-like receptor 9;

TNF-α, Tumor necrosis factor alpha; TRIF, TIR-domain-containing adapter-inducing interferon-β.

We propose that aging induces changes in DNA released upon cellular demise that originate from epigenetic drift in the chromatin landscape. We postulate that the resulting unmethylated DNA may act as an immunogenic, host-derived biomolecule, which should be further explored as a putative factor contributing to aging induced chronic inflammation [44]. Notably, an inverse correlation has been observed between species lifespan (mouse, nonhuman primate, and human) and rate of epigenetic drift [60], which further strengthens the case that epigenetic drift might be one driver of aging. Even in species harboring significantly low levels of DNA methylation, such as Drosophila spp., epigenetic drift can still be observed in other chromatin marks (e.g., histone modifications) known to trigger PRR signaling [61]. We argue that a better understanding of aging-specific DAMPs and the role of autophagy in promoting longevity may reveal epigenetic drift as a potentially key contributor to species-specific lifespans [62]. Furthermore, this knowledge might help guide the development of personalized medicine based on a patient's 'epigenetic age', the concentrations of inflammatory cytokines, as well as circulating unmethylated self-DNA. Taken together, aging-associated epigenetic changes might represent a new class of 'immunogenic molecular patterns' harboring potential as candidate pharmacological targets in the fight against aging and certain ARDs.

Chapter 3

DNA methylation dynamics during esophageal epithelial regeneration following repair with acellular silk fibroin grafts in rat

Esophageal pathologies such as atresia and benign strictures often require surgical reconstruction with autologous tissues to restore organ continuity. Complications such as donor site morbidity and limited tissue availability have spurred the development of acellular grafts for esophageal tissue replacement. Acellular biomedical implants for esophageal repair rely on the activation of intrinsic regenerative mechanisms to mediate de novo tissue formation at implantation sites. Previous research has identified signaling cascades involved in neoepithelial formation in a rat model of onlay esophagoplasty with acellular silk fibroin grafts, including phosphoinositide 3-kinase (PI3K), and protein kinase B (Akt) signaling. However, it is currently unknown how these mechanisms are governed by DNA methylation (DNAme) during esophageal wound healing processes. We performed reduced-representation bisulfite sequencing to characterize temporal DNAme dynamics in host and regenerated tissues up to 1-week post-implantation. Overall, we observe global hypermethylation at post-reconstruction timepoints and an inverse correlation between promoter DNAme and the expression levels of differentially expressed proteins during regeneration. Site-specific hypomethylation targets genes associated with immune activation while hypermethylation occurs within gene bodies encoding PI3K-Akt signaling components during the tissue remodeling period. Our data provide insight into the epigenetic mechanisms during esophageal regeneration following surgical repair with acellular

grafts. This work characterizes DNA methylation changes during esophageal regeneration in rats after surgical repair with acellular grafts. CpG methylation modulates the transcriptional activity of genes. Decreases in CpG methylation target genes involved in immune activation, while site-specific increases in CpG methylation target genes encoding components of the PIK3-Akt signaling pathway.

3.1 INTRODUCTION

Congenital and acquired disorders of the esophagus including atresia, stricture disease, and malignancies often require surgical reconstruction of focal or tubular esophageal segments with autologous tissue grafts to reestablish organ continuity and restore tissue function [9–12]. However, this gold standard approach is frequently hampered by complications such as donor site morbidity and limited donor tissue availability, [63] which has spurred research into the development of acellular biomaterials for esophageal tissue engineering [64]. Bi-layer silk fibroin (BLSF) scaffolds represent an emerging platform for esophageal repair due to their high structural strength and elasticity, low immunogenicity, and tunable degradative properties [65], These matrices have been previously demonstrated to support the formation of innervated, vascularized esophageal tissues with contractile properties sufficient for solid food ingestion in preclinical animal models. [65,66] Constructive remodeling of BLSF scaffolds is dependent on the ability of host progenitor cell populations to migrate, proliferate, and differentiate within the implant microenvironment to facilitate regeneration of functional neotissues [65]. Molecular mechanisms governing scaffold-mediated wound healing processes in the esophagus are largely unexplored. An increased understanding of

regenerative signaling networks and their regulation may allow for the development of instructive biomaterial designs to maximize esophageal repair outcomes.

Recent reports from our research team utilized quantitative proteomics and in silico pathway evaluations to identify signaling cascades which were significantly activated/inhibited during neoepithelial regeneration in a rat model of onlay esophagoplasty with BLSF grafts [66]. Pharmacologic inhibitor and rescue experiments demonstrated that epithelialization of esophageal neotissues is significantly dependent in part on pro-survival stimuli capable of suppressing caspase activity in epithelial progenitors via activation of hepatocyte growth factor receptor (c-MET), tropomyosin receptor kinase A (TrkA), phosphoinositide 3-kinase (PI3K), and protein kinase B (Akt) signaling pathways. Interestingly, activation of these pro-survival signaling cascades in cancer cells is largely influenced by epigenetic mechanisms, such as DNA methylation (DNAme) which occurs in mammals most commonly in the context of CpG dinucleotides [67]. For example, a loss of DNAme at a CpG island associated with the activation of oncogene *PIK3CA* expression, which encodes a catalytic subunit of PI3K, is thought to play a part in activating the PI3K/Akt pathway and contributing to tumorigenesis in esophageal cancer patients [15]. Altered DNAme signatures of genes encoding integral components of c-MET and TrkA signaling pathways have also been reported to be key drivers of various malignancies. [68,69] The involvement of DNAme in these pathways, which are also essential to regenerative and wound healing responses [17–19], alludes to the potential role of DNAme in facilitating cell fate and lineage decisions in esophageal neotissues. However, the role of DNAme in esophageal tissue regeneration following surgical reconstruction remains poorly understood.

In this present study, we aimed to characterize the DNAme changes which occur following surgical injury and neoepithelial formation in rat esophageal tissues subjected to onlay esophagoplasty with BLSF grafts. Specifically, we performed reduced-representation bisulfite sequencing (RRBS) to profile the DNAme landscape in host and regenerated tissues up to 1 week post-operatively, identified CpGs which undergo differential methylation in response to tissue damage and repair, and elucidated putative biological processes associated with DNAme alterations.

3.2 METHODS

Onlay rat esophagoplasty model

All in vivo procedures and animal husbandry were carried out pursuant to National Institutes of Health guide for the use of laboratory animals under the protocol number AUP-19-153 approved by the Animal Care and Use Committee of the University of California, Irvine. Adult male Sprague-Dawley rats (Charles River Laboratories, San Diego, CA) weighing 260-300 grams were randomized into the 3 groups according to implantation period including nonsurgical controls (NSC) (n=8), Day1 post-op (n=8), and Wk1 post-op (n=8). Day1 and Wk1 groups were subjected to onlay esophagoplasty with BLSF grafts using published protocols [66] as described below. Prior to surgical reconstruction, animals were single housed in wire cages and maintained on a nutritionally balanced liquid diet formulation (TestDiet, Richmond, IN mixed with PediaSure, Abbott Laboratories, Columbus, OH) for Day1 prior to surgery and continued for 3 days post-operatively. In addition, rats were also given to free access water during the entire study period. General anesthesia was induced and maintained by 2-4% isoflurane inhalation. Abdominal fur was then clipped, and the skin was sterilized with

betadine and 70% ethanol. The surgical area was covered by sterile drapes. The intra-abdominal portion of the lower esophagus was approached by a vertical midline abdominal incision. The esophagus was then pulled to the skin level using two vessel loops and a full thickness 7x3 mm elliptical defect was created on the anterior esophageal wall. The defect was repaired with an equal sized BLSF graft via anastomosis with the surrounding host tissue using absorbable 7-0 polyglactin running sutures. Four 7-0 nonabsorbable polypropylene sutures were positioned at the proximal/distal and lateral edges of the implanted matrix in order to identify the original scaffold margins. The scaffold was then covered with an omental patch to minimize any potential leakage from the suture line and the esophagus was placed back into the abdomen and tissue layers were sutured closed. Post-operative pain control was managed with 0.5% bupivacaine diluted 1:1 with saline as well as Buprenorphine SR (1.2 mg/kg, subcutaneously) and fluxine meglumine (2.5 mg/kg; subcutaneously). Animals received enrofloxacin (5mg/kg; 3 days post-operatively, subcutaneously) for mitigation of potential bacterial infection. All rats were transferred from liquid diet to standard rat chow 3 days after surgery and were euthanized by carbon dioxide asphyxiation at experimental timepoints. Following animal harvest, esophageal tissues from each group were equally segregated for either epigenetic or histological/immunohistochemical analyses (n=4 per group for each assay). For epigenetic studies, biopsy punches were utilized to acquire host esophageal tissues surrounding 2 mm of the original defect circumference at Day1 post-op, while neotissues at Wk1 post-op were isolated from the initial graft area. Full thickness esophageal specimens were harvested in parallel from NSC for baseline epigenetic evaluations.

Histological and immunohistochemical (IHC) analyses

Reconstructed esophageal segments (N=4 per timepoint) as well as nonsurgical control (NSC) specimens (N=4) were fixed in 10% formalin for 12 hours, dehydrated in graded alcohols, and paraffin embedded. Tissue sections (5 μm) were stained with Masson's trichrome to reveal global tissue architecture using standard histological protocols. Masson's trichrome staining and immunohistochemical (IHC) analyses were performed on four biological replicates in each condition: non-surgical controls (NSCs), Day1, and Wk1 (n=4 for each condition). IHC evaluations were performed on tissue sections following antigen retrieval (10 mM sodium citrate buffer, pH 6.0) and incubation in phosphate-buffered saline with 0.3% Triton X-100, 5% fetal bovine serum, and 1% bovine serum albumin for 1 hour at room temperature. Sections were then stained with primary antibodies including anti-DNA methyltransferase (DNMT)1 (cat. # 24206-1-AP, 1:200 dilution, Proteintech, Rosemont, IL), anti-DNMT3A (cat. #GTX129125, 1:200 dilution, GeneTex, Irvine, CA), anti-DNMT3B (cat. # PA1-884, 1:200 dilution, Invitrogen, Waltham, MA), anti-cytokeratin (CK)5 [cat. # ab53121, 1:200 dilution, Abcam], and anti-filaggrin (FG) (cat. #sc-80609, 1:200 dilution, Santa Cruz Biotechnology). For DNMT1, 3A, and 3B detection, specimens were then incubated with species-matched horseradish peroxidase (HRP)-conjugated secondary antibodies in combination with hematoxylin counterstain. For CK5 and filaggrin detection, samples were probed with species-matched Alexa Fluor 488 and 647-conjugated secondary antibodies (Thermo Fisher Scientific) and nuclear counterstain was carried out with 4′, 6-diamidino-2-phenyllindole (DAPI). An Axioplan-2 microscope (Carl Zeiss MicroImaging, Thornwood, NY) was deployed for sample visualization and representative fields were acquired with Axiovision software (version 4.8).

RRBS Library preparation

10mg of tissue each was collected for DNA isolation using Qiagen DNeasy Blood & Tissue kit (Qiagen, Hilden, Germany). 4.5ug of genomic DNA was digested with MspI overnight. The digested products were size-selected using AMPure XP beads to remove anything above 300bp or small fragment retention. 100ng size-selected DNA was bisulfite-converted using EZ DNA Methylation-Gold Kit (Zymo Research, Irvine, CA). The eluted DNA was performed immediately using the Accel-NGS Methyl-seq DNA library kit (Swift Biosciences, Ann Arbor, MI) according to the manufacturer's instructions. Final libraries were generated from 9-14 PCR cycles. PCR products were cleaned up using the SPRIselect beads (Beckman Coulter, Orange, CA) to remove the primer dimers. Libraries were confirmed by an Agilent Bioanalyzer, and the yields were quantified by KAPA qPCR. Sequencing was performed at the UCI Genomics High Throughput Facility. 100bp paired-end reads were sequenced by Illumina Nova-seq 6000 sequencing system.

RRBS data processing and detection of DMCs

Adaptor and low-quality RRBS reads in FASTQ format were trimmed and filtered using Trim Galore (version 0.6.6) with the following parameters: "--paired --clip_r1 10 --clip_r2 15 --three_prime_clip_r1 10 --three_prime_clip_r2 10 --fastqc". Reads were aligned to the rat genome (mRatBN7.2/rn7, data: 2020/11/10) with Bismark (version 0.23.0) [70]. On average, 22.8 million trimmed reads per sample were aligned to rat genome (mRatBN7.2/rn7, release 105, Ensembl). As a quality control measure, the RRBS data analysis as performed on biological replicates that had a mapping efficiency value $\geq$70%. CpG sites were called using the "bismark_methylation_extractor" function (--

comprehensive option) in Bismark. Differential methylated cytosines (DMCs) were called with methylKit (version 1.14.2) for CpGs with a minimum of 5 counts [71].

Genomic feature annotations

The methylation percentages for genomic regions, gene bodies, promoters, 5′-UTRs, exons, introns and 3′-UTRs were found using BEDTools' intersect function to finding the overlapping CpGs (≥5x coverage) in the sample BED files and genomic tracks from UCSC genome table browser (BEDTools version 2.25.0). Intergenic features were acquired by finding regions outside of gene bodies using BEDTools' complement function and the size of each chromosomes in the rat genome (rn7) which was obtained by downloading the rn7.chrom.sizes.txt file from NCBI [72,73]. Genomic promoter features were defined as 2kb upstream and 500bp downstream of gene transcription start sites (TSS) acquired from UCSC genome table browser. Gene body features were defined as 500bp downstream of TSS from UCSC genome table browser to prevent overlap between the promoter track and gene body track.

Identification of gene network and ontologies from DMC-associated gene lists

The list of genes associated with DMCs were obtained by intersecting locations of CpGs with locations of annotated genes in the rat genome assembly (mRatBN7.2) obtained from NCBI Rattus norvegicus Annotation Release 108 (Assembly accession: GCF_015227675.2). The enrichment analysis was performed on the genes associated with DMCs within promoters and within gene bodies for Gene Ontology (GO) Biological Processes (BP), Protein Analysis Through Evolutionary Relationships (PANTHER) Pathway, and Kyoto Encyclopedia of Genes and Genomes (KEGG) enriched pathways using ShinyGO (version 0.75).[74–77] Enriched GO (BP) and pathways were filtered

using a false discovery rate (calculated according to the Benjamini & Hochberg method)≤ 0.05 [78].

Determining differentially methylated transcription factor binding sites (TFBS)

DMC files, in BED format, were inputted into Hypergeometric Optimization of Motif EnRichment (HOMER) software (Version 4.11) to identify enrichment of known TFBS motifs, reposited within the software's vertebrae database [79]. BED files were converted to Rnor_6.0 genome assembly version with UCSC's liftOver tool. Analyses were performed with the list of CpGs (5x coverage) present in at least 3 replicates per experimental condition as background and the motif size parameter set to 200bp. TFBS motif results were finally filtered for *p*-value≤ 0.01.

LiftOver human enhancer tracks

Human enhancer-gene interaction networks annotated in hg19 for esophagus whole cell and the neutrophil-like cell line (HL-60) were obtained from EnhancerAtlas 2.0 [80]. The downloaded files were processed with Python 3.0 to create BED files that include the chromosome number, start and end coordinates of the enhancer region, strandedness, and the associated gene names. The UCSC liftOver tool was used to lift over BED files from the human genome to the rat genome. Minimum ratio of bases that must remap was set at 0.1. BED files for hg19 enhancer tracks were first lifted over to the hg38 genome (100% liftOver conversion rate) and then lifted over to the rat genome (rn7) (91% liftOver conversion rate) since the liftOver tool does not allow for a direct conversion from hg19 to rn7.

Determining differentially methylated lifted enhancers

The BED files containing our filtered set of CpGs (≥5x coverage found in ≥3 samples in each condition, n=514,813) for each timepoint were intersected with lifted enhancer BED files obtained from EnhancerAtlas 2.0 using BEDTools (version 2.25.0). We calculated the average methylation values for CpGs for each lifted enhancer. Differentially methylated enhancers were identified using a 20% threshold value for the methylation difference between each surgical timepoint compared to the NSC (i.e., NSC->Day1 and NSC->Wk1). We filtered the lifted unique gene-enhancer pairs for genes that were previously identified as DEPs during esophageal regeneration based on data from Gundogdu et al. Sci Reports. 2021 [66]. Logarithmic odds ratio (logOR) analyses were performed to determine the significance of differentially methylated gene-enhancers pairs with genes encoding DEPs. Our confusion matrices were configured to consider hypomethylated/hypermethylated or not lifted enhancers and upregulated/downregulated or not DEPs. Fisher's exact test was used to determine the significance of odds ratios using R (version 4.0.5).

Statistical Analysis

All statistical tests were performed with R (version 4.0.5). To ensure high-quality reads were used in the analysis, only RRBS samples with an alignment efficiency of 70% or greater were used in downstream data analysis which resulted in the following number of biological replicates: NSC (n=4), Day1 (n=5), and Wk1 (n=4). Significance values were calculated using the Wilcoxon rank-sum test in R (version 4.0.5) because the data did not follow a Gaussian distribution. The *p*-values were listed in each figures and *ns* indicates a *p*-value >0.05. Euclidean hierarchical clustering was performed on CpGs with >5x coverage that were captured in all samples: NSC (n=4), Day1 (n=5), and Wk1 (n=4)

(n=3,494 CpGs). The hierarchical clustering was performed with pHeatmap package (version 1.0.12) using the Ward's minimum variance method (Ward.D2) clustering method in RStudio (version 4.0.5). DMC statistical analysis was performed on CpGs with >5x coverage that were found in a minimum of three biological replicates in each condition and were present across all conditions (n=514,813 CpGs). DMCs were determined by comparing in the mean differences in methylated calls for a particular cytosine between the non-surgical controls and post-op timepoint samples using a threshold value of q-value <0.01 and meth.diff value >20% using the R package methylKit (Version 1.16.0). The DEP data was obtained from Gundogdu et al. Sci Reports. 2021 which identified DEPs from proteomic analysis of regenerating rat esophageal tissues following repair with acellular grafts using a threshold value of >2-fold (log2ratio >1 or <-1) between the NSC controls and post-surgical timepoints (1 day, 1 week, 1 month, 2 months post-op) (N= 4 for experimental condition) [66].

3.3 RESULTS

3.3.1 RRBS reveals global DNA hypermethylation during surgical reconstruction and regeneration of esophageal tissue

In this study, we performed histological, immunohistochemistry (IHC), and RRBS analysis on rat esophageal tissue that was collected at 1 day (Day1) and 1 week (Wk1) following onlay esophagoplasty with BLSF grafts, as well as from nonsurgical controls (NSC) (Fig. 5A-B). There were no significant intra-operative or post-operative complications with onlay esophagoplasty procedures and the survival rate was 100% until scheduled euthanasia. Masson's trichrome staining of reconstructed esophageal tissue was performed to temporally characterize the host response and degree of tissue

regeneration following scaffold implantation (Fig. 5B). Day1 post-op, the BLSF graft was largely intact and the implant site was populated with mononuclear inflammatory cells and neutrophils with limited tissue integration from the host esophagus. At Wk1 post-op, an epithelialized fibrovascular scar composed of mononuclear inflammatory and fibroblastic cell types was evident within the original graft site (Fig. 5B).

We performed immunohistochemistry (IHC) staining for the three major mammalian DNA methyltransferases DNMT1, 3A, and 3B protein expression which revealed the presence of all 3 methyltransferases in NSC and reconstructed host tissues at Day1 and Wk1 after surgery. DNMT3B expression was primarily nuclear and was detected in epithelial, mucosal, and skeletal muscle compartments throughout NSC and reconstructed tissues NSC (Fig. 5C). In contrast, NSC tissues displayed both cytoplasmic and nuclear DNMT1 and DNMT3A expression which was mainly localized to CK5+FG-basal epithelial cells. Qualitative increases in cytoplasmic expression of these markers were also observed in host and regenerated epithelia at Day1 and Wk1, respectively, in comparison to NSC (Fig. 5C).

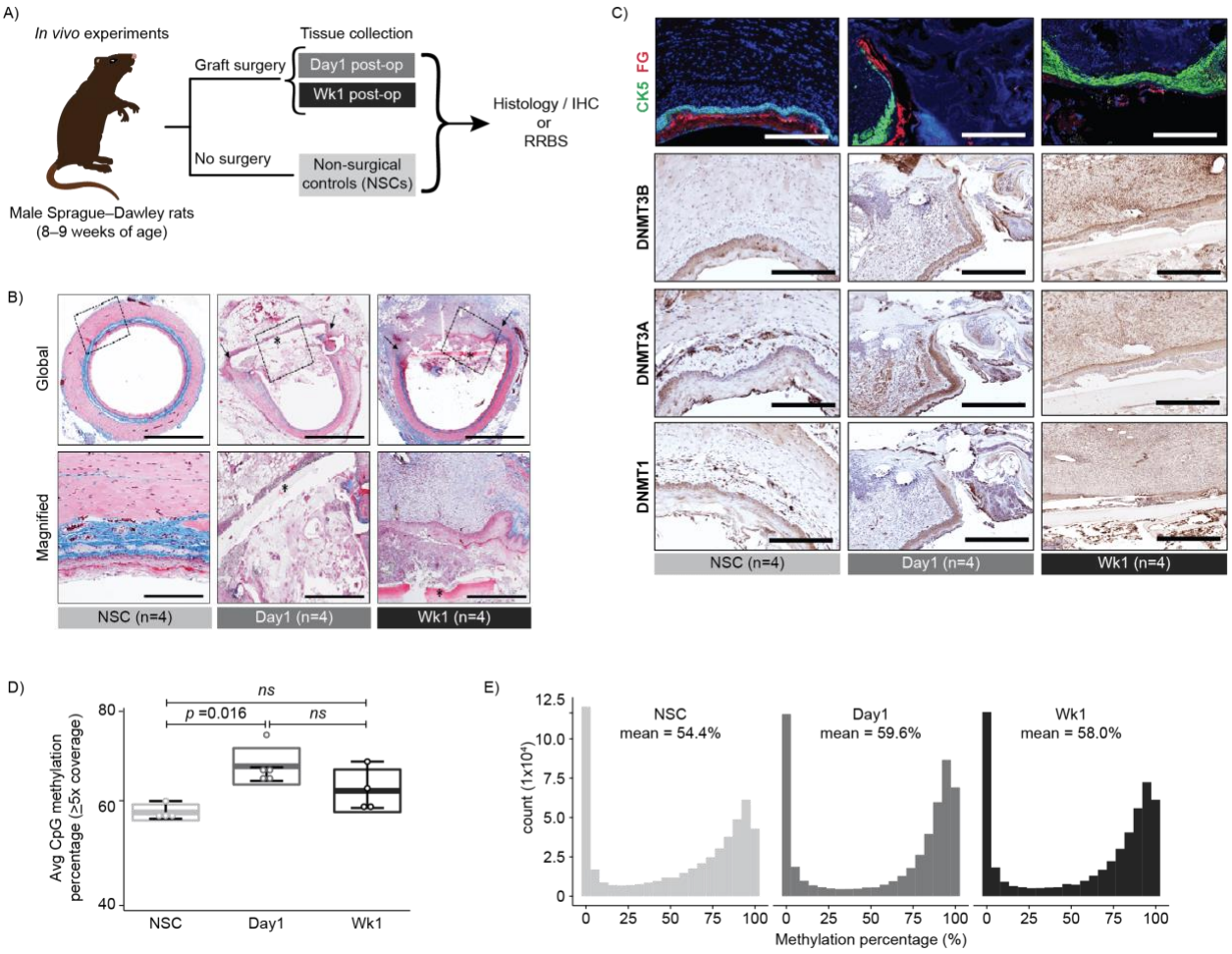

Figure 5. RRBS characterization of temporal DNA methylation dynamics during esophageal regeneration. A) Schematic representation of the experimental setup. Timeline, experimental conditions, and corresponding controls are shown. For RRBS, non-surgical controls (NSCs. n=4), Day1 (n=5), and Wk1 (n=5). For histological and immunohistochemical (IHC) analyses, NSCs (n=4), Day1 (n=4), and Wk1 (n=4). B) Masson's trichrome staining of reconstructed esophageal tissues was performed to temporally characterize early phases of tissue regeneration and host tissue responses during the scaffold implantation period (n=4 for each condition). Arrows denote anastomotic borders of the implant site and asterisks denote residual scaffold fragments. C) Top: Representative images of NSC and neotissues supported by acellular grafts demonstrating protein expression of cytokeratin (CK)5 and filaggrin (FG) expression in red (FG) or green (CK5) while DAPI nuclear counterstain is detailed in blue. Cyan coloring is a consequence of merging CK5 and DAPI staining. IHC profiling of DNMT1, 3A, and 3B protein expression in NSC and in reconstructed host tissues at Day1 and Wk1 after surgery with counterstain. For all panels, images are representative of four biological replicates (n=4 for each condition). Scale bars = 200 μm. D) Boxplot displaying the mean genome-wide CpG methylation percentage using the average number of CpG captured with ≥5x coverage in each condition: NSC (n=3,311,677), Day1 (n=2,708,305), and Wk1

(n=13,610,699) for NSC (n=4), Day1 (n=5), and Wk1 (n=4) biological replicates. Boxplots indicate the mean (middle thicker line) and interquartile range (outer box) of NSC (n=4), Day1 (n=5), and Wk1 (n=4) independent biological replicates. The *p*-values were calculated using Wilcoxon rank-sum test. *ns* indicates $p > 0.05$. E) Histograms displaying the distribution of CpG methylation percentage in each experimental group for CpGs ($\geq$5x depth) that were captured in at least 3 replicates in each experimental group (n=514,813) for NSC (n=4), Day1 (n=4), and Wk1 (n=4) biological replicates.

To characterize CpG methylation during regeneration we performed RRBS on genomic DNA extracted from harvested rat esophageal tissues and sequenced reads were aligned to the rat genome (mRATBN7.2/rn7) using Bismark (see Methods). On average, we captured 14.7 million CpGs with >70% mapping efficiency per sample which is consistent with previous RRBS reports in rat (Fig 6A). Methylation calls were performed with Bismark (see Methods) [81]. To compare global patterns of site-specific CpG methylation during regeneration, CpGs were filtered for $\geq$5x coverage. We identified a significant increase in the percentage of methylated CpGs captured at Day1 relative to the NSC condition (p=0.016) (Fig 5D). DNAme levels decreased between Day1 and Wk1, however this difference was not significant (p=0.19). DNAme levels at Wk1 compared to the NSC condition were not significantly different (p=0.11). This result suggests that esophageal tissues undergo a gain in DNAme, or DNA hypermethylation, during regeneration which may be a transient response immediately following surgical repair as methylation levels appear to trend towards baseline (NSC) levels by Wk1 post-op.

Of the captured CpGs, a total of 514,813 unique CpG sites were captured in $\geq$3 replicates in all conditions and used in downstream analyses. These CpGs fell within intergenic regions (40.1%), introns (43%), promoters (24.6%), and exons (21.9%). Methylation calls for the total 514,813 CpGs were merged across replicates within each condition. Consistent with our previous global CpG analysis, the distributions of DNAme

percentage at each timepoint revealed that Day1 and Wk1 conditions exhibited a greater frequency of highly methylated CpGs (e.g., methylation percentage >80%) relative to the NSC condition (Fig. 5E).

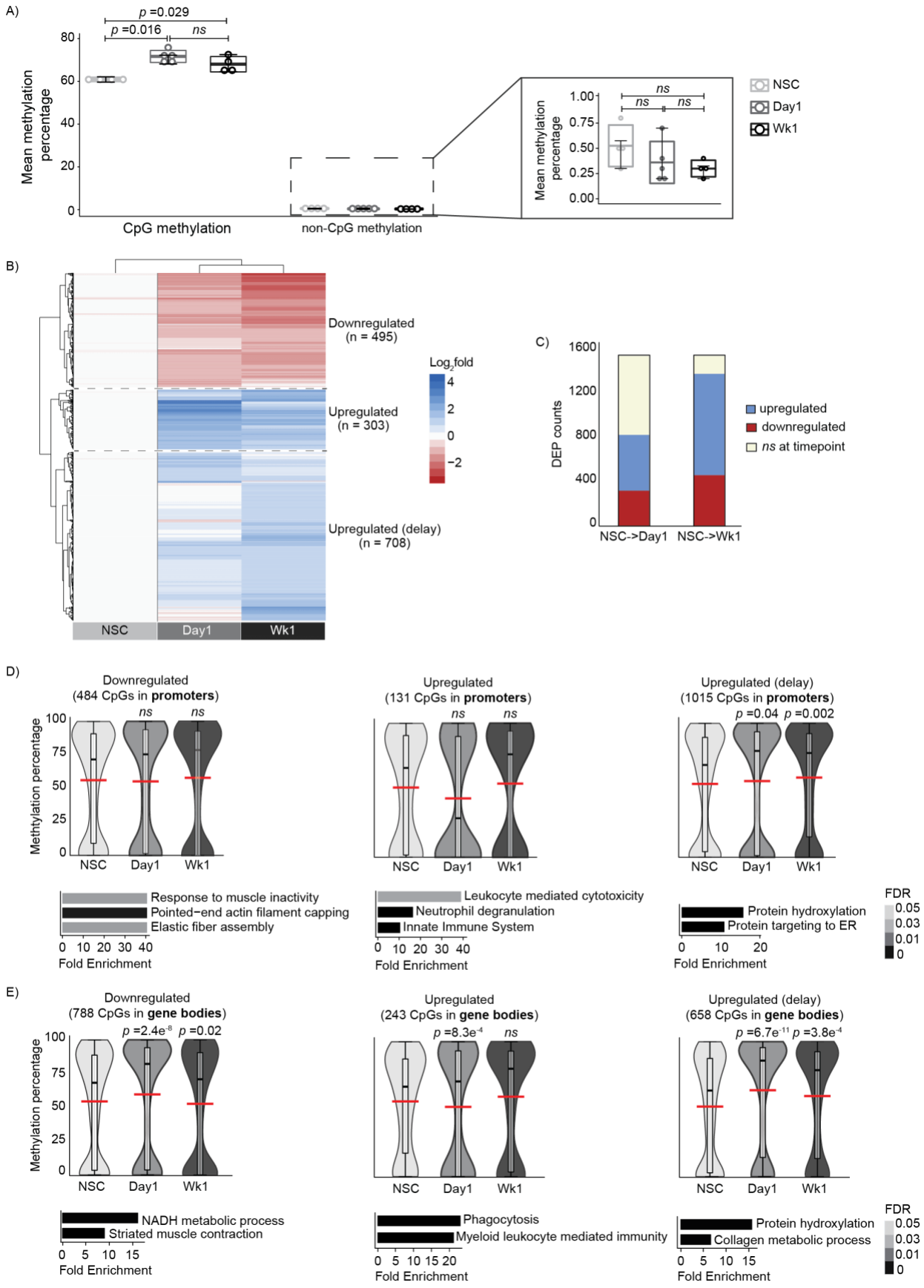
A)
p =0.029
p =0.016
ns
Mean methylation percentage
CpG methylation
non-CpG methylation
NSC
Day1
Wk1
B)
Downregulated (n = 495)
Upregulated (n = 303)
Upregulated (delay) (n = 708)
Log2fold
NSC
Day1
Wk1
C)
DEP counts
upregulated
downregulated
ns at timepoint
NSC->Day1
NSC->Wk1
D)
Downregulated (484 CpGs in promoters)
Upregulated (131 CpGs in promoters)
Upregulated (delay) (1015 CpGs in promoters)
p =0.04
p =0.002
Methylation percentage
Response to muscle inactivity
Pointed-end actin filament capping
Elastic fiber assembly
Leukocyte mediated cytotoxicity
Neutrophil degranulation
Innate Immune System
Protein hydroxylation
Protein targeting to ER
Fold Enrichment
FDR
E)
Downregulated (788 CpGs in gene bodies)
Upregulated (243 CpGs in gene bodies)
Upregulated (delay) (658 CpGs in gene bodies)
p =2.4e-8
p =0.02
p =8.3e-4
p =6.7e-11
p =3.8e-4
NADH metabolic process
Striated muscle contraction
Phagocytosis
Myeloid leukocyte mediated immunity
Protein hydroxylation
Collagen metabolic process

Figure 6. Characterization of DNA methylation and protein expression dynamics during esophageal regeneration. A) Boxplot displaying the mean genome-wide CpG methylation percentage of each condition using the total number of CpGs captured. The average number of CpG captured per condition: NSC (n=12,806,052), Day1 (n=17,119,293), and Wk1 (n=13,610,699). CpG methylation levels were obtained using the Bismark methylation extractor function. The *p*-values were calculated using Wilcoxon rank-sum test. B) Heatmap of 1,506 proteins found to be differentially regulated by twofold (log2ratio > 1 or < − 1) in at least one post-surgical timepoint relative to the NSC condition. Data was obtained from Gundogdu et al. Sci Rep. 2021 [22]. C) Stacked barplots show the number of DEPs that were upregulated, downregulated, or had no significant change at each timepoint relative to the NSC condition. Data was obtained from Gundogdu et al. Sci Rep. 2021 [22]. D) Top: Violin plots depicting the distribution of CpG methylation percentage for CpGs within promoters of genes that encode DEPs from Groups 1, 2, and 3. Red horizontal lines represent the mean and black horizontal lines represent the median. Bottom: Bar plots showing the fold enrichment and corresponding adjusted *p*-values for GO: biological processes (BPs) enriched for CpG-associated genes encoding DEPs from Groups 1, 2, and 3. The *p*-values were calculated using Wilcoxon rank-sum test for each timepoint relative to the NSC. E) Top: Violin plots depicting the distribution of CpG methylation percentage for CpGs within gene bodies of genes that encode DEPs from Groups 1, 2, and 3. Red horizontal lines represent the mean and black horizontal lines represent the median. Bottom: Bar plots showing the fold enrichment and corresponding adjusted *p*-values for GO: BPs enriched for CpG-associated genes encoding DEPs from Groups 1, 2, and 3. The *p*-values were calculated using Wilcoxon rank-sum test for each timepoint relative to the NSC.

3.3.2 Promoter methylation is inversely correlated with expression level of differentially expressed proteins (DEPs) during regeneration

Previously, our lab identified a set of 1,506 differentially expressed proteins (DEPs) that are modulated during regeneration in esophageal tissues following BLSF implant surgery [66], examples are shown in (Fig. 6B-C). To better understand the relationship between DEPs and methylation changes, we investigated how methylation levels change in CpGs that fall within genic regions encoding DEPs. Notably, methylation levels were lower in CpGs within promoters and gene bodies that encode upregulated DEPs at Day1 compared to the NSC (Fig. 6D-E). Gene ontology (GO) analysis revealed these genes were enriched for biological processes (BP) associated with immune activation (Fig. 6D-E). This could reflect immune cell infiltration at the graft

site which has been observed previously after surgical injury and during wound healing processes [82].

To characterize differential DNAme during post-surgical reconstruction, we identified a set of differentially methylated CpGs (DMCs) that were determined based on their magnitude of DNAme changes (≥20% methylation difference) and their significance level ($q<0.05$) between timepoints. We focused initially on identifying DMCs present in post-op samples compared to NSCs (i.e., NSC->Day1, NSC->Wk1). We found that DMCs that fell within promoter of genes encoding DEPs showed an inverse correlation in their methylation difference compared to previously reported changes in protein expression for NSC→Day1 and NSC→Wk1 timepoints ($R=-0.52$ and -0.37 respectively) (Fig. 7A).

We observed a similar, but less apparent inverse correlation for DMCs located within the gene body of genes encoding DEPs (Fig. 7B). We found upregulated DEPs were associated with DNA hypomethylation at NSC->Day1 DMCs that occurred in promoters of genes involved in immune activation such as S100A8 (S100 Calcium Binding Protein A8) and Platelet factor 4 (Pf-4) (Fig. 7A) [83]. Pf-4 regulates proinflammatory responses in monocytes and macrophages in humans and murine bone marrow-derived macrophages and acts as an inhibitor of angiogenesis [84,85]. The most upregulated DEPs were associated with DNA hypomethylation at NSC->Wk1 DMCs found in the promoters of genes involved in T-cell activation such as Vav Guanine Nucleotide Exchange Factor 1 (VAV1), a critical regulator of signal transduction in T-cells and B-cells, and Proteasome subunit beta type-10 (Psmb10) which forms an immunoproteasome complex involved in histocompatibility complex antigen presentation (Fig. 7A) [86].

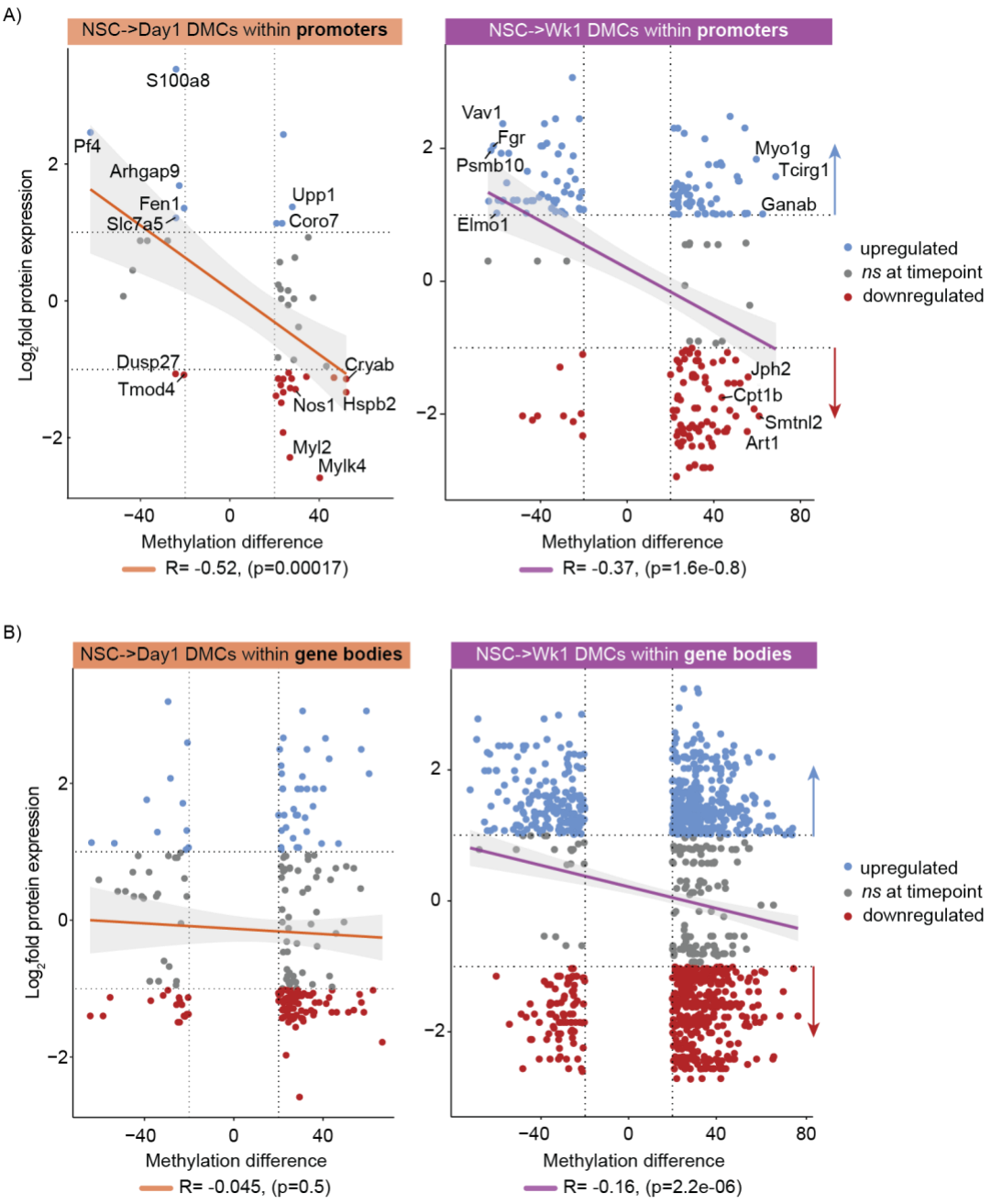

Figure 7. CpG methylation levels are inversely correlated with DEP expression levels during regeneration. A) Left: Scatterplot displaying the methylation difference for NSC->Day1 DMCs that fall within promoters, as well as the log_2fold protein expression value for the protein encoded by the gene associated with that DMC. Orange line represents linear regression and gray shading represents 95% confidence interval. Right: Scatterplot displaying the methylation difference for NSC->Wk1 DMCs that fall within promoters, as well as the log_2fold protein expression value for the protein encoded by the gene associated with that DMC. Violet line represents linear regression and gray shading represents 95% confidence interval. Dotted horizontal lines represent log_2fold protein expression value of 1 and -1. Dotted vertical lines represent 20% methylation difference

threshold for calling DMCs. The average log_2fold protein expression of DEPs which were previously identified in post-surgical timepoints compared to the NSC for biological replicates (4 for each condition). The proteomics data was obtained from Gundogdu et al. Sci Reports. 2021 [66]. B) Left: Scatterplot displaying the methylation difference for NSC->Day1 DMCs that fall within gene bodies, as well as the log_2fold protein expression value for the protein encoded by the gene associated with that DMC. Orange line represents linear regression and gray shading represents 95% confidence interval. Right: Scatterplot displaying the methylation difference for NSC->Wk1 DMCs that fall within gene bodies, as well as the log_2fold protein expression value for the protein encoded by the gene associated with that DMC. Violet line represents linear regression and gray shading represents 95% confidence interval. Dotted horizontal lines represent log_2fold protein expression value of 1 and -1. Dotted vertical lines represent 20% methylation difference threshold for calling DMCs. The average log_2fold protein expression of DEPs which were previously identified in post-surgical timepoints compared to the NSC for biological replicates (4 for each condition) (n=1,506 DEPs). The proteomics data was obtained from Gundogdu et al. Sci Reports. 2021 [66].

3.3.3 While the genome shows global hypermethylation, genic regions contain both hyper and hypomethylated DMCs

We next sought to characterize timepoint-specific changes in DNAme during esophageal regeneration. To do so, we identified DMCs that were uniquely associated to a single two-way timepoint comparison versus those that were shared multiple two-way timepoint comparisons (Fig. 8A). At this resolution, we observed the majority of DMCs were uniquely associated with the NSC->Wk1 condition (n=28,552). The NSC->Day1 condition had the second largest number of uniquely associated DMCs (n=6,120) and the Day1->Wk1 condition had the fewest uniquely associated DMCs (n=535). Thus, we focused our downstream analyses on the majority of DMCs which occur between post-surgical timepoint conditions and the NSC (i.e., NSC->Day1 DMCs and NSC->Wk1 DMCs). While there were 135 universally shared DMCs among all three timepoint comparisons, NSC->Day1 and NSC->Wk1 comparisons shared a total of 5,658 DMCs. We found that the majority of DMCs in the NSC->Day1 and NSC->Wk1 conditions were hypermethylated (9,247 and 25,945, respectively) while a substantially smaller subset of

DMCs were hypomethylated at these same timepoints (3,032 and 8,561, respectively) (Fig. 8B). The distribution of methylation difference comprising hypermethylated DMCs (HyperDMCs) and hypomethylated DMCs (HypoDMCs), however, appeared comparable across both timepoint comparisons (Fig. 8C). To profile DNAme changes among shared DMCs across individual samples, the set of CpGs comprising the 5,658 shared DMCs between NSC->Day1 and NSC->Wk1 was further filtered for CpGs with $\geq$5x coverage across all experimental samples, which resulted in 3,494 CpGs (Fig. 8D). Euclidean hierarchical clustering revealed that the data separated according to CpG site dynamics and condition. We found three DNA methylation patterns emerged during regeneration. We observed >70% of CpGs gained methylation in post-surgical timepoints (Cluster 2 and Cluster 3) while the DMCs in Cluster 1 lost methylation in post-surgical timepoints (Fig. 8D). The relative distribution of CpGs captured in each cluster revealed that the majority of DMCs in Cluster 1 and Cluster 3 occur within gene bodies (79% and 57% respectively) and a smaller percentage occur in promoters (14% and 21% respectively). The majority of DMCs in Cluster 2 occur outside of promoters and gene bodies (Fig. 8D). DMCs in Cluster 3 were lowly methylated in NSCs and levels of DNAme increased following surgical repair at Day1 and Wk1 (Fig. 8D).

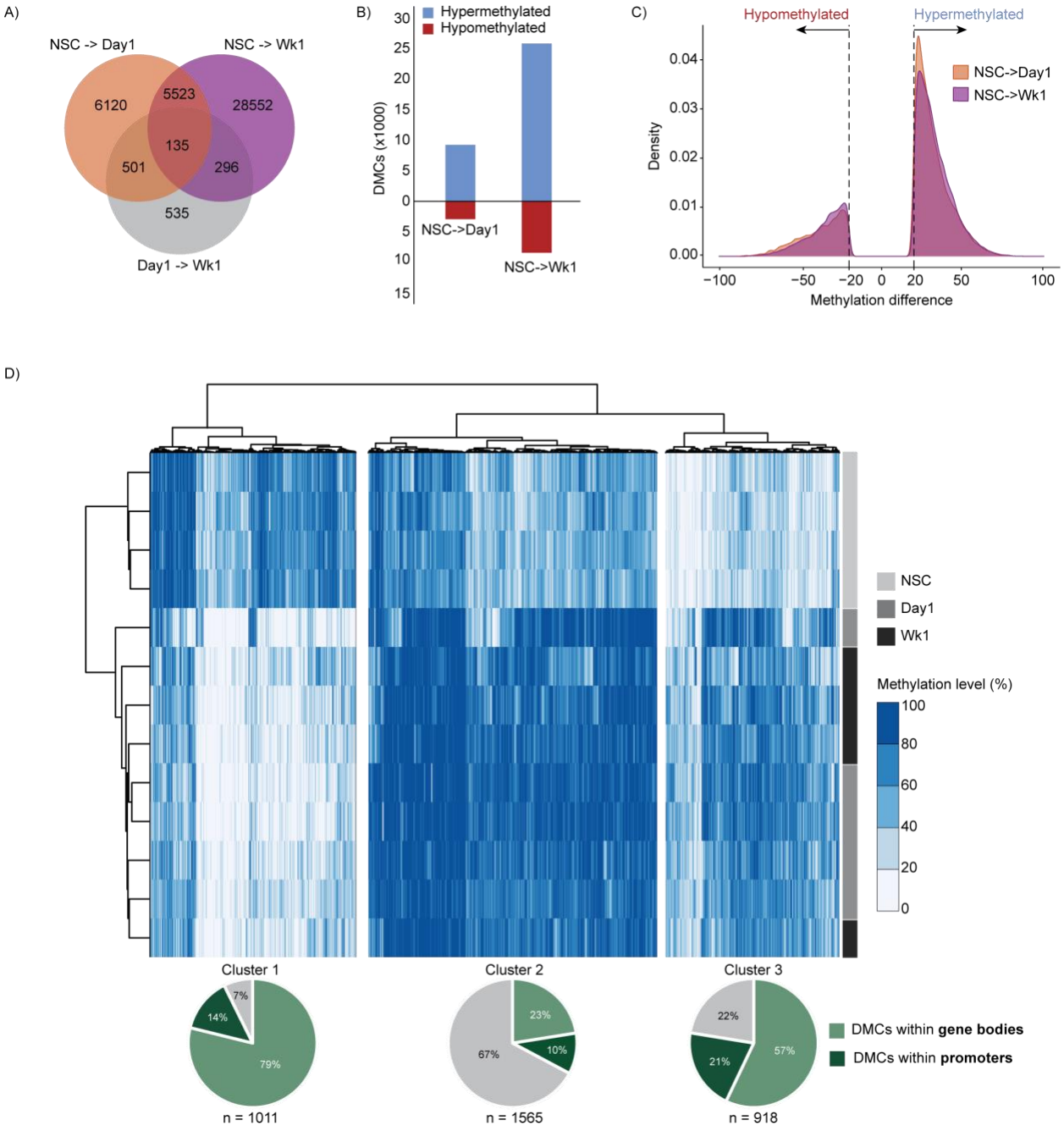

Figure 8. DNA hypermethylation is largely observed at post-surgical repair timepoints. A) Venn diagram displaying shared and unique DMCs called among the comparison groups: NSC->Day1 (DMCs called at Day1 relative to NSC baseline), NSC->Wk1 (DMCs called at Wk1 relative to NSC baseline), Day1->Wk1 (DMCs called at Wk1 relative to Day1). DMCs were called at a threshold of 20% CpG methylation difference and q-value<0.01. The number of DMCs for each group comparison: NSC->Day1 (n=12,279), NSC->Wk1 (n=34,506) and Day1->Wk1 (1,467). B) Bar plot showing the number of hypermethylated and hypomethylated DMCs in each comparison group. The number of hypermethylated DMCs for the NSC->Day1 (n=9,247) and

NSC->Wk1 (25,945) groups. The number of hypomethylated DMCs for the NSC->Day1 (n=3,032) and NSC->Wk1 (8,561). C) Density plot depicting the distribution of hypermethylated and hypomethylated DMCs in each comparison group. D) Top: For shared DMCs that are represented in each individual sample with ≥5x coverage (n=3,494), corresponding CpG methylation levels within in each sample are shown in the heatmap. Euclidean hierarchical clustering was performed with pHeatmap package (version 1.0.12) using the ward.D2 clustering method in RStudio (version 4.0.5). Three clusters with different temporal DNA methylation dynamics were identified. Bottom: Pie charts displaying the distribution of DMCs corresponding to each cluster that fall within a gene body, promoter, or neither.

To better understand the functional implications for the patterns of DNAme we observed, we performed GO and Kyoto Encyclopedia of Genes and Genomes (KEGG) enrichment analysis on the genes associated with identified DMC clusters *[74]*. Interestingly, we found DMCs in Cluster 3, which start out lowly methylated and gain methylation, were associated with genes that were enriched for GO (BP) terms associated with cytokine production (Fig. 9A). Genes associated with DMCs within promoters in Cluster 3 were not enriched for any KEGG pathways (Fig. 9B). In contrast, DMCs in Cluster 1, which are hypomethylated at post-surgical timepoints, were associated with genes that are enriched for GO (BPs) such as epithelial cell differentiation and regulation of cell migration (Fig. 9C). We found hypermethylated DMCs, found in Cluster 1 and Cluster 2, occur in genes involved in pathways that have been implicated in esophageal regeneration in previous studies. Specifically, genes associated with DMCs in Cluster 2 were enriched for KEGG pathways including vascular endothelial growth factor (VEGF), Ras, and PI3K-Akt (Fig. 9B-D) .

Next, to investigate whether methylation patterns were indicative of changes in gene regulatory elements, we determined whether DMC locations were enriched for certain classes of transcription factor binding sites (TFBS). We performed TFBS motif

enrichment analysis in our DMCs using Hypergeometric Optimization of Motif EnRichment (HOMER) *[79]*. We found Cluster 1 and Cluster 2 were enriched for several members of the basic helix-loop-helix (bHLH) family of transcription factors (TF) which have been implicated in cell lineage determination and differentiation (Fig. 9E) *[90,91]*. DMCs in Cluster 3 were enriched for motifs associated with the ETS Homologous Factor (EHF) which targets genes that characterize epithelial-specific expression patterns, and E26 transformation-specific (ETS) TF family such as E74 Like ETS Transcription Factor 4 (Elf4) and ETS1 which have been implicated in cell proliferation, apoptosis, morphogenesis, and mesenchymal–epithelial interactions, especially during development (Fig. 9E).

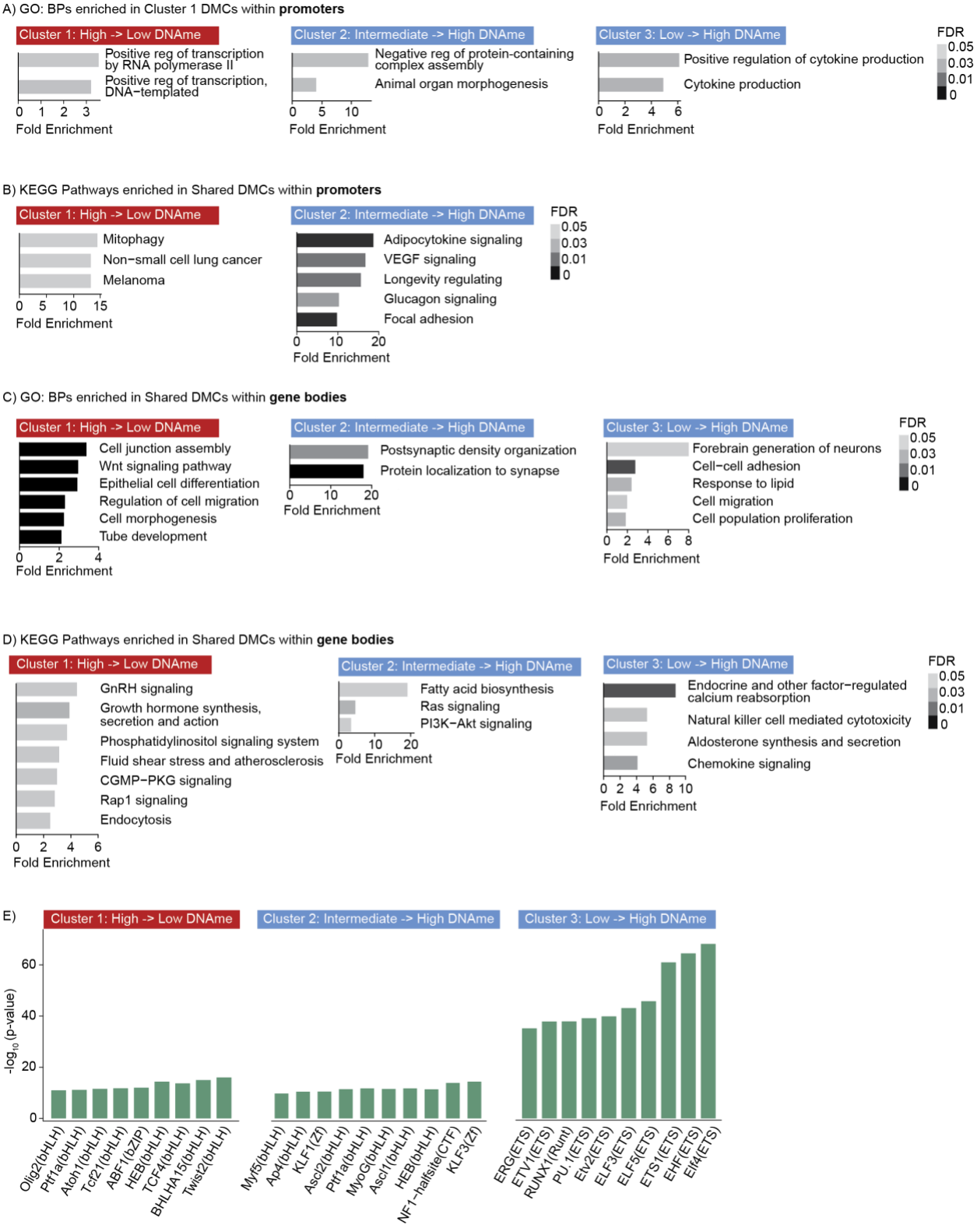

Figure 9. GO and KEGG analysis in DMCs with similar patterns of methylation changes during regeneration. A) Bar plots depicting GO: biological processes (BP) enriched in the gene list associated with DMCs found in promoters for each cluster

shown in Figure 8D. For 9A-D, the x-axis indicates fold enrichment and colors indicate false-discovery rate (FDR). B) Bar plots depicting KEGG pathways enriched in the gene list associated with DMCs found in promoters for each cluster shown in Figure 8D. C) Bar plots depicting GO: BP enriched in the gene list associated with DMCs in gene bodies for each cluster shown in Figure 8D. D) Bar plots depicting KEGG pathways enriched in the gene list associated with DMCs in gene bodies for each cluster shown in Figure 8D. E) Top transcription factor binding motifs that are enriched in each DMC cluster shown in Figure 8D. Bar plot reports the degree of statistical significance for each motif enrichment.

3.3.4 Hypomethylation occurs at CpG sites found in promoters of genes associated with immune activation.

To investigate which genes are targeted by DNA hypomethylation, which is a known regulatory mechanism for transcriptional expression, we first identified and characterized shared and unique HypoDMCs between timepoint comparisons (Fig. 10A). To gain insight into the biological processes regulated through DNAme changes during esophageal regeneration, we focused our analyses on HypoDMCs that were unique to each timepoint comparison. We identified 1,396 HypoDMCs unique to “NSC->Day1” (Fig. 10A, orange shaded region), of which, 53% were found in gene bodies and 12% were found in promoters (Fig. 10A-B). We identified 6,898 HypoDMCs unique to “NSC->Wk1” (violet shaded region), of which, 55% were found in gene bodies and 12% were found in promoters (Fig. 10A-B). For unique HypoDMCs occurring within promoters, GO enrichment analysis of associated genes revealed a strong enrichment in BPs involved in immune activation and inflammation (Fig. 10C). Specifically, for the genes associated with unique NS->Day1 HypoDMCs within promoters, we observed enrichment of BPs associated with NK T-cell activation and Interleukin-17 production, while genes associated with unique NSC->Wk1 HypoDMCs within promoters were enriched for leukocyte migration (Fig. 10C). To further identify signaling pathways that could be regulated by DNA hypomethylation within promoters, we performed pathway enrichment

analysis on associated genes using Protein Analysis Through Evolutionary Relationships (PANTHER) Pathway [75]. This analysis could identify novel pathways involved in esophageal tissue regeneration. The genes associated with unique NSC->Wk1 HypoDMCs within promoters were enriched for PANTHER pathways involved in T-cell activation, angiogenesis, and Wnt signaling (Fig. 10D).

As DNAme occurring within the gene body has also been shown to modulate gene expression, we performed enrichment analysis for unique HypoDMCs that fall within the gene body [92,93]. GO enrichment analysis of genes associated with unique NSC->Day1 HypoDMCs within gene bodies revealed low enrichment for BPs including cholesterol homeostasis and lipid homeostasis (Fig. 10E). In contrast, the genes that were unique to NSC->Wk1 HypoDMCs within gene bodies were associated with cell morphogenesis (Figure 7E). Genes associated with unique NSC->Wk1 HypoDMCs occurring in gene bodies were enriched for PANTHER pathways such as epidermal growth factor (EGF) and platelet-derived growth factor (PDGF) which are important signaling pathways involved in tissue regeneration and wound healing processes (Fig. 10F). Notably, unique NSC->Day1 HypoDMCs within promoters and within gene bodies were not significantly enriched for any PANTHER pathways, which may be attributable to the smaller total number of unique NSC->Day1 HypoDMCs. Interestingly, we found NSC->Wk1 HypoDMCs occur in the promoter of the gene encoding DNMT3A, which conducts de novo methylation and interacts with histone methyltransferases to regulate transcriptional activity. Both functions are critical for cell fate transitions and may contribute to cell proliferation and regeneration during wound healing processes [94].

Next, we sought to determine how changes in DNA methylation could impact the binding of specific regulatory factors. We identified binding motifs enriched in unique HypoDMCs using HOMER. Unique HypoDMCs were enriched for binding motifs associated with regulatory factors involved in immune activation and inflammation such as interferon regulatory factors (Irf, Irf8), CCAAT enhancer-binding protein (Cebp), Elf4, and PU.1 [95,96]. Motifs of RUNX TF family members, which have been shown to activate PI3K-Akt pathways, were also enriched at HypoDMCs (Fig. 10G) [97,98].

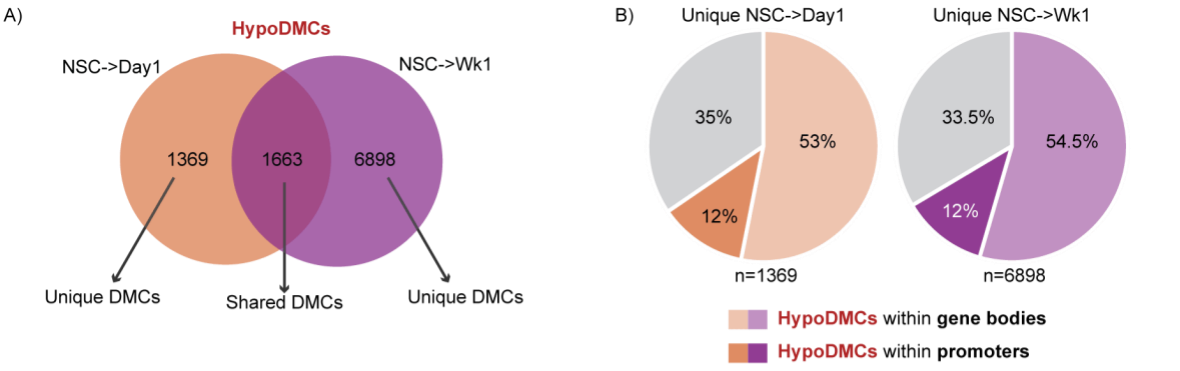
A)
HypoDMCs
NSC->Day1
NSC->Wk1
1369
1663
6898
Unique DMCs
Shared DMCs
Unique DMCs
B)
Unique NSC->Day1
Unique NSC->Wk1
35%
53%
12%
33.5%
54.5%
12%
n=1369
n=6898
HypoDMCs within gene bodies
HypoDMCs within promoters

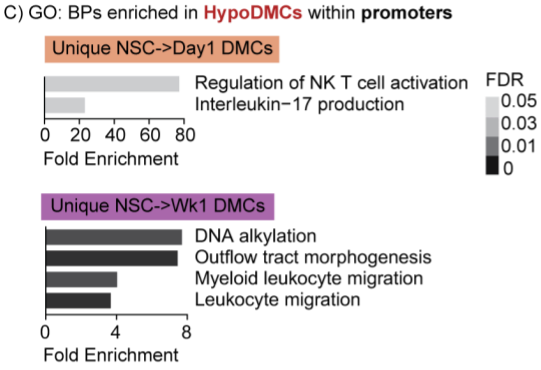
C) GO: BPs enriched in HypoDMCs within promoters
Unique NSC->Day1 DMCs
Regulation of NK T cell activation
Interleukin−17 production
0 20 40 60 80
Fold Enrichment
FDR
0.05
0.03
0.01
0
Unique NSC->Wk1 DMCs
DNA alkylation
Outflow tract morphogenesis
Myeloid leukocyte migration
Leukocyte migration
0 4 8
Fold Enrichment

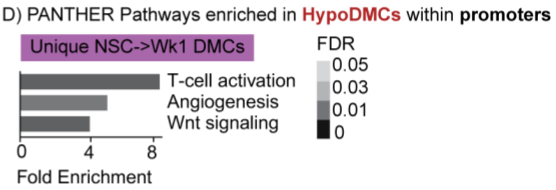
D) PANTHER Pathways enriched in HypoDMCs within promoters
Unique NSC->Wk1 DMCs
T-cell activation
Angiogenesis
Wnt signaling
0 4 8
Fold Enrichment
FDR
0.05
0.03
0.01
0

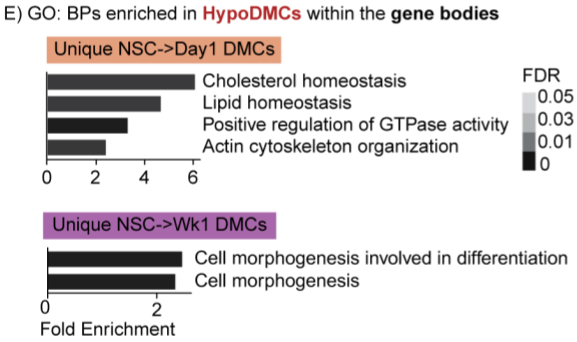
E) GO: BPs enriched in HypoDMCs within the gene bodies
Unique NSC->Day1 DMCs
Cholesterol homeostasis
Lipid homeostasis
Positive regulation of GTPase activity
Actin cytoskeleton organization
0 2 4 6
FDR
0.05
0.03
0.01
0
Unique NSC->Wk1 DMCs
Cell morphogenesis involved in differentiation
Cell morphogenesis
0 2
Fold Enrichment

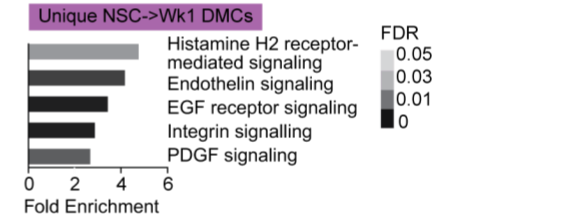
F) PANTHER Pathways enriched in HypoDMCs within gene bodies
Unique NSC->Wk1 DMCs
Histamine H2 receptor-mediated signaling
Endothelin signaling
EGF receptor signaling
Integrin signalling
PDGF signaling
0 2 4 6
Fold Enrichment
FDR
0.05
0.03
0.01
0

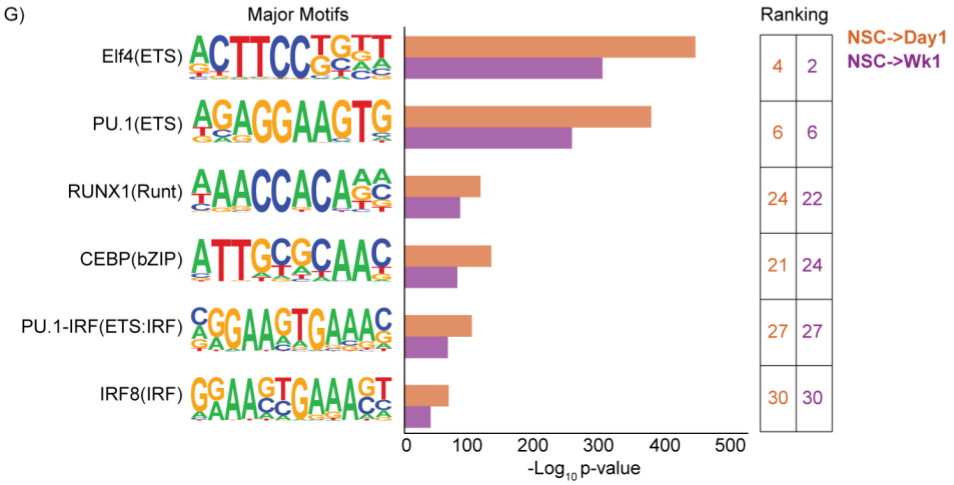
G)
Major Motifs
Ranking
NSC->Day1
NSC->Wk1
Elf4(ETS)
PU.1(ETS)
RUNX1(Runt)
CEBP(bZIP)
PU.1-IRF(ETS:IRF)
IRF8(IRF)
4 2
6 6
24 22
21 24
27 27
30 30
0 100 200 300 400 500
-Log10 p-value

Figure 10. Hypomethylation occurs at CpG sites found in promoters of genes associated with immune activation. A Venn diagram displaying shared and unique DMCs called among the comparison groups: NSC->Day1 (DMCs called at Day1 relative to NSC baseline), NSC->Wk1 (DMCs called at Wk1 relative to NSC baseline), Day1->Wk1 (DMCs called at Wk1 relative to Day1). DMCs were called at a threshold of 20% CpG methylation difference and q-value<0.01. The number of DMCs for each group comparison: NSC->Day1 (n=12,279), NSC-->Wk1 (n=34,506) and Day1->Wk1(1,467). B) Bar plot showing the number of hypermethylated and hypomethylated DMCs in each comparison group. The number of hypermethylated DMCs for the NSC->Day1 (n=9,247) and NSC->Wk1 (25,945) groups. The number of hypomethylated DMCs for the NSC->Day1 (n=3,032) and NSC->Wk1 (8,561) groups. C) Density plot depicting the distribution of hypermethylated and hypomethylated DMCs in each comparison group. D) Top: For shared DMCs that are represented in each individual sample with ≥5x coverage (n=3,494), corresponding CpG methylation levels within in each sample are shown in the heatmap. Euclidean hierarchical clustering was performed with pHeatmap package (version 1.0.12) using the ward.D2 clustering method in RStudio (version 4.0.5). Three clusters with different temporal DNA methylation dynamics were identified. Bottom: Pie charts displaying the distribution of DMCs corresponding to each cluster that fall within a gene body, promoter, or neither.

3.3.5 Hypermethylation in post-surgical repair timepoints targets biological processes involved in PI3K-Akt signaling.

We identified 5,256 HyperDMCs unique to “NSC->Day1” (Fig. 11A, orange shaded region), of which, 46% were found in gene bodies and 10% were found in promoters (Fig. 11A-B). We identified 21,954 HyperDMCs unique to “NSC->Wk1” (violet shaded region), of which, 55% were found in gene bodies and 10 % were found in promoters (Fig. 11A-B). GO enrichment analysis revealed that unique NSC->Day1 HyperDMCs occur within promoters of genes involved in receptor protein tyrosine kinase signaling and growth (Fig. 11C), while unique NSC->Wk1 HyperDMCs occur in genes involved in lipid oxidation and angiogenesis (Fig. 11C). PANTHER Pathway enrichment analysis revealed that unique NSC->Day1 HyperDMCs occur in promoters of genes involved in the VEGF signaling which is the major regulator of angiogenesis [99]. Unique NSC->Wk1 HyperDMCs occur in promoters of genes involved in muscarinic acetylcholine receptors 1 and 3 signaling (Fig. 11D).

We focused on hypermethylation that occurs at CpG sites within gene bodies which has been shown to upregulate gene expression for unique NSC->Day1 and NSC->Wk1 HyperDMCs [93,100]. Interestingly, both unique NSC->Day1 and NSC->Wk1 HyperDMCs occur within the gene bodies of genes involved in developmental BPs such as cell morphogenesis and tube development (Fig. 11E). This observation may suggest development BPs are upregulated in regenerating esophageal tissues following surgical injury. Most notably, PANTHER Pathway enrichment analysis revealed that unique NSC->Day1 and NSC->Wk1 HyperDMCs occur within gene bodies of genes involved in signaling pathways that have been previously implicated in tissue regeneration such as EGF, PDGF and Ras [87,89,101]. Ras activates PI3K-Akt signaling which we previously showed was involved in neotissue formation following surgical repair with BLSF grafts (Fig. 11F) [66,102]. P13K has also been shown to mediate PDGF and VEGF signaling [88,103].

Hypermethylation of CpG sites can decrease the accessibility of TF binding to regulatory regions and can modulate the expression of genes and their downstream targets *[104,105]*. Motif analysis on unique HyperDMCs revealed an enrichment for motifs associated with the Forkhead (FOX) TF family (Foxa1, Foxo3, Foxm1, and Foxa2). The observed enrichment was more significant for NSC->Wk1 HyperDMCs than NSC->Day1 HyperDMCs (Fig. 11G). PI3K-Akt activation inhibits members of the Forkhead TF family which target genes involved in apoptotic responses and thereby promotes cell survival [106,107].

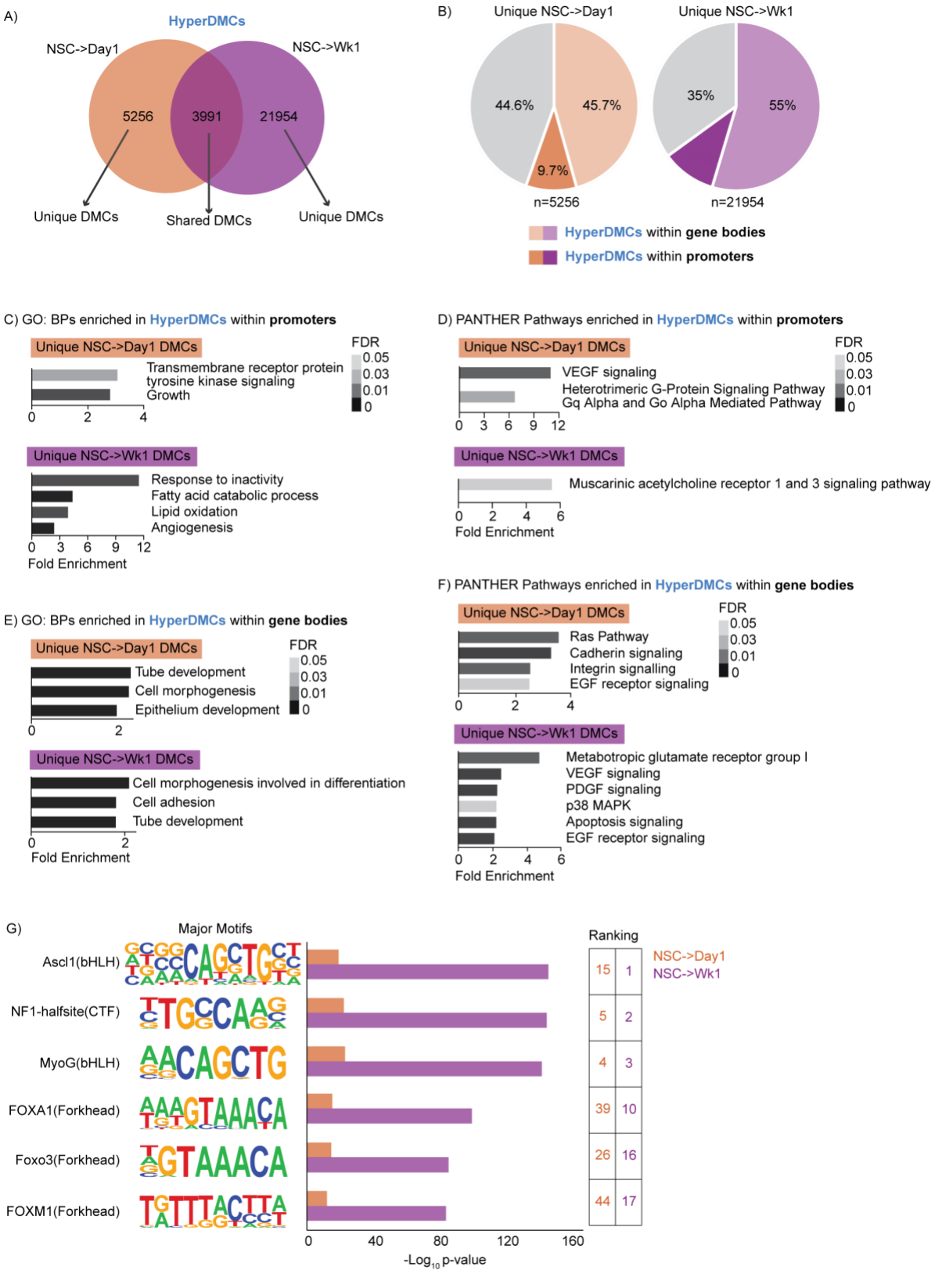
A)
HyperDMCs
NSC->Day1
NSC->Wk1
5256
3991
21954
Unique DMCs
Shared DMCs
Unique DMCs
B)
Unique NSC->Day1
Unique NSC->Wk1
44.6%
45.7%
9.7%
35%
55%
n=5256
n=21954
HyperDMCs within gene bodies
HyperDMCs within promoters
C) GO: BPs enriched in HyperDMCs within promoters
Unique NSC->Day1 DMCs
Transmembrane receptor protein tyrosine kinase signaling
Growth
FDR
0.05
0.03
0.01
0
Unique NSC->Wk1 DMCs
Response to inactivity
Fatty acid catabolic process
Lipid oxidation
Angiogenesis
Fold Enrichment
D) PANTHER Pathways enriched in HyperDMCs within promoters
Unique NSC->Day1 DMCs
VEGF signaling
Heterotrimeric G-Protein Signaling Pathway
Gq Alpha and Go Alpha Mediated Pathway
Unique NSC->Wk1 DMCs
Muscarinic acetylcholine receptor 1 and 3 signaling pathway
Fold Enrichment
E) GO: BPs enriched in HyperDMCs within gene bodies
Unique NSC->Day1 DMCs
Tube development
Cell morphogenesis
Epithelium development
Unique NSC->Wk1 DMCs
Cell morphogenesis involved in differentiation
Cell adhesion
Tube development
Fold Enrichment
F) PANTHER Pathways enriched in HyperDMCs within gene bodies
Unique NSC->Day1 DMCs
Ras Pathway
Cadherin signaling
Integrin signalling
EGF receptor signaling
Unique NSC->Wk1 DMCs
Metabotropic glutamate receptor group I
VEGF signaling
PDGF signaling
p38 MAPK
Apoptosis signaling
EGF receptor signaling
Fold Enrichment
G)
Major Motifs
Ascl1(bHLH)
NF1-halfsite(CTF)
MyoG(bHLH)
FOXA1(Forkhead)
Foxo3(Forkhead)
FOXM1(Forkhead)
Ranking
NSC->Day1
NSC->Wk1
15 1
5 2
4 3
39 10
26 16
44 17
-Log10 p-value

Figure 11. Hypermethylation at post-surgical repair timepoints targets genes involved in PI3K-Akt signaling. A) Venn diagram displaying shared and unique hypermethylated DMCs (HyperDMCs) between NSC->Day1 (n=9,247) and NSC->Wk1 (n=25,945) groups. B) Pie charts showing the proportions of unique HyperDMCs located within gene bodies, promoters, or neither for NSC->Day1 and NSC->Wk1 comparison groups. Panels C-F) Plots depicting enriched GO: biological processes (BPs) and PANTHER pathways. The x-axis indicates fold enrichment and the colors indicate the false-discovery rate (FDR). C) Bar plot depicting GO: (BPs) enriched for genes associated with HyperDMCs found within promoters that are unique to NSC->Day1 (top) or that are unique to NSC->Wk1 (bottom). 460 and 1,438 genes were associated with unique NSC->Day1 and NSC->Wk1 HyperDMCs within promoters, respectively. D) Bar plot depicting PANTHER pathways enriched for genes associated with HyperDMCs found within promoters that are unique to NSC->Day1 (top) or that are unique to NSC->Wk1 (bottom). E) Bar plot depicting GO: BPs enriched for genes associated with HyperDMCs found within gene bodies that are unique to NSC->Day1 (top) or that are unique to NSC->Wk1 (bottom). 1,715 and 4,999 genes were associated with unique NSC->Day1 and NSC->Wk1 HyperDMCs within gene bodies, respectively. F) Bar plot depicting PANTHER pathways enriched for genes associated with HyperDMCs found within gene bodies that are unique to NSC->Day1 (top) or that are unique to NSC->Wk1 (bottom). G) Transcription factor binding motifs enriched for unique NSC->Day1 and NSC->Wk1 HyperDMCs. Motif logos are shown in the left column. Bar plot shows the degree of statistical significance for each motif enrichment. Motifs were ranked by $-\log_{10}$(*p*-values) in each condition calculated by HOMER.

3.3.6 Putative enhancers lifted over from the human genome show dynamic methylation during esophageal regeneration

Given that we observe protein expression changes that correlate with DNAme changes at proximal regulatory elements (promoters and gene bodies), we also aimed to characterize differential methylation across distal regulatory elements. Due to the lack of annotations available for regulatory genomic features in the rat genome, we used the UCSC liftOver tool to lift human genome annotations to the rat genome to analyze differential methylation across conserved distal regulatory regions (Fig. 12A) [80]. First, we investigated the DNAme dynamics of CpGs that occur within conserved esophagus enhancer regions. Human esophagus gene-enhancer interaction networks were obtained from EnhancerAtlas 2.0 and lifted over to the rat genome with a 91% liftOver conversion

rate [80]. We found that the majority of the lifted esophagus enhancers resided within 100 kb of their associated gene's transcription start site (TSS) in the rat genome (Fig. 13A). To obtain regional resolution of DNAme dynamics, we determined the average methylation levels for CpGs found across lifted esophagus enhancer regions. Lifted enhancers were considered to be differentially methylated if the average methylation level assigned to the lifted enhancer between the NSC condition and at each surgical timepoint exhibited a difference of at least 20%. Global analysis revealed CpGs that occur across lifted esophagus enhancers were hypermethylated at Day1 and Wk1 compared to NSC (Fig. 12B). We then focused on characterizing the methylation dynamics across conserved esophagus enhancers that were associated with genes, which we refer to as gene-enhancer pairs, that were also previously identified as DEPs during esophageal regeneration [66]. We found a comparable number of gene-enhancer pairs associated with genes encoding upregulated and downregulated DEPs in the NSC->Day1 comparison, while there were more gene-enhancer pairs associated with genes encoding upregulated DEPs compared to downregulated DEPs in the NSC->Wk1 comparison (Fig. 13B). We determined the likelihood that differentially methylated lifted esophagus enhancers were associated with genes that encode DEPs using a logarithmic odds ratio (logOR) analysis (see Methods). We analyzed the differentially methylated lifted gene-enhancer pairs and DEP directional expression for each timepoint comparison which revealed that hypomethylated gene-enhancer pairs were more strongly associated with DEPs that were upregulated at both timepoint comparisons (Fig. 12C; Table 3). Our results suggest that the likelihood of hypermethylated lifted esophagus enhancers was positively associated with downregulated DEPs and negatively associated with

upregulated DEPs at both timepoint comparisons (Fig. 12C; Table 3). Similarly, we found a subtle association between hypomethylated lifted esophagus enhancers which were positively associated with upregulated DEPs and negatively associated with downregulated DEPs (Fig. 12C; Table 3C).

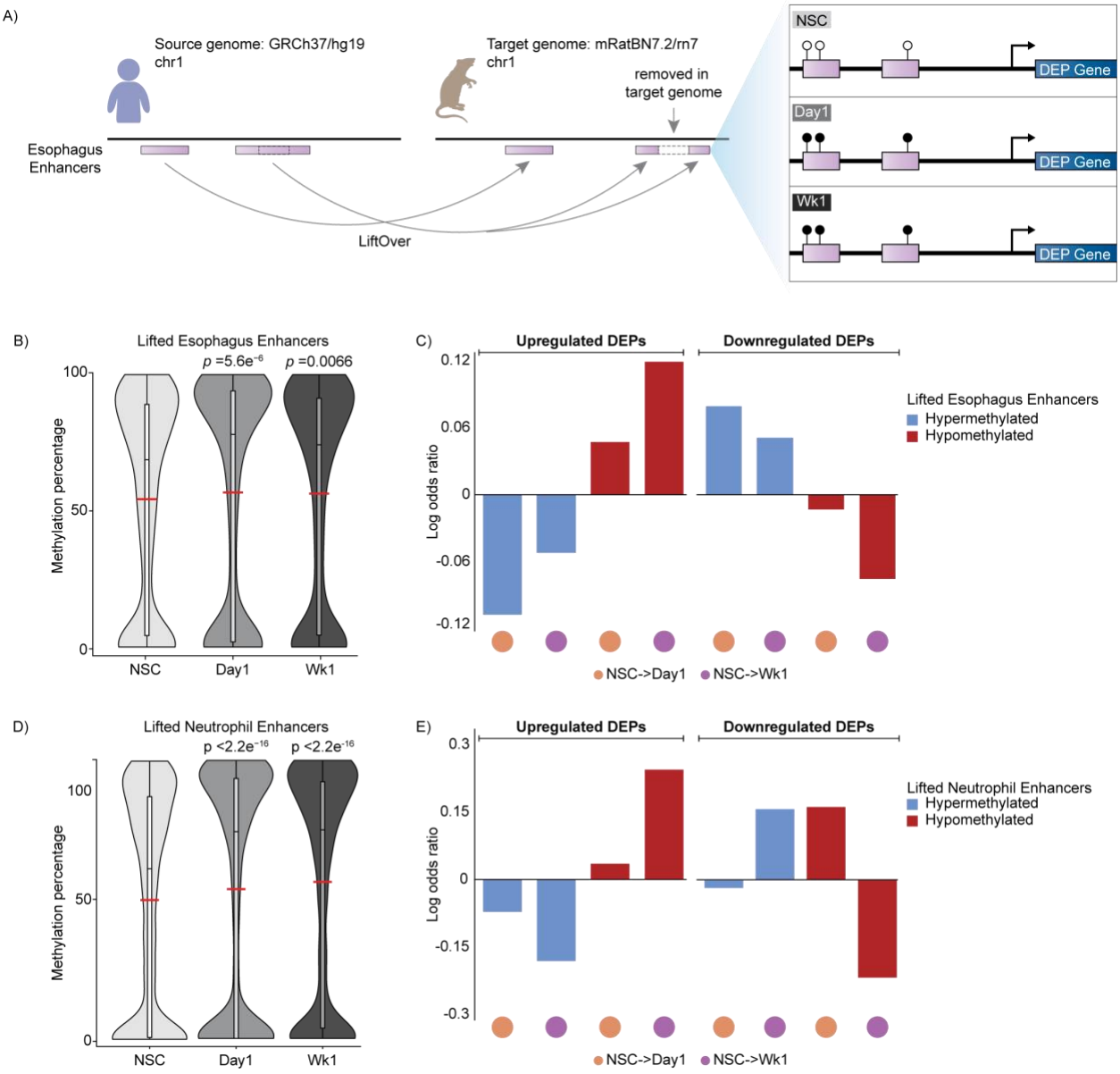

Figure 12. Conserved enhancer regions exhibit differential methylation that is largely associated with upregulation of differentially expressed proteins. A) Schematic illustration of experimental workflow for characterizing methylation changes in conserved genomic regions between GRCh37/hg19 and mRatBN7.2/rn7 genomes. Black circles represent methylated CpGs, while white circles represent unmethylated CpGs. In

this scenario, the enhancer of interest is hypermethylated at Day1 and Wk1 compared to the NSC. B) Violin plots depicting the distribution of CpG methylation percentage for all CpGs within lifted esophagus enhancers (n=13,189) for each experimental timepoint. The *p*-values were calculated with Wilcoxon rank-sum test. C) Bar plots show the logOR between differentially methylated lifted esophagus enhancers that were hypomethylated (red) and hypermethylated (blue) and DEPs for each timepoint comparison. The colored circles at the bottom reflect timepoint comparisons (i.e., orange indicates NSC->Day1 and violet indicates NSC->Wk1). LogOR significance was calculated with Fisher's exact test. Note: LogOR were *ns*. D) Violin plots depicting the distribution of CpG methylation percentage for all CpGs within lifted neutrophil enhancer regions (n=11,294) for each experimental timepoint. The *p*-values were calculated with Wilcoxon rank-sum test. E) Bar plots show the logOR between differentially methylated lifted neutrophil enhancers that were hypomethylated (red) and hypermethylated (blue) and DEPs for each timepoint comparison. The colored circles at the bottom reflect timepoint comparisons (i.e., orange indicates NSC->Day1 and violet indicates NSC->Wk1). LogOR significance was calculated with Fisher's exact test. Note: LogOR were *ns*.

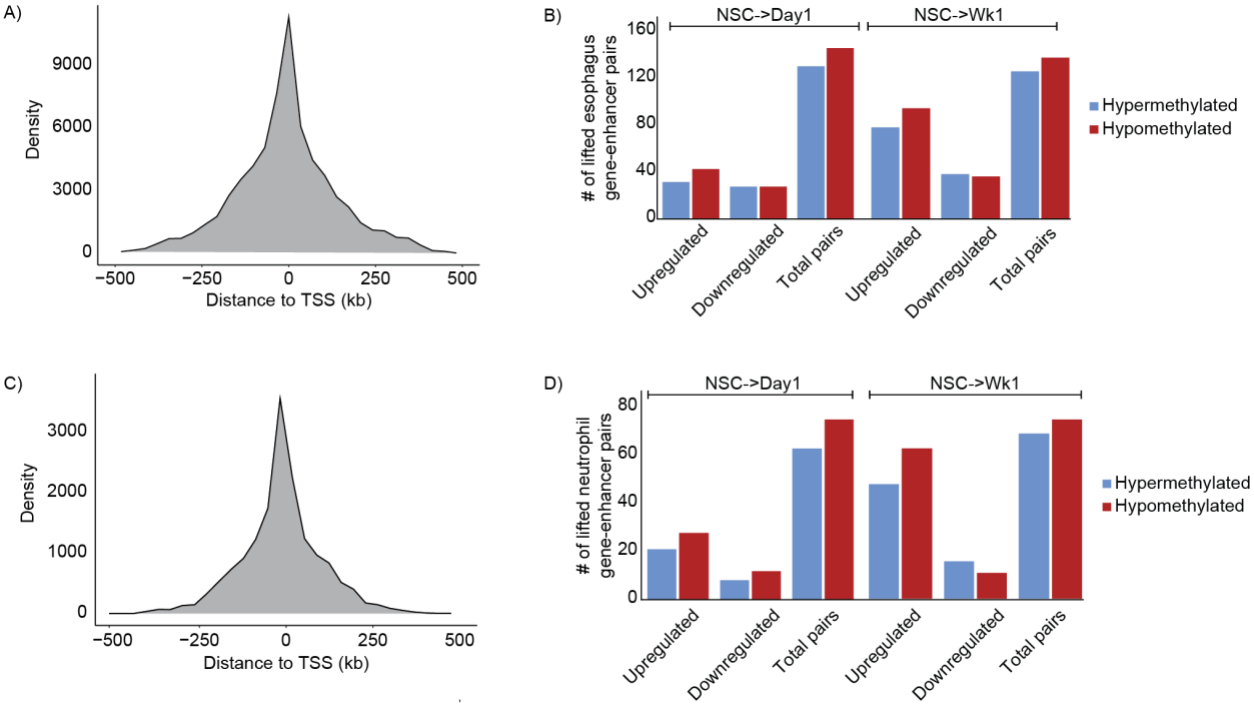

Figure 13. Methylation levels across lifted esophagus enhancers and lifted neutrophil enhancers that are associated with genes which encode DEPs involved in esophageal regeneration. A) Density plot showing the distribution of distance to the TSS for lifted esophagus enhancers. A positive genomic coordinate indicates that the lifted enhancer is located downstream of its associated gene's TSS, while a negative genomic coordinate indicates that the lifted enhancer is located upstream of its associated gene's TSS. B) Bar plots show the total number of unique lifted esophagus gene-enhancer pairs that were hypermethylated (blue) or hypomethylated (red) based on

average methylation level across the enhancer for each timepoint comparison. Bar plots show the number of differentially methylated lifted esophagus gene-enhancer pairs that occur in genes encoding previously identified upregulated and downregulated DEPs for each timepoint comparison. C) Density plot showing the distribution of distance to the TSS for lifted neutrophil enhancers. D) Bar plots show the total number of unique lifted neutrophil gene-enhancer pairs that were hypermethylated (blue) or hypomethylated (red) based on average methylation level across the enhancer for each timepoint comparison. Bar plots show the number of differentially methylated lifted neutrophil gene-enhancer pairs that occur in genes encoding previously identified upregulated and downregulated DEPs for each timepoint comparison.

Group	Differentially methylated esophagus enhancers	Upregulated DEPs		Downregulated DEPs	
		logOR	p-value	logOR	p-value
NSC->Day1	Hypermethylated	-0.1079	0.3511	0.0789	0.5097
NSC->Wk1		-0.0519	0.5825	0.0510	0.6402
NSC->Day1	Hypomethylated	0.0473	0.652	-0.0132	1
NSC->Wk1		0.1194	0.2362	-0.0752	0.4947

Table 3. LogOR for lifted esophagus Enhancer-Gene Interactions. Fisher's exact test was used to determine the significance of odds ratios using R. Abbreviations: Logarithmic odds ratio (logOR); Differentially expressed proteins (DEPs); nonsurgical control (NSC).

In our study, we showed that NSC->Day1 HypoDMCs were associated with genes involved in immune activation and this finding is supported by previous work that found neutrophils and mononuclear cells infiltrate the surgical implant site 1-day after BLSF surgery [66]. Based on these observations, we also investigated the DNAme dynamics of CpGs that occur across conserved neutrophil enhancer regions. Human neutrophil gene-enhancer interaction regions for the cell line (HL-60) were obtained from EnhancerAtlas 2.0 and lifted over to the rat genome with a 91% liftOver conversion rate [80]. Similar to the lifted esophagus enhancers, we characterized the average methylation levels for CpGs across lifted neutrophil gene-enhancer pairs and used a 20% methylation difference threshold to determine differentially methylated neutrophil gene-enhancer regions. We found that the majority of lifted neutrophil enhancers resided within 100 kb of their associated gene's TSS in the rat genome (Fig. 13C). Global analysis of

methylation levels across lifted neutrophil enhancers showed that CpGs were hypermethylated at Day1 and Wk1 compared to NSC (Fig. 12D). We focused on characterizing the methylation dynamics across conserved neutrophil gene-enhancer regions that were associated with genes that were previously identified as DEPs during esophageal regeneration [66]. We found a high number of gene-enhancer pairs associated with genes encoding upregulated compared to genes encoding downregulated DEPs for both timepoint comparison (Fig. 13D). We performed a logOR analysis for differentially methylated lifted neutrophil gene-enhancer regions and DEP expression. Hypomethylated lifted neutrophil gene-enhancer regions showed the strongest association with upregulated DEPs for the NSC->Day1 comparison (Fig. 12E; Table 4). In contrast, hypomethylated lifted neutrophil gene-enhancer regions were associated with both upregulated and downregulated DEPs for the NSC->Wk1 timepoint comparison (Fig. 12E; Table 4). We found a slight association between hypermethylated lifted neutrophil gene-enhancer regions and upregulated DEPs and downregulated DEPs for the NSC->Wk1 (Fig. 12E; Table 4). Our results suggest that the likelihood of hypomethylated lifted neutrophil enhancers in the NSC->Wk1 was positively associated with upregulated DEPs and was negatively associated with upregulated DEPs, while hypermethylated lifted neutrophil enhancers likelihood was negatively associated with upregulated DEPs and positively associated with downregulated DEPs (Fig. 12E; Table 4). The implications of methylation dynamics of lifted neutrophil enhancers in the NSC->Day1 comparison was less clear but may reflect changes in cell populations found at the implant site, specifically infiltrating neutrophils after surgical repair.

Group	Differentially methylated neutrophil enhancers	Upregulated DEPs		Downregulated DEPs	
		logOR	p-value	logOR	p-value
NSC->Day1	Hypermethylated	-0.0722	0.646	-0.0183	1
NSC->Wk1		-0.1816	0.2431	0.1565	0.3606
NSC->Day1	Hypomethylated	0.0347	0.8836	0.1613	0.4048
NSC->Wk1		0.2453	0.1083	-0.2175	0.2161

Table 4. LogOR for lifted neutrophil Gene-Enhancer Interactions. Fisher's exact test was used to determine the significance of odds ratios using R. Abbreviations: Logarithmic odds ratio (logOR); Differentially expressed proteins (DEPs); nonsurgical control (NSC).

3.4 CONCLUSION

The application of bioengineered biomaterials in graft implants has therapeutic potential to improve the treatment and prognosis of patients with esophagus defects and other gastroenterological diseases *[64,65]*. Several pathways have been implicated in epithelial esophageal regeneration following surgical repair with acellular grafts previously in rats; however, the role of DNA methylation in tissue regeneration are not well understood [65,66]. In this report, we characterize changes in CpG methylation with RRBS in rat esophageal tissues following onlay esophagoplasty with BLSF grafts and during neoepithelial formation. Our findings indicate global hypermethylation occurs after surgery with acellular grafts at Day1 and Wk1 which correspond to post-surgical timepoints associated with neotissue formation (Fig. 5).

Interestingly, while the majority of DMCs were hypermethylated in post-surgical timepoint samples, we found hypomethylated DMCs occur in promoters and the gene body of genes that are involved in immune activation and inflammation. We postulate that this subset of hypomethylated DMCs may reflect changes in the cell populations present in the surgical implant site. Histological and proteomics findings from previous work found that inflammatory cells including neutrophils infiltrate surgical wounds sites one day after

esophageal reconstruction [66]. Our results showed that hypomethylation occurs in CpGs of genes involved in immune activation after surgery. It is unclear whether the hypomethylated DMCs we identified reflect a new population of infiltrating immune cells or changes in DNAme levels of other cell types at the surgical implant site. Future studies using single-cell techniques can help identify cell-type specific epigenetic signatures in esophageal tissues during regeneration [108,109].

Surprisingly, we found that site-specific hypermethylation appears to target several pathways which have been implicated in tissue regeneration in previous studies *[66]*. Specifically, it has been shown that epithelial esophageal regeneration is mediated, in part, through pro-survival stimuli and the inhibition of apoptotic pathways such as caspase and Baculoviral IAP Repeat Containing 3 (Birc3) [66]. Our results showed that CpG hypermethylation occurs in promoters and gene bodies of genes involved in cytokine pathways which regulate cell growth and apoptotic signaling such as VEGF, PDGF and EGF receptor signaling (Fig. 11C-D) [99]. It has been demonstrated that promoter hypermethylation is important for repressing gene transcription, while gene body hypermethylation can upregulate gene expression [110]. Our findings provide evidence that epigenetic mechanisms, specifically promoter hypermethylation, may contribute to the inhibition of apoptotic signaling during regeneration. Additionally, we found HyperDMCs were enriched for several motifs in the Forkhead TF family that promote target genes involved in apoptotic signaling (Fig. 11G) [106]. Additional studies are required to assess how hypermethylation of Forkhead binding motifs affects transcription factor binding and gene regulation.

Whether the DNAme dynamics we observed here reflect a transient signaling response induced by surgical injury or changes to the cell populations found in the regenerating tissues is not clear. While further gene expression analyses, protein-DNA binding experiments, and gene-enhancer interaction network studies are necessary to elucidate how these pathways and their molecular components are precisely affected by changing DNAme dynamics, our work offers novel insight into potential epigenetic mechanisms that may be involved in esophageal regeneration, thereby identifying promising potential therapeutic targets that could be modulated to improve the regeneration process.

Chapter 4

Activation of a bacterial flow sensor by hypochlorous acid from stimulated neutrophils

Bacteria sense environmental stressors and activate responses to improve their survival in harsh growth conditions. Neutrophils respond to the presence of bacteria by producing oxidative antibacterial species including hypochlorous acid (HOCl). However, the extent that bacteria detect activated neutrophils or HOCl has not been known. Here, we report that the opportunistic bacterial pathogen *Pseudomonas aeruginosa* responds to activated neutrophils by activating the *fro* system, which regulates the expression of antioxidative factors. We show that this response is specific to HOCl and that other oxidative factors including H_2O_2, do not trigger a *fro* response. The *fro* system has been previously shown to detect flow that is present in host vasculature, such as in animal circulatory systems. Our data thus suggest a model in which *fro* serves as an early host detection system in *P. aeruginosa* that improves its survival against neutrophil-mediated defenses, which could promote colonization in human tissue and increase pathogenicity.

4.1 INTRODUCTION

P. aeruginosa is a Gram-negative bacterium that is a major cause of acute hospital-acquired infections and a significant threat for antibiotic-resistant infections *[111]*. To survive in a broad range of conditions, this bacterium has evolved signaling pathways that relay information about changes in nutrients, chemical gradients, and mechanical forces such as those generated by flow, and stimulates responses that

promote survival [112,113]. Many of these signaling pathways improve the bacterium's survival in hosts in particular. Understanding how such environmental-sensing pathways detect and respond to host cues is critical for improving treatments of bacterial infections.

Mammalian host immune systems respond to the presence of bacterial pathogens by recruiting immune cells to sites of infection. Neutrophils are among the first and most abundant immune cells recruited to inflamed or damaged tissues [26]. Neutrophils are stimulated into an activated state by the presence of the bacterial components, including the membrane constituent lipopolysaccharide. Activated neutrophils kill bacteria through a number of mechanisms, including producing respiratory burst products such as reactive oxygen species (ROS) and reactive chlorine species (RCS) [114,115]. While the toxic effects of ROS on bacteria are understood, far less is known about how bacteria are affected by RCS [116,117]. Hypochlorous acid (HOCl) is a major neutrophil RCS that has strong bactericidal activity towards bacteria [118,119]. HOCl is formed through the activity of myeloperoxidase with H_2O_2 and chlorine ions [114,115,120]**.** P. aeruginosa is a potent activator of neutrophil respiratory bursts [121]**.** However, whether and how P. aeruginosa detects and responds to neutrophil respiratory bursts is not understood.

Recently, it was reported that *P. aeruginosa* detects the flow of fluids via the flow-regulated operon fro [113]. Flow is ubiquitous in the lung and in the circulatory system, which neutrophils and other immune cells must travel through to reach infected sites. The fro system could thus enable P. aeruginosa to detect the presence of flow-associated host environments and immune system components. *P. aeruginosa* induces

fro operon expression during infections in humans [113,123] (Fig. 14A).The operon consists of the genes *froABCD* (*PA14_21570*, *PA14_21580, PA14_21590, PA14_21600*). FroB is predicted to localize in cytoplasm while FroC and FroD are predicted to localize to the inner membrane [124]. The *fro* operon is regulated by two upstream genes, *froR* (*PA14_21550)* and *froI* (*PA14_21560*), which are sigma and anti-sigma factors, respectively [125]. Overexpression of *froR* increases *fro* expression whereas overexpression of *froI* eliminates *fro* induction [113]. Flow activates FroR-dependent transcription of *froABCD* through an unknown mechanism.

We investigated whether the *fro* system directly responds to components of the circulatory system. Here, we show that the expression of the *fro* system is upregulated by activated neutrophils. We determine that HOCl is a critical component of the neutrophil activation that is responsible for the *fro* upregulation and that its upregulation reduces the bactericidal effects of HOCl. These data suggest a novel mechanism by which a bacterial defense system is primed to detect host immune system activity through both flow and the presence of the immune cell effector HOCl and responds by producing protective antioxidant proteins.

4.2 MATERIALS AND METHODS

Strains and Growth Conditions

Experiments were performed using the *P. aeruginosa* strain AL143, which contains the *yfp* gene integrated between *froA* and *froB* and a constitutively-expressed *mCherry* gene [113]. For experiments with response of *P. aeruginosa* against NaOCl Δ*froR* and Δ*froI* mutant strains were used [113]. Strains were streaked onto LB-Miller (BD Biosciences, Franklin Lakes, NJ) petri dishes containing 2% Bacto agar (BD

Biosciences, Franklin Lakes, NJ), incubated at 37 °C to obtain single colonies, and inoculated into MinA minimal medium, which contains per 1 L of water: 4.5 g KH_2PO4, 10.5 g K_2HPO_4, 1 g $(NH_4)_2SO_4$, 1 mM $MgSO_4$ and 0.2 % (w/v) sodium citrate *[126]*. Strains were cultured in minimal medium for 18 hours in a roller drum spinning at 200 rpm at 37 °C, diluted 1:1000 into the same medium supplemented with oxidative or antioxidative agents, conditioned medium from neutrophils, or were not supplemented, cultured for 1 hour at 37 °C, and imaged using microscopy.

Phase Contrast and Fluorescence Microscopy

Bacteria were immobilized on 1% agarose pads containing minimal medium and imaged immediately. Images were acquired using a Nikon Eclipse Ti-E microscope (Nikon, Melville, NY) containing a Nikon 100X Plan Apo (1.45 N.A.) objective, a Nikon Ph3 phase contrast condenser annulus, a Sola light engine (Lumencor, Beaverton, OR), an LED-DA/FI/TX filter set (Semrock, Rochester, NY) for visualizing the mCherry fluorescence spectrum containing a 409/493/596 dichroic and 575/25 nm filters for excitation and 641/75 nm filters for emission, an LED-CFP/YFP/MCHERRY filter set (Semrock) for visualizing YFP fluorescence containing a 459/526/596 dichroic and 509/22 nm filters for excitation and 544/24 nm filters for emission, and a Hamamatsu Orca Flash 4.0 V2 camera (Hamamatsu, Bridgewater, NJ).

Images were acquired using Nikon NIS-Elements and analyzed using custom built software written previously [127] in Matlab (Mathworks, Natick, MA). See the “Code availability” section below to download code. Briefly, cell masks were determined from phase contrast images using an edge-detection algorithm. The YFP to mCherry fluorescence ratios in the masked cell areas were computed. The expression of *fro* is

quantified as the ratio of YFP to mCherry fluorescence in individual *P. aeruginosa*, which is averaged over at least one hundred *P. aeruginosa*. A minimum of 100 cells were imaged and analyzed in each experiment.

Growth Curves

Growth curve experiments were performed using a Synergy HTX multi-mode plate reader and sterile, tissue-culture treated, clear bottom, black polystyrene 96-well microplates (Corning, Corning, NY) containing 200 µL of culture in each well. The temperature set point was 37 °C and preheated before beginning measurements. For experiments performed with stationary phase bacteria, overnight cultures of bacteria were grown for 18 hours at 37 °C in the roller drum at 200 rpm to saturation, diluted into minimal medium to an optical density at 600 nm (OD_{600}) of 0.01 containing NaOCl, H_2O_2, HNO_3 or no supplement. Plates were incubated at 37 °C with continuous orbital shaking with an amplitude of 3 mm at the frequency of 180 cycles per minute and measured for OD_{600} every 20 minutes.

Cell size analysis

P. aeruginosa were cultured for 18 hours at 37 °C in a roller drum spinning at 200 rpm, diluted 1:1000 into fresh minimal medium, treated 1 µM NaCl, 200 µM HCl or with serial dilutions of NaOCl, H_2O_2, HNO_3 or media only, and incubated at 37 °C in 250 mL flasks for 3 hours with shaking at 225 rpm. Cells were immobilized on 1% agarose pads containing minimal medium, imaged using phase contrast microscopy, and analyzed using the edge detection image analysis tools in Matlab described above. The total pixel area of each individual cell was determined by computing the mask area and converting

from pixels to μm^2 by multiplying the mask area by a factor of 0.004225 μm^2/pixel to account for the microscope camera pixel size and objective magnification.

Neutrophil isolation

Blood samples from healthy donors between 18 to 65 years old were collected at the Institute for Clinical and Translational Science at the University of California, Irvine, through approved protocols with the UCI Institutional Review Board, and informed consent was obtained from all donors. Neutrophils were prepared essentially as described in [128]. Briefly, 3% dextran (Leuconostoc spp, Mr 450,000-650,000, Sigma-Aldrich, St. Louis, MO) in PBS (Gibco, ThermoFisher, Waltham, MA) was used to separate red blood cells (RBCs) from whole blood. Neutrophils were purified from the remaining cells by overlaying on a Ficoll density gradient (GE Healthcare, Chicago, IL) following centrifugation in Ficoll-Paque Centrifugation Media (GE Healthcare, Chicago, IL) for 25 minutes at 500 × g. The remaining RBCs were lysed using RBC Lysis Buffer (Fisher Scientific, Hampton, NH), and neutrophils were resuspended in RPMI 1640 medium (ATCC, Manassas, VA) and purity was assessed by flow cytometry using the ACEA NovoCyte Flow Cytometer and fluorescent antibodies APC-CD11b, FITC-CD16 and PE-CD66b (eBioscience, San Diego, CA). Neutrophils were immediately used for neutrophil stimulation or co-incubation experiments with *P. aeruginosa*. This procedure routinely yielded greater than 95% CD11B-positive neutrophil populations.

Tissue culturing

J774.1 mouse macrophages (ATCC) or primary neonatal normal human dermal fibroblasts (Neo-NHDF) (ATCC) were cultured in 10 mL DMEM (Gibco, ThermoFisher) in T75 flasks (VWR, Radnor, PA) at 37 °C with 5% CO_2. Macrophages were passaged

every three days through scraping and Neo-NHDF cells were passaged every 5 days through trypsinization.

Co-incubation of mammalian cells with P. aeruginosa

P. aeruginosa were cultured for 18 hours in minimal medium, centrifuged at 4600 x g for 2 minutes and resuspended in DPBS (Gibco, ThermoFisher) three times, and diluted to a final OD_{600} of 0.2. Macrophages or Neo-NHDF cells that were harvested from growth flasks, or freshly prepared neutrophils, were washed three times by centrifuging at 300 x g for 5 minutes and resuspending in DPBS, and 1 mL aliquots containing 4 x 10^5 cells/mL were transferred into flat-bottom dishes. *P. aeruginosa* culture was added to the cells at a multiplicity of infection of 10 and incubated at 37 °C with CO_2 for 30 minutes. Dishes were aspirated until approximately 20 µL of media remained and pads consisting of 1 % agarose containing DPBS were placed on top of the samples in the dishes to immobilize bacteria and cells. Samples were imaged immediately using microscopy.

Preparation of neutrophil-stimulated conditioned medium

Approximately 2 million/mL of freshly harvested neutrophils were incubated at 37 °C in a roller drum spinning at a speed of 4 rotations per minute in PBGT medium (10 mM phosphate buffer pH 7.4 (2.46 mM monobasic with 7.54 mM dibasic sodium phosphate), 140 mM sodium chloride, 10 mM potassium chloride, 0.5 mM magnesium chloride, 1 mM calcium chloride, 1 mg/mL glucose, and 5 mM taurine [129]). Neutrophils were supplemented with 100 ng/mL of PMA or left untreated for 1 hour, and were separated from the supernatant by 5-minute centrifugation at 4,600 x g at 25 °C. The supernatant was isolated and used as conditioned medium. *P. aeruginosa* were cultured in minimal

medium for 18 hours at 37 °C in a roller drum spinning at 200 rpm, diluted 1:1000 in conditioned media with or without the addition of 100 µM methionine, and incubated for 3 hours. Bacterial culture from each sample was concentrated using cellulose syringe filters with a 0.22 µm pore size (Millipore, Burlington, MA). *P. aeruginosa* cells were immobilized on 1% agarose pads and imaged. Data analysis was performed as described in the "cell size analysis" methods section.

Antioxidant treatments

P. aeruginosa cultured for 18 hours at 37 °C in a roller drum spinning at 200 rpm, diluted 1:1000 into fresh minimal medium were diluted 1:1000 into minimal medium alone or supplemented with 1 µM NaOCl with an addition of methionine (1 µM, 10 µM, 100 µM), β-mercaptoethanol (βME) (1 µM, 10 µM, 100 µM) or cysteine (0.1 µM, 1 µM, 10 µM). 50 mL of each bacterial culture was incubated at 37 °C in 250 mL flasks for 3 hours with shaking at 225 rpm. Data analyses were performed as described in the "cell size analysis" methods section showed that the visible decrease of *fro* response to 1 µM NaOCl was observed when using 0.1 µM cysteine, 1 µM methionine and 1 µM βME. While *fro* response was not elevated at higher concentrations of these antioxidants.

Code Availability

The custom Matlab scripts used to process and analyze the fluorescence microscopy data have been previously described [127] and are freely available from Zenodo at https://doi.org/10.5281/zenodo.3898289.

4.3 RESULTS

4.3.1 Host cells stimulate *fro* expression in *P. aeruginosa* under non-flow conditions

We investigated if the *fro* operon is activated directly by immune cells. To quantify *fro* expression, we used a *P. aeruginosa* strain that co-expresses the yellow fluorescent protein (YFP) under the transcriptional control of the *fro* promoter and mCherry under the control of a constitutive promoter (Fig. 14B). Neutrophils and macrophages are among the first immune cells that are recruited to sites of infection. We co-incubated *P. aeruginosa* with these cells for 30 minutes to determine whether they would elicit a response in the *fro* operon. Experiments were performed in the absence of flow in order to deconvolve the effects of flow from potential activation of *fro* by host cells. Relative to *P. aeruginosa* that were incubated in host cell-free media, *P. aeruginosa* in close proximity to neutrophils or that were engulfed in macrophages had higher levels of *fro* expression (Fig. 14C). Furthermore, increases in *fro* expression were observed in some *P. aeruginosa* that were internalized in fibroblasts (Fig. 14C). These data suggest direct interaction or close proximity with hosts stimulates *fro* expression in *P. aeruginosa*.

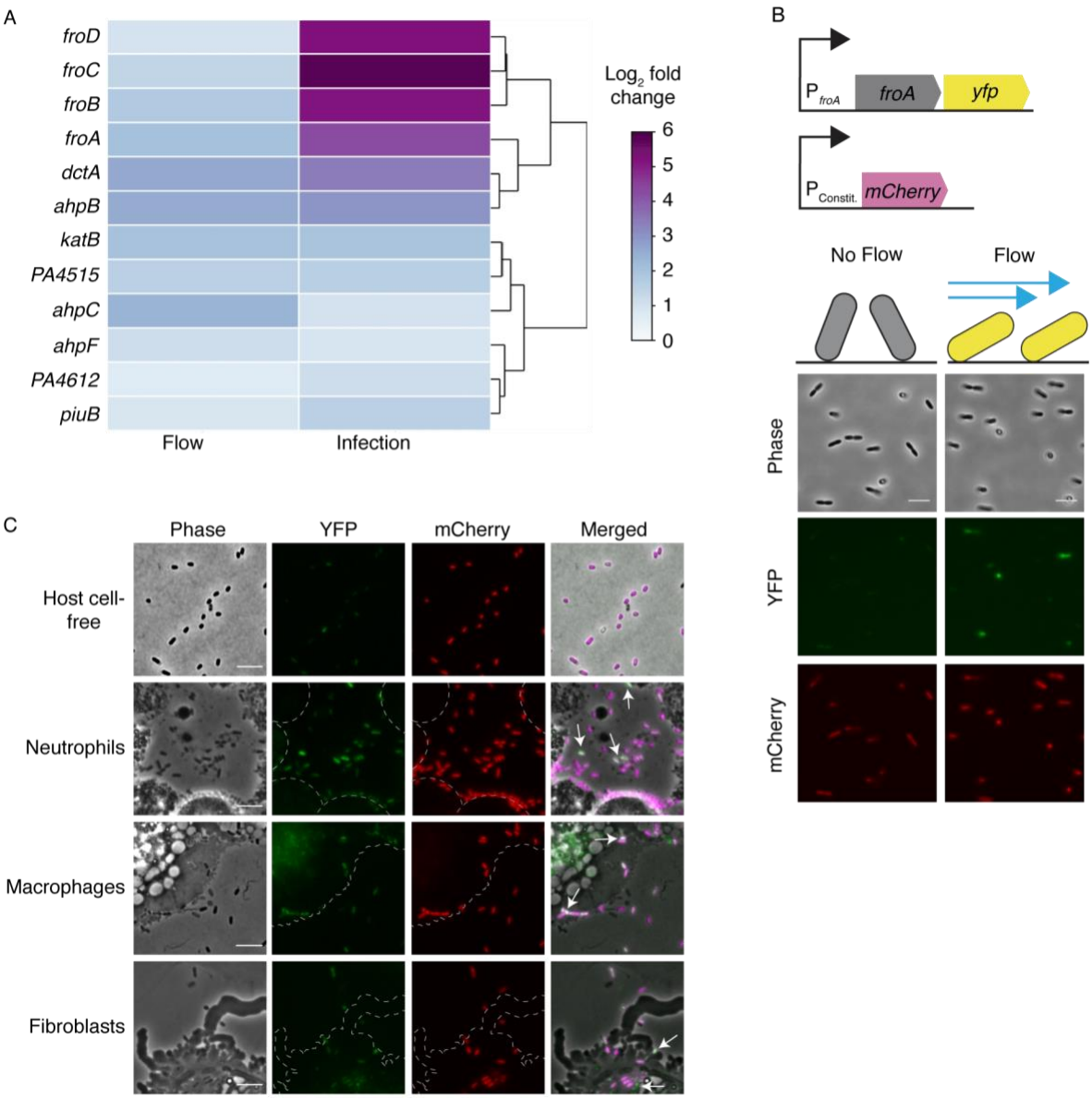

Figure 14. Activation of *fro* transcription by flow and during infection of human tissue. (A) RNA-seq heatmap of *P. aeruginosa* genes that are significantly upregulated at least 3-fold both by flow and during infections in human wounds. RNA-seq datasets are from *[113,123]*. **(B)** Top: schematic of a *P. aeruginosa* fluorescent reporter strain that contains a transcriptional fusion of *yfp* to *fro* and constitutively expresses *mCherry*. Representative phase contrast, YFP, and mCherry images the reporter under flow (right) or non-flow (left) conditions for 30 minutes. **(C)** Representative phase contrast, YFP, mCherry, and merged images of the *P. aeruginosa* reporter strain co-incubated with neutrophils, macrophages, fibroblasts, or host cell-free media for 30 minutes. Dotted lines outline the boundaries of the host cells. White arrows in merged images indicate *P. aeruginosa* with the high ratios of YFP/mCherry intensities. Images are representative of three independent repetitions. Scale bars represent 5 μm.

4.3.2 *fro* expression is induced by activated neutrophils

We focused our efforts on understanding how neutrophils activate *fro* expression, as neutrophils are one of the first immune cells that are recruited to bacterial infection sites. *P. aeruginosa* triggers respiratory bursts in neutrophils [121], which generates ROS and RCS. We hypothesized that the observed *fro* activation could be a response to respiratory burst products. To test this, we determined whether molecules released by activated neutrophils could induce *fro* expression. We isolated cell-free conditioned medium from neutrophils that were stimulated to induce respiratory bursts using 100 ng/mL phorbol myristate acetate (PMA) in neutrophil isolation medium (PBGT) [130]. *P. aeruginosa* were cultured for 3 hours in the conditioned medium (Fig. 15A). The expression of *fro* was quantified by computing the ratio of YFP to mCherry fluorescence in individual *P. aeruginosa* and averaging over at least one hundred *P. aeruginosa.* Conditioned medium from PMA-stimulated neutrophils increased the expression of *fro* by 30-fold compared to medium from unstimulated neutrophils (Fig. 15B). The upregulation in *fro* was not due to PMA, as the addition of PMA without neutrophils had no effect on *fro* expression (Fig. 15B). The conditioned media from unstimulated neutrophils had no significant effect on *fro* expression compared to PBGT medium alone (Fig. 15B).

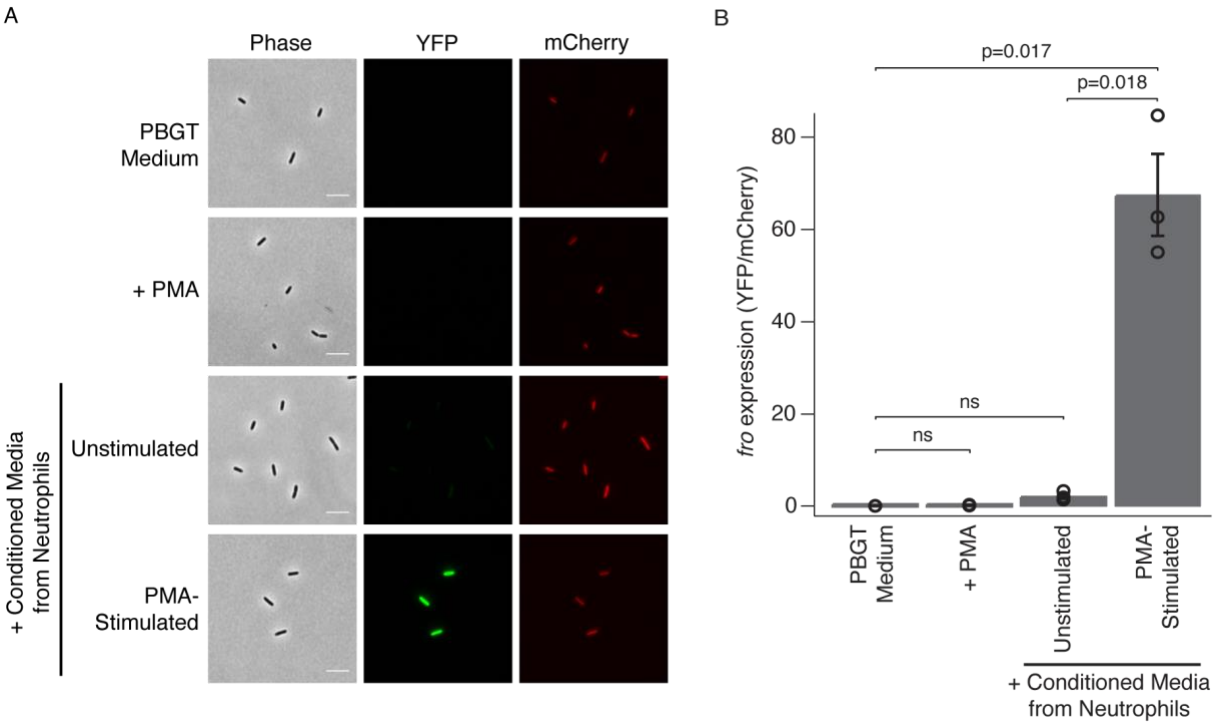

Figure 15. Conditioned medium from stimulated neutrophils induces *fro* expression. (A) Representative phase-contrast and fluorescence images and **(B)** quantification of *fro* expression levels of *P. aeruginosa* that were cultured for 3 hours in PGBT medium with or without 100 ng/mL of PMA, conditioned medium from unstimulated neutrophils, or conditioned medium from neutrophils that were stimulated with 100 ng/mL of PMA. Bars indicate the mean and error bars represent the standard error of the mean (SEM) of three independent experiments. P-values were calculated using a two-tailed, unequal variance t-test. ns indicates $p > 0.05$. Scale bars represent 5 μm.

4.3.3 *fro* expression is induced by HOCl but not by H_2O_2 or HNO_3

Previous work by Ilona Foik assessed the ability of specific respiratory burst products to drive *fro* activation. Activated neutrophils generate multiple ROS and RCS oxidants, which have an inhibitory effect on bacterial growth. We hypothesized that these oxidants induce *fro* expression and tested the impact of these species on *fro* expression at near-inhibitory concentrations (Fig. 16A). It was determined that 1 M of NaOCl or 8 μM of H_2O_2 were near the threshold of growth inhibition for *P. aeruginosa* (Fig. 16B) and were subsequently used to measured *fro* expression in cultures up to these concentration thresholds. H_2O_2 in a range of concentrations below, at, or above 8

μM had no significant impact on *fro* expression (Fig. 16C-D). In contrast, 1 μM NaOCl increased *fro* expression by up 78-fold compared to untreated cultures. This activation is not due to sodium or chloride ions alone, as neither NaCl at the same concentration or HCl up to the highest concentration without changing pH of the minimal medium did not induce *fro* expression (Fig. 16D). In addition, the *fro* response to NaOCl is not due to basic pH alone, as treatment with 6 mM NaOH, which adjusted the medium to the same pH as 1 μM NaOCl (pH 7.1), had no significant impact on *fro* activation (Fig. 16D). NaOCl-induced *fro* expression occurred at concentrations below those associated with growth inhibition (Fig. 16B-D).

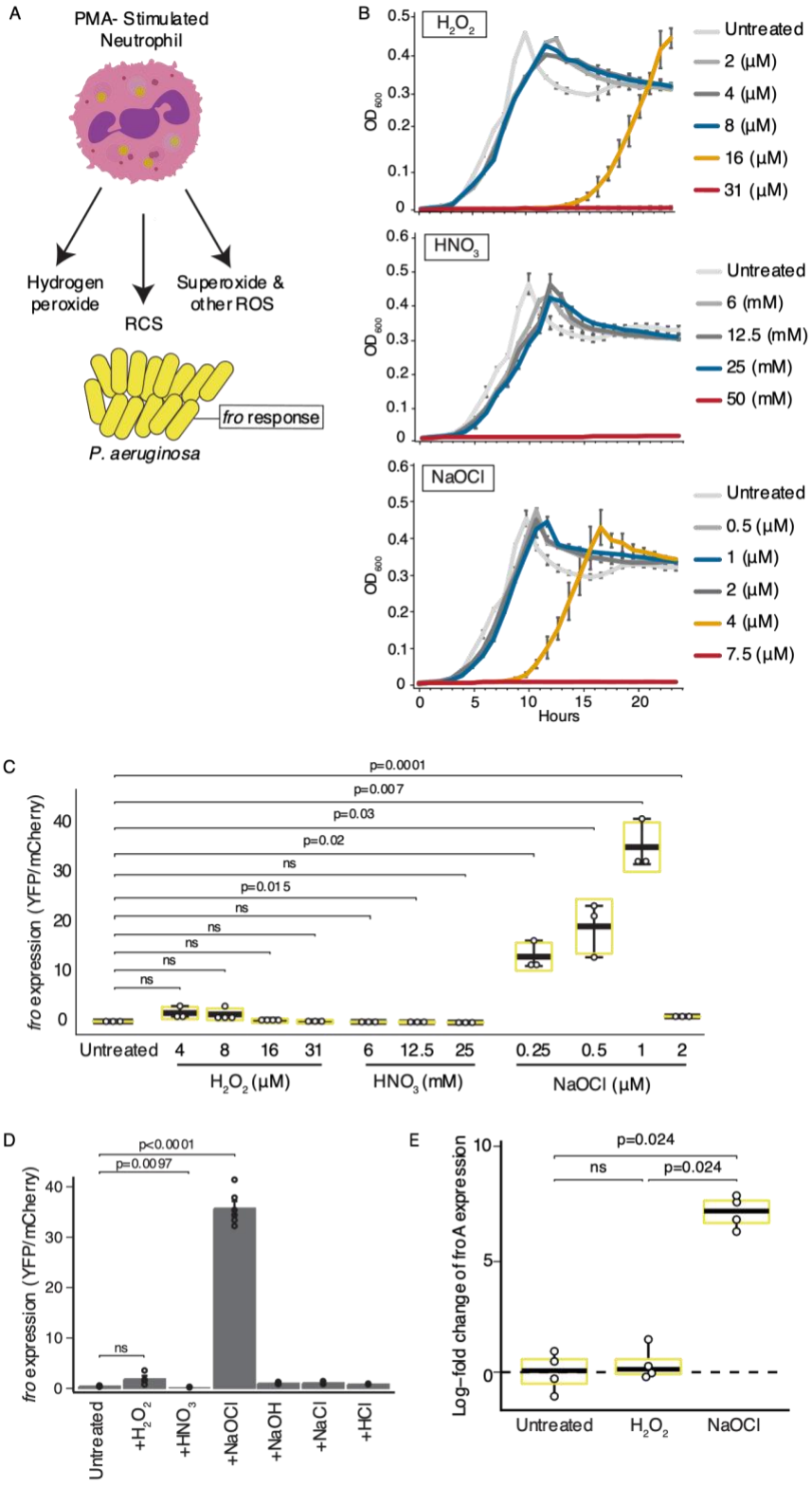

Figure 16. The expression of *fro* is induced by HOCl but not by H_2O_2 or HNO_3. (A) Schematic of model indicating that PMA-stimulated neutrophils produce respiratory burst products that could induce *fro* expression. **(B)** Growth profiles, measured by

optical density (OD_{600}), of *P. aeruginosa* that were treated with sublethal and lethal concentrations of H_2O_2, NaOCl, HNO_3, or untreated. Data points represent the mean and error bars indicate the SEM of at least two independent experiments. **(C)** The expression of *fro* in *P. aeruginosa* that were treated for 3 hours with sublethal concentrations of H_2O_2, NaOCl, HNO_3, or were untreated. **(D)** The expression of *fro* in *P. aeruginosa* that were treated for 3 hours with 8 µM H_2O_2, 1 µM NaOCl, 25 mM HNO_3, 6 mM NaOH, 1 µM NaCl, 200 µM HCl, or untreated. Bars represent the mean and error bars indicate the SEM of at least two independent experiments. Boxplots indicate the mean (black line) and interquartile range (yellow) of three independent experiments. **(E)** The *froA* expression in *P. aeruginosa* (PA14) that were treated for 0.5 hrs with 8 µM H_2O_2 and 1 µM NaOCl. Boxplots indicate the medium (black line) and interquartile range (yellow) of three independent experiments. P-values were calculated using a two-tailed, unequal variance t-test. ns indicates $p > 0.05$. Experiments were performed by Ilona Foik and Runhang Shu.

The activation of *fro* by NaOCl is consistent with a recent transcriptional study that identified *fro* as a gene that is upregulated by HOCl [131]. Interestingly, the results showed that higher concentration of 2 µM NaOCl did not increase *fro* expression. However, this concentration caused a significant decrease in cell size (Fig. 17), indicative of cell stress that may have interfered with transcription. We further assessed whether *fro* expression could be activated by the strong oxidant HNO_3. The effects of this oxidizer were measured up to inhibitory concentrations (Fig. 16B-D). However, no impact on *fro* expression was detected. These results suggest that *fro* responds specifically to RCS stress from HOCl and supports the hypothesis that HOCl produced by stimulated neutrophils activates *fro* expression.

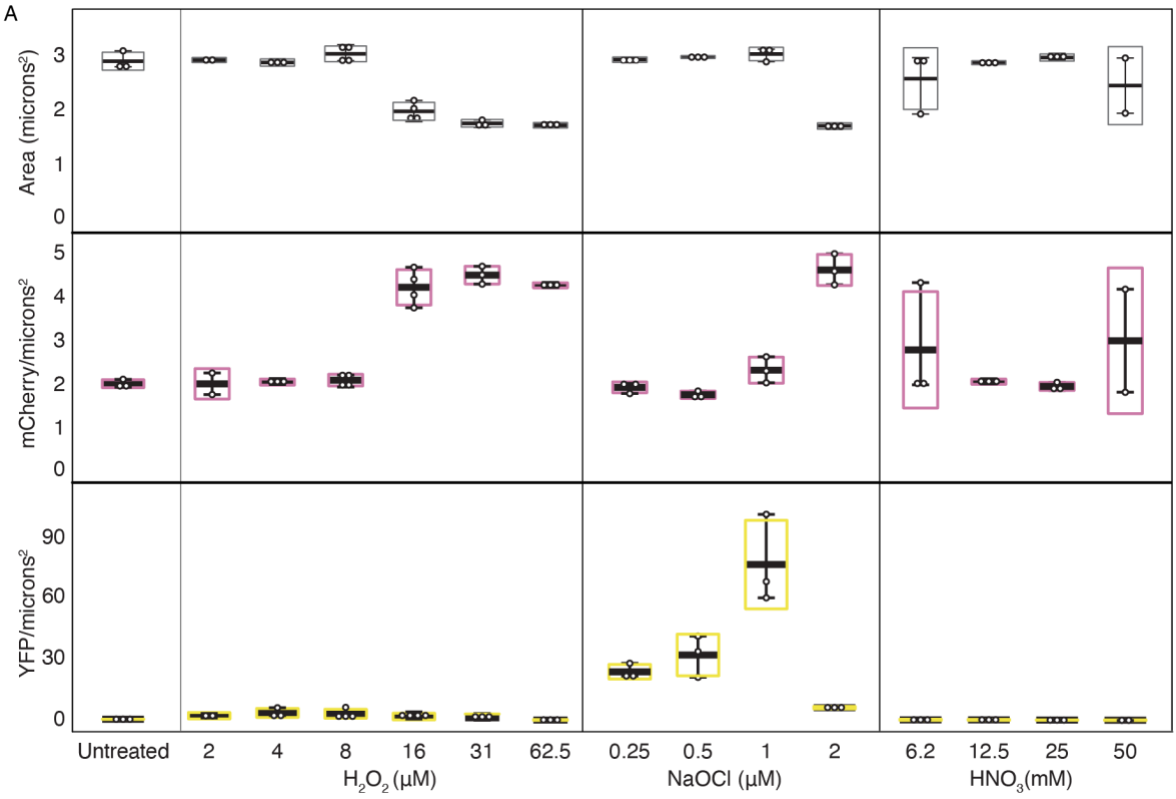

Figure 17. Effects on cell size and global transcription in *P. aeruginosa* treated with NaOCl, H_2O_2, or HNO_3. (A) Top: average area of individual *P. aeruginosa* cells, Middle: average mCherry/area, Bottom: average YFP/area in *P. aeruginosa* treated with dilutions of H2O2, NaOCl, HNO3, or untreated for 3 hours. Boxplots show the mean (black line) and the interquartile range of three independent experiments. **(B)** The *froA* expression in *P. aeruginosa* (PAO1) that were treated for 0.5 hrs with 8 μM H_2O_2 and 1 μM NaOCl. Boxplots indicate the medium (black line) and interquartile range (yellow) of three independent experiments.

4.3.4 Antioxidant supplements inhibit *fro* activation

HOCl oxidizes amine and sulfur groups within amino acids [132–135]. We posited that blocking the oxidative activity of HOCl could inhibit *fro* activation. Sulfur-containing amino acids (e.g., methionine and cysteine) and beta-mercaptoethanol (βME) are antioxidants and major targets for HOCl-mediated oxidation [135,136]. We hypothesized that supplementing 1 μM NaOCl treatments with methionine, cysteine, or βME reduces *fro* expression. Indeed, Ilona Foik observed that supplementing these antioxidants at equal or lower concentrations as NaOCl (1 μM methionine, 0.1 μM

cysteine, or 1 µM βME) significantly reduced the NaOCl-induced *fro* expression (Fig. 18A-B) indicating that the oxidative activity of NaOCl activates *fro*. Concentrations of antioxidants that were higher than 1 µM also inhibited *fro* expression (Fig. 19).

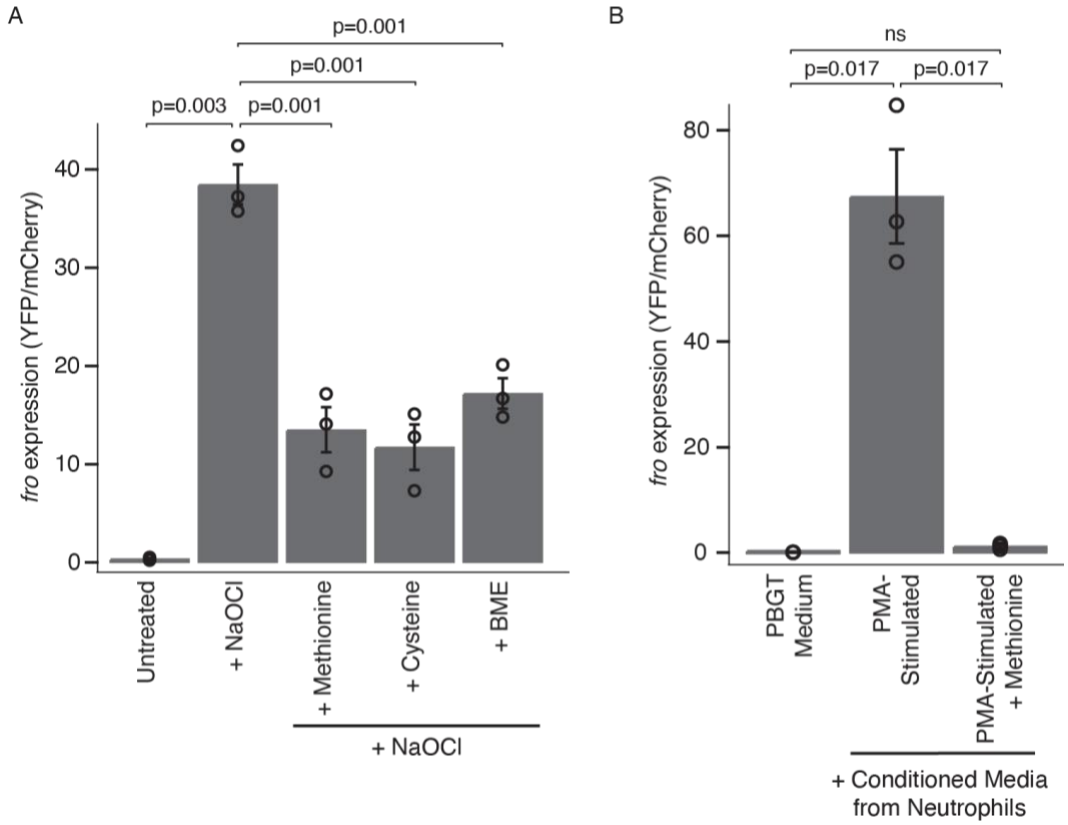

Figure 18. Antioxidants inhibit *fro* activation that is induced by HOCl and conditioned media from PMA-stimulated neutrophils. (A) The expression of *fro* in *P. aeruginosa* that are untreated, treated with 1 µM NaOCl, or treated with 1 µM NaOCl and supplemented with 1 µM methionine, 0.1 µM cysteine, or 1 µM beta-mercaptoethanol (BME), for 3 hours. **(B)** Quantification of *fro* expression levels in *P. aeruginosa* that were cultured in PBGT medium or in PBGT medium from PMA-stimulated neutrophils (replotted from Fig. 2B) that was untreated or supplemented with 100 µM methionine. Bars represent the mean and error bars indicate the SEM of three independent experiments. P-values were calculated using a two-tailed, unequal variance t-test. ns indicates $p > 0.05$. Experiments were performed by Ilona Foik.

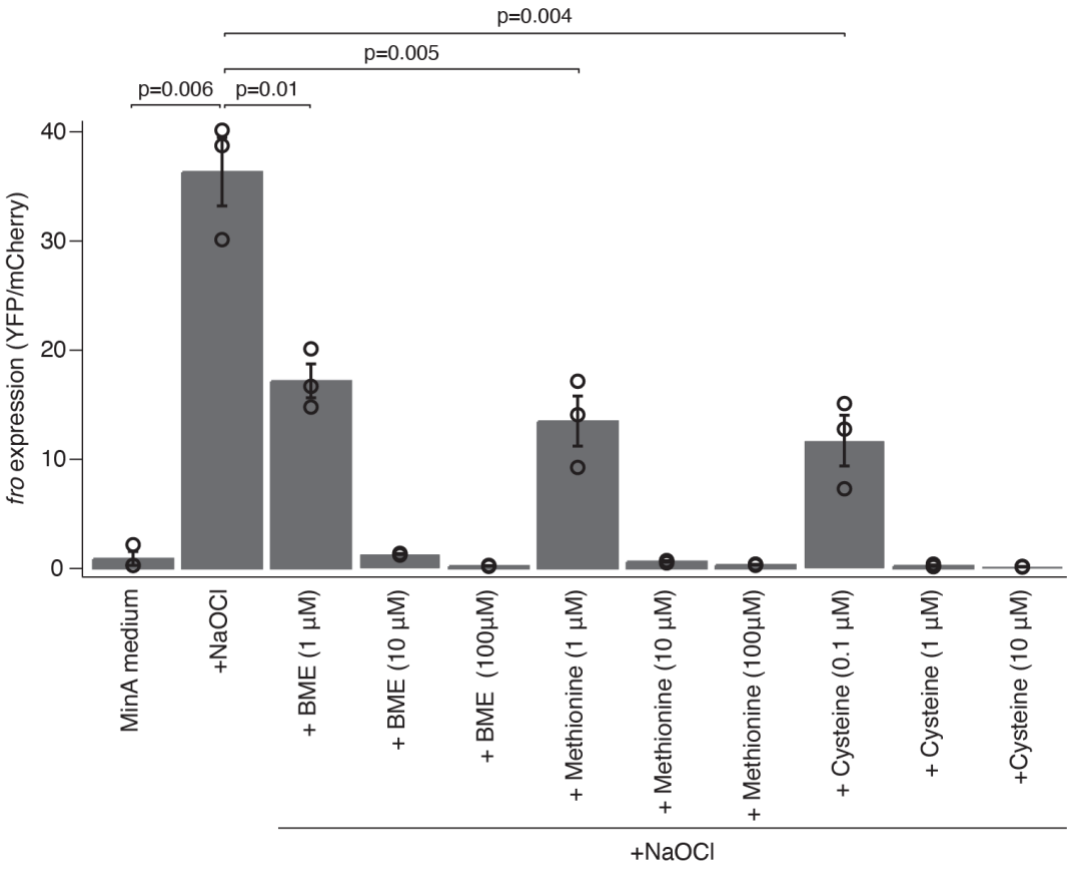

Figure 19. Dose-dependent effects of antioxidant supplements on *fro* expression induced by HOCl. Quantification of *fro* expression levels in *P. aeruginosa* cultures treated with 1 µM NaOCl and supplemented with methionine, cysteine, or beta-mercaptoethanol (BME). Plots show the mean and SEM for three independent experiments. P-values were calculated using two-tailed, unequal variance t-test. ns indicates $p > 0.05$. Experiments were performed by Ilona Foik.

Treatments of cysteine, methionine, and βME alone had no significant impact on *fro* expression (Fig. 20). Based on these data, we hypothesized that the activation of *fro* expression by PMA-stimulated neutrophils is suppressed by antioxidants. Indeed, we found that supplementing conditioned media from PMA-stimulated neutrophils with 100 µM of methionine inhibited *fro* activation (Fig. 18B) comparable to that observed in PBGT media alone and in unstimulated neutrophils (Figs. 15B and 18B). Together, these results suggest that stimulated neutrophils activate *fro* expression through the oxidative activity of HOCl.

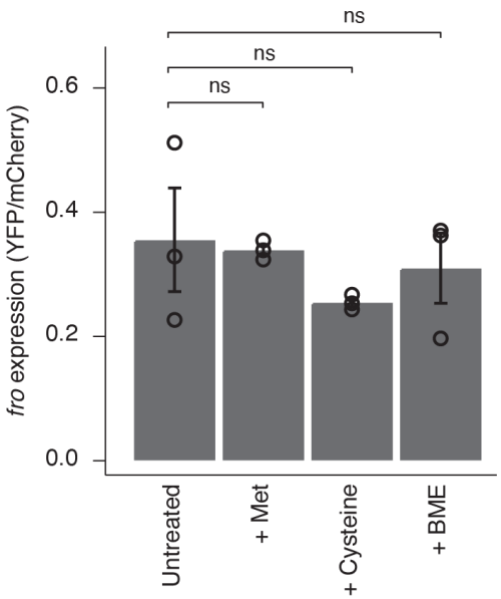

Figure 20. Effects of antioxidants alone on *fro* expression. Quantification of *fro* expression levels in *P. aeruginosa* cultures treated with 1 µM methionine, 0.1 µM cysteine, 1 µM betamercaptoethanol (BME), or untreated (MinA data replotted from Fig. 3C). Plots show the mean and the standard error of the mean (SEM) for three independent experiments. P-values were calculated using two-tailed, unequal variance t-test. ns indicates $p > 0.05$. Experiments were performed by Ilona Foik.

4.3.5 *fro* improves *P. aeruginosa* growth during HOCl treatments

We investigated whether *fro* activation has a beneficial impact on *P. aeruginosa* survival in response to HOCl-induced stress. We measured the growth of wild-type *P. aeruginosa* and the mutant strain Δ*froR*, which lacks the sigma factor that is required for *fro* activation. In the absence of NaOCl, both strains grew comparably. Treatment with 16 µM NaOCl significantly delayed the growth of the wild-type strain (Fig. 21). This treatment resulted in even greater growth inhibition in the Δ*froR* strain. This result suggests that activation of the *fro* operon increases *P. aeruginosa* survival against oxidative stress induced by HOCl.

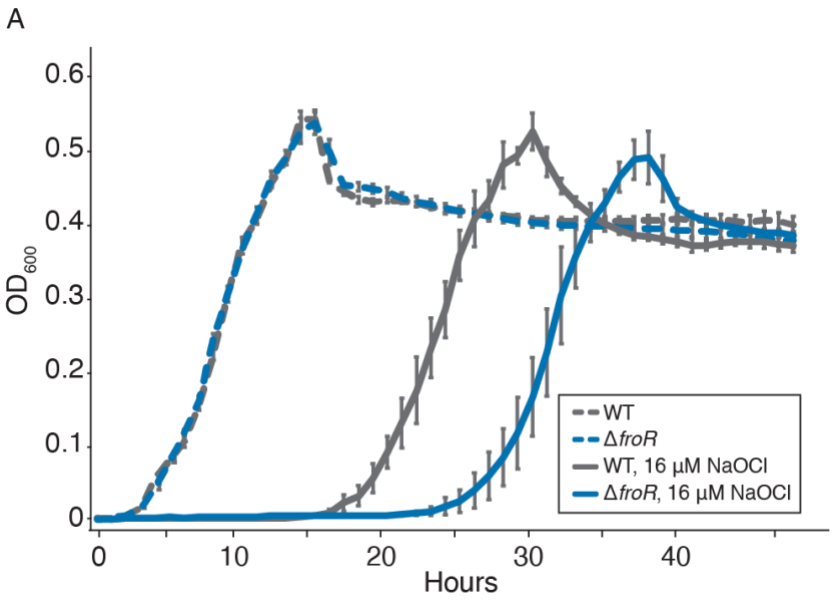

Figure 21. FroR improves *P. aeruginosa* survival against HOCl stress. Growth profiles of wild-type (WT) *P. aeruginosa* and Δ*froR* mutants that were treated with 16 µM NaOCl or untreated. Data points represent the mean and the error bars indicate the SEM of three independent experiments. Experiments performed by Andy Huang under the guidance of Lauren Urban and Ilona Foik.

4.4 Discussion

Neutrophils are activated by the presence of bacteria during the infection of host tissues. In this activated state, neutrophils produce respiratory bursts that contain high concentrations of HOCl. Whether and how bacteria respond to activated neutrophils and the RCS that the neutrophils produce has not been clear. In this study, we have demonstrated that *P. aeruginosa* responds to activated neutrophils by upregulating the transcriptional expression of the *fro* operon, which relieves HOCl-induced stress. Our data suggest that *fro* activation could function as a bacterial defense mechanism against a neutrophil attack mechanism. The *fro* response may thus improve *P. aeruginosa* survival against neutrophils and enhance the colonization of human tissues during infection.

One of the striking features of the *fro* system is that it is finely tuned to activate at sub-lethal concentrations (1-2 µM) of NaOCl. Activated neutrophils produce HOCl as high as 50 µM HOCl [129]. The activation of *fro* at relatively low concentrations suggests that the system functions as a sensitive early detector of HOCl. In host environments, *fro* may activate in environments where HOCl is present at low concentrations, such as during early stages of neutrophil stimulation or when *P. aeruginosa* is spatially distant from activated neutrophils. The early activation of *fro* could benefit *P. aeruginosa* by triggering a protective mechanism that relieves the impact of HOCl stress before HOCl reaches lethal concentrations. This mechanism would ensure that the system is already activated when *P. aeruginosa* encounters neutrophils. Indeed, we observed that *fro* expression is strongly upregulated in *P. aeruginosa* that are in close proximity to activated neutrophils (Fig. 14C). Additional evidence supports the function of *fro* as a defensive early detection mechanism. The transcription of *fro* is partially activated by moving fluids *[113]* that generate wall shear stresses in animal circulatory systems. Neutrophils move in the fluidic networks of the circulatory system in response to tissue injury. *P. aeruginosa* that are present in the circulatory system could prime its defenses via flowing sensing by *fro* against potential HOCl produced by recruited neutrophils.

How does *fro* relieve HOCl stress in bacteria? The *fro* operon activates over 100 genes, including *ahpC*, *ahpF*, and *katB,* that encode proteins that reduce the activity of ROS and are critical for bacterial survival against oxidative stress [137,138]. While the effect of these antioxidant proteins on RCS activity is unclear, our data suggest that *fro* activation mitigates the toxic effects of HOCl (Fig. 21). In addition, our results indicate

that the presence of antioxidant agents, including methionine, cysteine, or BME, reduces the activity of HOCl (Figs. 18 and 19). Together, our data suggest a model in which *P. aeruginosa* senses HOCl via the *fro* system, which upregulates the production of antioxidant proteins that suppress the toxic effects of HOCl. This would constitute an early detection mechanism that defends against neutrophils. A recent finding identified the RclR transcriptional regulator as a sensor of HOCl [139]. Further work is necessary to determine how antioxidative proteins and antioxidative agents reduce the toxic activity of HOCl and the extent that RclR and *fro* are co-regulated by HOCl.

In addition to promoting colonization of the lung and gastrointestinal tract [122,140], the *fro* system may have additional impacts on pathogenicity, such as increasing antibiotic resistance. Bacteria that are exposed to low doses of HOCl have higher rates of horizontal gene transfer and can acquire antibiotic resistance genes more rapidly [141,142]. The tolerance of *P. aeruginosa* to HOCl via *fro* may thus provide a mechanism to facilitate antibiotic resistance. The findings here thus suggest that the *fro* pathway could be an important defense mechanism to target. Inhibition of this pathway could increase *P. aeruginosa* susceptibility to neutrophil-mediated killing while minimizing antibiotic resistance.

Chapter 5

Future Directions

5.1 Epigenetics mechanism involved in wound healing and tissue regeneration

Our results provide novel information about the immune responses involved in tissue regeneration. Immune activation is necessary for wound healing and tissue regeneration, while chronic inflammation can cause fibrosis, tissue damage, and implant failure [143]. We found that hypomethylation of CpGs occurs within genes involved in immune activation and that HypoDMCs were enriched for binding motifs that were associated with TFs commonly found in macrophages such as C/EBP, IRF family members, and PU.1 [144]. Previous research found that the ETS TF member PU.1 has a direct role in H3K4me1 deposition and that TLR4 activation in macrophages is also linked with H3K4 methylation [145,146]. A better understanding of epigenetic mechanisms that contribute to wound healing processes can help improve the design of novel regenerative therapies to promote tissue regeneration and suppress pro-inflammatory responses that can have potentially deleterious effects. The urgency of this research has increased since findings have showed that the healthy maintenance of immune responses becomes dysfunctional with aging [147]. Epidemiological reports indicate that over 75% of the elderly population has at least one health condition, which often presents with chronic inflammation [49]. The effects of immune dysfunction associated with aging or pre-existing medical conditions on tissue regeneration following surgical repair with SF grafts requires further research [148,149].

Previous studies have demonstrated that targeting epigenetic modifiers involved in reprogramming macrophages can influence wound healing M2 phenotypes and also successfully improve tissue regeneration following surgical implantation [27,150,151]. Epigenetic modifiers such as DNMT3A and Tet Methylcytosine Dioxygenase 2 (TET2) are involved in the reprogramming of macrophages during inflammation [152]. The Downing lab and others found that physical properties, such as implant stiffness, can also influence macrophage fate decisions and inflammatory gene activity [29,30]. Previous studies showed stiffer substrates can polarize macrophages to the pro-inflammatory M1 phenotype and upregulate TNF-α and IL-1β expression [153]. Additionally, stiffer implants were associated with more severe and prolonged foreign body FBR *in vivo* [154,155]. Others have found that stiffer substrates prime vascular smooth muscle cell (vSMC) towards a proinflammatory phenotype which increases the secretion of inflammatory cytokines, such as MCP1 and IL6 that recruit monocyte and M1 macrophages and result in arterial stiffening. New findings suggest this biomechanism-immune modulating mechanism may be mediated by the phosphorylation and endocytosis of a receptor tyrosine kinase that binds collagens known as discoidin domain receptor 1 (DDR1) which represses the expression of DNA methyltransferase 1 (DNMT1) [156]. Future work should further investigate novel approaches to target epigenetic modifiers to modulate immune responses and tissue regeneration following surgical repair with SF grafts, especially in vulnerable patient populations which have impaired immune systems [148,149].

A limitation of our analysis is that it is based on bulk DNAme profiles. Several studies showed that epigenetic signatures are highly tissue- and cell-type-specific [157].

Our findings may reflect the presence infiltrating immune cells based on previous work that found neutrophils and monocytes are rapidly recruited to the surgical wound site following SF implantation [22]. Future work is required to distinguish epigenetic and expression changes in the different cell populations found at the implant site such as the regenerating esophageal epithelial and immune cells during regeneration [108,109]. Several *in silico* deconvolution methods have been developed to infer cell-type fractions and epigenetic signatures from bulk methylation data. There are two main types of deconvolution methods: reference-based and reference-free. Reference-based methods are the preferred method since several studies have found they outperform reference-free methods [158]. Reference-based deconvolution methods such as MethylCIBERSORT and MethylResolver are supervised algorithms that infer the relative cell fractions from bulk tissue methylation using reference methylation signatures to identify cell-type specific differentially methylated regions (DMRs) [159,160]. Reference-free methods such as RefFreeEWAS2.0 by Houseman *et al*. are unsupervised models that estimate the number of cell types from the proportion of variation in the bulk methylation profiles to resolve cell-fraction methylation signatures [161]. Unfortunately, cell-type RRBS methylation data does not exist currently in the rat genome. Future work should investigate whether reference methylation data in the human or mouse genome could be lifted over into the rat genome to use in deconvolution methylation analysis. The results of this work can determine key molecular and epigenetics mechanisms involved in wound healing processes during tissue regeneration.

5.2 How does *fro* activation impact bacterial pathogenicity?

We found that *fro* induction occurs at sublethal doses of NaOCl which are below levels associated with bactericidal activity or levels produced during neutrophil activation *in vitro* [129]. Our results suggest that *fro* activation primes *P. aeruginosa* defenses against neutrophil activation to upregulate the expression of antioxidants. Other work found that the *fro* operon protects against HOCl stress in *P. aeruginosa* (PA14) [162]. However, our understanding of how environmental conditions in the human body, such as flow and the presence of immune cells, impact bacterial fitness and virulence during infections remains limited. Future work is required to determine the biological significance of *fro* activation by HOCl *in vivo*. To this end, ongoing work in the labs of Drs. Siryaporn and Pearlman are assessing *fro* activation using a corneal wound assay in mice with a myeloperoxidase inhibitor which inhibits oxidative burst in neutrophils, to determine whether *fro* expression is dependent on oxidative burst. The results of this work can help determine whether targeting the *fro* signaling pathway can increase susceptibility to HOCl stress during *P. aeruginosa* infections.

Future work should focus on determining how HOCl activates the *fro* system. It is possible that oxidation by HOCl activates the sigma factor FroR or inactivates the anti-sigma factor FroI which could increase *fro* expression. Previous studies have identified several ROS defense sensors in bacteria such as the transcriptional regulators OxyR or SoxR in *Escherichia coli* and MexT, a transcriptional regulator which activates expression of the MexEF-OprN multidrug efflux system in *P. aeruginosa* [163,164]. Unfortunately, little information is known about bacterial defense mechanisms against HOCl stress. Future work is needed to compare changes in gene expression in WT

PA14 treated with HOCl, H_2O_2, or nitric oxide with qRT-PCR and RNA-seq. The results of this work can help identify novel bacterial defense mechanisms that protect against HOCl stress specifically.

REFERENCES

1. Waterland, R.A. (2006) Epigenetic mechanisms and gastrointestinal development. *J Pediatr* 149, S137-142
2. Bibikova, M. *et al.* (2006) Human embryonic stem cells have a unique epigenetic signature. *Genome Res* 16, 1075–1083
3. Ladle, B.H. *et al.* (2016) De novo DNA methylation by DNA methyltransferase 3a controls early effector CD8+ T-cell fate decisions following activation. *Proc Natl Acad Sci U S A* 113, 10631–10636
4. Choi, J. *et al.* (2010) In vivo administration of hypomethylating agents mitigate graft-versus-host disease without sacrificing graft-versus-leukemia. *Blood* 116, 129–139
5. Cooper, M.L. *et al.* (2017) Azacitidine Mitigates Graft-versus-Host Disease via Differential Effects on the Proliferation of T Effectors and Natural Regulatory T Cells In Vivo. *J Immunol* 198, 3746–3754
6. Ktena, Y.P. *et al.* (2022) Donor T cell DNMT3a regulates alloreactivity in mouse models of hematopoietic stem cell transplantation. *J Clin Invest* 132, e158047
7. Lamb, P.J. and Griffin, S.M. (2005) The Anatomy and Physiology of the Oesophagus. In *Upper Gastrointestinal Surgery*, pp. 1–15, Springer-Verlag
8. Doupé, D.P. *et al.* (2012) A single progenitor population switches behavior to maintain and repair esophageal epithelium. *Science* 337, 1091–1093
9. Raboei, E. and Luoma, R. (2008) Colon Patch Esophagoplasty: An Alternative to Total Esophagus Replacement? *Eur J Pediatr Surg* 18, 230–232
10. Benazzo, M. *et al.* (2008) Sternocleidomastoid Muscle Flap in Esophageal Perforation Repair After Cervical Spine Surgery: Concepts, Techniques, and Personal Experience. *Journal of Spinal Disorders & Techniques* 21, 597–605
11. Ki, S.H. *et al.* (2015) Reconstructive Trends in Post-Ablation Patients with Esophagus and Hypopharynx Defect. *Arch Craniofac Surg* 16, 105
12. Lin, Y.-C. *et al.* (2017) Patch esophagoplasty with a free proximal lateral leg flap for focal stricture of the cervical esophagus: A case report: Patch Esophagoplasty with Proximal Lateral Leg Flap. *Microsurgery* 37, 426–430
13. Strisciuglio, C. *et al.* (2021) Disease-associated DNA methylation signatures in esophageal biopsies of children diagnosed with Eosinophilic Esophagitis. *Clin Epigenetics* 13, 81
14. Kaz, A.M. *et al.* (2011) DNA methylation profiling in Barrett's esophagus and esophageal adenocarcinoma reveals unique methylation signatures and molecular subclasses. *Epigenetics* 6, 1403–1412
15. Wang, W. *et al.* (2013) PIK3CA hypomethylation plays a key role in activation of the PI3K/AKT pathway in esophageal cancer in Chinese patients. *Acta Pharmacol Sin* 34, 1560–1567
16. Jammula, S. *et al.* (2020) Identification of Subtypes of Barrett's Esophagus and Esophageal Adenocarcinoma Based on DNA Methylation Profiles and Integration of Transcriptome and Genome Data. *Gastroenterology* 158, 1682-1697.e1
17. Chen, Y. *et al.* (2020) PI3K/Akt signaling pathway is essential for de novo hair follicle regeneration. *Stem Cell Res Ther* 11, 144
18. Chmielowiec, J. *et al.* (2007) c-Met is essential for wound healing in the skin. *Journal of Cell Biology* 177, 151–162

19. Zheng, M.-G. *et al.* (2019) TrkA regulates the regenerative capacity of bone marrow stromal stem cells in nerve grafts. *Neural Regen Res* 14, 1765
20. Huang, B. *et al.* (1998) [A new burn wound covering-fibroin membrane]. *Zhonghua Zheng Xing Shao Shang Wai Ke Za Zhi* 14, 270–274
21. Wang, Y. *et al.* (2008) In vivo degradation of three-dimensional silk fibroin scaffolds. *Biomaterials* 29, 3415–3428
22. Gundogdu, G. *et al.* (2021) Molecular mechanisms of esophageal epithelial regeneration following repair of surgical defects with acellular silk fibroin grafts. *Sci Rep* 11, 7086
23. Gundogdu, G. *et al.* (2021) Evaluation of Bilayer Silk Fibroin Grafts for Tubular Esophagoplasty in a Porcine Defect Model. *Tissue Eng Part A* 27, 103–116
24. Filipe, E.C. *et al.* (2018) Rapid Endothelialization of Off-the-Shelf Small Diameter Silk Vascular Grafts. *JACC Basic Transl Sci* 3, 38–53
25. Park, Y.R. *et al.* (2018) NF-κB signaling is key in the wound healing processes of silk fibroin. *Acta Biomater* 67, 183–195
26. Lavoie, E.G. *et al.* (2011) Innate immune responses to Pseudomonas aeruginosa infection. *Microbes Infect* 13, 1133–1145
27. Smith, T.D. *et al.* (2017) Harnessing macrophage plasticity for tissue regeneration. *Adv Drug Deliv Rev* 114, 193–205
28. Leoni, G. *et al.* (2015) Wound repair: role of immune-epithelial interactions. *Mucosal Immunol* 8, 959–968
29. Sridharan, R. *et al.* (2019) Material stiffness influences the polarization state, function and migration mode of macrophages. *Acta Biomater* 89, 47–59
30. McWhorter, F.Y. *et al.* (2013) Modulation of macrophage phenotype by cell shape. *Proc. Natl. Acad. Sci. U.S.A.* 110, 17253–17258
31. DeFife, K.M. *et al.* (1999) Spatial regulation and surface chemistry control of monocyte/macrophage adhesion and foreign body giant cell formation by photochemically micropatterned surfaces. *J Biomed Mater Res* 45, 148–154
32. Dewair, M. *et al.* (1985) Use of immunoblot technique for detection of human IgE and IgG antibodies to individual silk proteins. *J Allergy Clin Immunol* 76, 537–542
33. Altman, G.H. *et al.* (2003) Silk-based biomaterials. *Biomaterials* 24, 401–416
34. Linton, M.F. *et al.* (2019) Akt Signaling in Macrophage Polarization, Survival, and Atherosclerosis. *Int J Mol Sci* 20, 2703
35. Zhao, H.-Y. *et al.* (2021) M2 macrophages, but not M1 macrophages, support megakaryopoiesis by upregulating PI3K-AKT pathway activity. *Signal Transduct Target Ther* 6, 234
36. Arranz, A. *et al.* (2012) Akt1 and Akt2 protein kinases differentially contribute to macrophage polarization. *Proc Natl Acad Sci U S A* 109, 9517–9522
37. Davenport Huyer, L. *et al.* (2020) Advanced Strategies for Modulation of the Material–Macrophage Interface. *Adv. Funct. Mater.* 30, 1909331
38. Dadi, N.C.T. *et al.* (2021) Impact of Healthcare-Associated Infections Connected to Medical Devices-An Update. *Microorganisms* 9, 2332
39. Cassini, A. *et al.* (2016) Burden of Six Healthcare-Associated Infections on European Population Health: Estimating Incidence-Based Disability-Adjusted Life Years through a Population Prevalence-Based Modelling Study. *PLoS Med* 13, e1002150

40. Rosenthal, V.D. *et al.* (2022) Risk factors for mortality in ICU patients in 10 middle eastern countries: The role of healthcare-associated infections. *J Crit Care* 72, 154149
41. Rosenthal, V.D. *et al.* (2022) The impact of healthcare-associated infections on mortality in ICU: A prospective study in Asia, Africa, Eastern Europe, Latin America, and the Middle East. *Am J Infect Control* DOI: 10.1016/j.ajic.2022.08.024
42. Aprahamian, T. *et al.* (2008) Ageing is associated with diminished apoptotic cell clearance in vivo. *Clin Exp Immunol* 152, 448–455
43. Simon, M. *et al.* (2019) LINE1 Derepression in Aged Wild-Type and SIRT6-Deficient Mice Drives Inflammation. *Cell Metab* 29, 871-885.e5
44. Franceschi, C. *et al.* (2017) Inflammaging and 'Garb-aging.' *Trends in Endocrinology & Metabolism* 28, 199–212
45. West, A.P. *et al.* (2015) Mitochondrial DNA stress primes the antiviral innate immune response. *Nature* 520, 553–557
46. Liu, L. *et al.* (2014) HMGB1-DNA complex-induced autophagy limits AIM2 inflammasome activation through RAGE. *Biochem Biophys Res Commun* 450, 851–856
47. Liu, B. *et al.* (2016) CpG methylation patterns of human mitochondrial DNA. *Sci Rep* 6, 23421
48. Matzinger, P. (2007) Friendly and dangerous signals: is the tissue in control? *Nat Immunol* 8, 11–13
49. Heyn, H. *et al.* (2012) Distinct DNA methylomes of newborns and centenarians. *Proc Natl Acad Sci U S A* 109, 10522–10527
50. Johansson, A. *et al.* (2013) Continuous Aging of the Human DNA Methylome Throughout the Human Lifespan. *PLoS One* 8, e67378
51. De Cecco, M. *et al.* (2019) L1 drives IFN in senescent cells and promotes age-associated inflammation. *Nature* 566, 73–78
52. Hemmi, H. *et al.* (2000) A Toll-like receptor recognizes bacterial DNA. *Nature* 408, 740–745
53. Notley, C.A. *et al.* (2017) DNA methylation governs the dynamic regulation of inflammation by apoptotic cells during efferocytosis. *Sci Rep* 7, 42204
54. Agrawal, A. *et al.* (2010) Age-associated epigenetic modifications in human DNA increase its immunogenicity. *Aging* 2, 93–100
55. Benayoun, B.A. *et al.* (2019) Remodeling of epigenome and transcriptome landscapes with aging in mice reveals widespread induction of inflammatory responses. *Genome Res* 29, 697–709
56. Keating, S.E. *et al.* (2011) Cytosolic DNA sensors regulating type I interferon induction. *Trends Immunol.* 32, 574–581
57. Kim, T. *et al.* (2010) Aspartate-glutamate-alanine-histidine box motif (DEAH)/RNA helicase A helicases sense microbial DNA in human plasmacytoid dendritic cells. *Proc. Natl. Acad. Sci. U.S.A.* 107, 15181–15186
58. Gasser, S. *et al.* (2017) Sensing of dangerous DNA. *Mech. Ageing Dev.* 165, 33–46
59. Meunier, E. *et al.* (2015) Guanylate-binding proteins promote activation of the AIM2 inflammasome during infection with Francisella novicida. *Nat. Immunol.* 16, 476–484

60. Maegawa, S. *et al.* (2017) Caloric restriction delays age-related methylation drift. *Nat Commun* 8, 539
61. Ma, Z. *et al.* (2018) Epigenetic drift of H3K27me3 in aging links glycolysis to healthy longevity in Drosophila. *Elife* 7
62. Simonsen, A. *et al.* (2008) Promoting basal levels of autophagy in the nervous system enhances longevity and oxidant resistance in adult Drosophila. *Autophagy* 4, 176–184
63. Genden, E.M. and Jacobson, A.S. (2005) The role of the anterolateral thigh flap for pharyngoesophageal reconstruction. *Arch Otolaryngol Head Neck Surg* 131, 796–799
64. Maghsoudlou, P. *et al.* (2014) Tissue engineering of the esophagus. *Semin Pediatr Surg* 23, 127–134
65. Algarrahi, K. *et al.* (2015) Acellular bi-layer silk fibroin scaffolds support functional tissue regeneration in a rat model of onlay esophagoplasty. *Biomaterials* 53, 149–159
66. Gundogdu, G. *et al.* (2021) Molecular mechanisms of esophageal epithelial regeneration following repair of surgical defects with acellular silk fibroin grafts. *Sci Rep* 11, 7086
67. Moore, L.D. *et al.* (2013) DNA Methylation and Its Basic Function. *Neuropsychopharmacol* 38, 23–38
68. Ogunwobi, O.O. *et al.* (2013) Epigenetic upregulation of HGF and c-Met drives metastasis in hepatocellular carcinoma. *PLoS One* 8, e63765
69. Jin, W. *et al.* (2011) DNA methylation-dependent regulation of TrkA, TrkB, and TrkC genes in human hepatocellular carcinoma. *Biochem Biophys Res Commun* 406, 89–95
70. Krueger, F. and Andrews, S.R. (2011) Bismark: a flexible aligner and methylation caller for Bisulfite-Seq applications. *Bioinformatics* 27, 1571–1572
71. Akalin, A. *et al.* (2012) methylKit: a comprehensive R package for the analysis of genome-wide DNA methylation profiles. *Genome Biol* 13, R87
72. Gibbs, R.A. *et al.* (2004) Genome sequence of the Brown Norway rat yields insights into mammalian evolution. *Nature* 428, 493–521
73. Havlak, P. *et al.* (2004) The Atlas genome assembly system. *Genome Res* 14, 721–732
74. Kanehisa, M. and Goto, S. (2000) KEGG: kyoto encyclopedia of genes and genomes. *Nucleic Acids Res* 28, 27–30
75. Mi, H. *et al.* (2013) Large-scale gene function analysis with the PANTHER classification system. *Nat Protoc* 8, 1551–1566
76. Ge, S.X. *et al.* (2020) ShinyGO: a graphical gene-set enrichment tool for animals and plants. *Bioinformatics* 36, 2628–2629
77. Ashburner, M. *et al.* (2000) Gene Ontology: tool for the unification of biology. *Nat Genet* 25, 25–29
78. Benjamini, Y. and Hochberg, Y. (1995) Controlling the False Discovery Rate: A Practical and Powerful Approach to Multiple Testing. *Journal of the Royal Statistical Society. Series B (Methodological)* 57, 289–300

79. Heinz, S. *et al.* (2010) Simple combinations of lineage-determining transcription factors prime cis-regulatory elements required for macrophage and B cell identities. *Mol Cell* 38, 576–589
80. Gao, T. and Qian, J. (2019) EnhancerAtlas 2.0: an updated resource with enhancer annotation in 586 tissue/cell types across nine species. *Nucleic Acids Research* DOI: 10.1093/nar/gkz980
81. Boison, D. *et al.* (2022) The impact of methodology on the reproducibility and rigor of DNA methylation data. *Sci Rep* 12, 380
82. Zhu, M. *et al.* (2019) In vivo engineered extracellular matrix scaffolds with instructive niches for oriented tissue regeneration. *Nat Commun* 10, 4620
83. Ryckman, C. *et al.* (2003) Proinflammatory activities of S100: proteins S100A8, S100A9, and S100A8/A9 induce neutrophil chemotaxis and adhesion. *J Immunol* 170, 3233–3242
84. Pervushina, O. *et al.* (2004) Platelet factor 4/CXCL4 induces phagocytosis and the generation of reactive oxygen metabolites in mononuclear phagocytes independently of Gi protein activation or intracellular calcium transients. *J Immunol* 173, 2060–2067
85. Maurer, A.-M. *et al.* (2006) Roles of platelet factor 4 in hematopoiesis and angiogenesis. *Growth Factors* 24, 242–252
86. Wu, X. *et al.* (2006) Genomic organization, localization and polymorphism of porcine PSMB10, a gene encoding the third beta-type proteasome subunit of 26S proteasome complex. *J Anim Breed Genet* 123, 331–336
87. Gross, S.M. and Rotwein, P. (2016) Mapping growth-factor-modulated Akt signaling dynamics. *J Cell Sci* 129, 2052–2063
88. Wang, D. *et al.* (1999) Induction of vascular endothelial growth factor expression in endothelial cells by platelet-derived growth factor through the activation of phosphatidylinositol 3-kinase. *Cancer Res* 59, 1464–1472
89. Ross, R. *et al.* (1985) Platelet-derived growth factor: its potential roles in wound healing, atherosclerosis, neoplasia, and growth and development. *Ciba Found Symp* 116, 98–112
90. Martin, J.F. *et al.* (1992) Repression of myogenin function by TGF-beta 1 is targeted at the basic helix-loop-helix motif and is independent of E2A products. *J Biol Chem* 267, 10956–10960
91. Hu, J.S. *et al.* (1992) HEB, a helix-loop-helix protein related to E2A and ITF2 that can modulate the DNA-binding ability of myogenic regulatory factors. *Mol Cell Biol* 12, 1031–1042
92. Mendizabal, I. *et al.* (2017) Body-hypomethylated human genes harbor extensive intragenic transcriptional activity and are prone to cancer-associated dysregulation. *Nucleic Acids Res* 45, 4390–4400
93. Yang, X. *et al.* (2014) Gene body methylation can alter gene expression and is a therapeutic target in cancer. *Cancer Cell* 26, 577–590
94. Okano, M. *et al.* (1999) DNA methyltransferases Dnmt3a and Dnmt3b are essential for de novo methylation and mammalian development. *Cell* 99, 247–257
95. Marecki, S. *et al.* (2001) PU.1 and multiple IFN regulatory factor proteins synergize to mediate transcriptional activation of the human IL-1 beta gene. *J Immunol* 166, 6829–6838

96. Yamada, T. *et al.* (2009) Transcription factor ELF4 controls the proliferation and homing of CD8+ T cells via the Krüppel-like factors KLF4 and KLF2. *Nat Immunol* 10, 618–626
97. Edwards, H. *et al.* (2009) RUNX1 regulates phosphoinositide 3-kinase/AKT pathway: role in chemotherapy sensitivity in acute megakaryocytic leukemia. *Blood* 114, 2744–2752
98. Fujita, T. *et al.* (2004) Runx2 induces osteoblast and chondrocyte differentiation and enhances their migration by coupling with PI3K-Akt signaling. *J Cell Biol* 166, 85–95
99. Baatar, D. *et al.* (2002) Esophageal ulceration triggers expression of hypoxia-inducible factor-1 alpha and activates vascular endothelial growth factor gene: implications for angiogenesis and ulcer healing. *Am J Pathol* 161, 1449–1457
100. Murrell, A. *et al.* (2001) An intragenic methylated region in the imprinted Igf2 gene augments transcription. *EMBO Rep* 2, 1101–1106
101. Tarnawski, A.S. and Ahluwalia, A. (2012) Molecular mechanisms of epithelial regeneration and neovascularization during healing of gastric and esophageal ulcers. *Curr Med Chem* 19, 16–27
102. Fang, X. *et al.* (1999) Regulation of BAD phosphorylation at serine 112 by the Ras-mitogen-activated protein kinase pathway. *Oncogene* 18, 6635–6640
103. Chung, J. *et al.* (1994) PDGF- and insulin-dependent pp70S6k activation mediated by phosphatidylinositol-3-OH kinase. *Nature* 370, 71–75
104. Luo, X. *et al.* (2021) Effects of DNA Methylation on TFs in Human Embryonic Stem Cells. *Front Genet* 12, 639461
105. Medvedeva, Y.A. *et al.* (2014) Effects of cytosine methylation on transcription factor binding sites. *BMC Genomics* 15, 119
106. Yano, S. *et al.* (1998) Calcium promotes cell survival through CaM-K kinase activation of the protein-kinase-B pathway. *Nature* 396, 584–587
107. Tullai, J.W. *et al.* (2004) Identification of Transcription Factor Binding Sites Upstream of Human Genes Regulated by the Phosphatidylinositol 3-Kinase and MEK/ERK Signaling Pathways. *Journal of Biological Chemistry* 279, 20167–20177
108. Schmidt, M. *et al.* (2020) Deconvolution of cellular subsets in human tissue based on targeted DNA methylation analysis at individual CpG sites. *BMC Biol* 18, 178
109. Stueve, T.R. *et al.* (2016) The importance of detailed epigenomic profiling of different cell types within organs. *Epigenomics* 8, 817–829
110. Rauluseviciute, I. *et al.* (2020) DNA hypermethylation associated with upregulated gene expression in prostate cancer demonstrates the diversity of epigenetic regulation. *BMC Med Genomics* 13, 6
111. Centers for Disease Control and Prevention (U.S.) (2019) *Antibiotic resistance threats in the United States, 2019*, Centers for Disease Control and Prevention (U.S.)
112. Fang, F.C. *et al.* (2016) Bacterial Stress Responses during Host Infection. *Cell Host Microbe* 20, 133–143
113. Sanfilippo, J.E. *et al.* (2019) Microfluidic-based transcriptomics reveal force-independent bacterial rheosensing. *Nat Microbiol* 4, 1274–1281
114. Segal, A.W. (2005) How neutrophils kill microbes. *Annu Rev Immunol* 23, 197–223

115. Hampton, M.B. *et al.* (1998) Inside the neutrophil phagosome: oxidants, myeloperoxidase, and bacterial killing. *Blood* 92, 3007–3017
116. Fang, F.C. (2011) Antimicrobial actions of reactive oxygen species. *mBio* 2
117. Gray, M.J. *et al.* (2013) Bacterial responses to reactive chlorine species. *Annu Rev Microbiol* 67, 141–160
118. Estrela, C. *et al.* (2003) Antimicrobial effect of 2% sodium hypochlorite and 2% chlorhexidine tested by different methods. *Braz Dent J* 14, 58–62
119. Albrich, J.M. and Hurst, J.K. (1982) Oxidative inactivation of Escherichia coli by hypochlorous acid. Rates and differentiation of respiratory from other reaction sites. *FEBS Lett* 144, 157–161
120. Harrison, J.E. and Schultz, J. (1976) Studies on the chlorinating activity of myeloperoxidase. *J Biol Chem* 251, 1371–1374
121. Jensen, E.T. *et al.* (1990) Human polymorphonuclear leukocyte response to Pseudomonas aeruginosa grown in biofilms. *Infect Immun* 58, 2383–2385
122. Potvin, E. *et al.* (2003) In vivo functional genomics of Pseudomonas aeruginosa for high-throughput screening of new virulence factors and antibacterial targets. *Environ Microbiol* 5, 1294–1308
123. Cornforth, D.M. *et al.* (2018) Pseudomonas aeruginosa transcriptome during human infection. *Proc Natl Acad Sci U S A* 115, E5125–E5134
124. Winsor, G.L. *et al.* (2016) Enhanced annotations and features for comparing thousands of Pseudomonas genomes in the Pseudomonas genome database. *Nucleic Acids Res* 44, D646-653
125. Boechat, A.L. *et al.* (2013) A novel role for an ECF sigma factor in fatty acid biosynthesis and membrane fluidity in Pseudomonas aeruginosa. *PLoS One* 8, e84775
126. Malke, H. (1993) Jeffrey H. Miller, A Short Course in Bacterial Genetics – A Laboratory Manual and Handbook forEscherichia coli and Related Bacteria. Cold Spring Harbor 1992. Cold Spring Harbor Laboratory Press. ISBN: 0–87969-349–5. *J Basic Microbiol* 33, 278–278
127. Doolin, T. *et al.* (2020) Mammalian histones facilitate antimicrobial synergy by disrupting the bacterial proton gradient and chromosome organization. *Nat Commun* 11, 3888
128. Clark, H.L. *et al.* (2018) Protein Deiminase 4 and CR3 Regulate Aspergillus fumigatus and β-Glucan-Induced Neutrophil Extracellular Trap Formation, but Hyphal Killing Is Dependent Only on CR3. *Front Immunol* 9, 1182
129. Dypbukt, J.M. *et al.* (2005) A sensitive and selective assay for chloramine production by myeloperoxidase. *Free Radic Biol Med* 39, 1468–1477
130. Karlsson, A. *et al.* (2000) Phorbol myristate acetate induces neutrophil NADPH-oxidase activity by two separate signal transduction pathways: dependent or independent of phosphatidylinositol 3-kinase. *J Leukoc Biol* 67, 396–404
131. Farrant, K.V. *et al.* (2020) Response of Pseudomonas aeruginosa to the Innate Immune System-Derived Oxidants Hypochlorous Acid and Hypothiocyanous Acid. *J Bacteriol* 203, e00300-20
132. Winterbourn, C.C. (1985) Comparative reactivities of various biological compounds with myeloperoxidase-hydrogen peroxide-chloride, and similarity of the oxidant to hypochlorite. *Biochim Biophys Acta* 840, 204–210

133. Hawkins, C.L. *et al.* (2003) Hypochlorite-induced oxidation of amino acids, peptides and proteins. *Amino Acids* 25, 259–274
134. Pattison, D.I. and Davies, M.J. (2006) Reactions of myeloperoxidase-derived oxidants with biological substrates: gaining chemical insight into human inflammatory diseases. *Curr Med Chem* 13, 3271–3290
135. Atmaca, G. (2004) Antioxidant effects of sulfur-containing amino acids. *Yonsei Med J* 45, 776–788
136. Bin, P. *et al.* (2017) Oxidation Resistance of the Sulfur Amino Acids: Methionine and Cysteine. *Biomed Res Int* 2017, 9584932
137. Seaver, L.C. and Imlay, J.A. (2001) Alkyl hydroperoxide reductase is the primary scavenger of endogenous hydrogen peroxide in Escherichia coli. *J Bacteriol* 183, 7173–7181
138. Brown, S.M. *et al.* (1995) Cloning and characterization of the katB gene of Pseudomonas aeruginosa encoding a hydrogen peroxide-inducible catalase: purification of KatB, cellular localization, and demonstration that it is essential for optimal resistance to hydrogen peroxide. *J Bacteriol* 177, 6536–6544
139. Farrant, K.V. *et al.* (2020) Response of Pseudomonas aeruginosa to the Innate Immune System-Derived Oxidants Hypochlorous Acid and Hypothiocyanous Acid. *J Bacteriol* 203, e00300-20
140. Skurnik, D. *et al.* (2013) A comprehensive analysis of in vitro and in vivo genetic fitness of Pseudomonas aeruginosa using high-throughput sequencing of transposon libraries. *PLoS Pathog* 9, e1003582
141. Hou, A.-M. *et al.* (2019) Chlorine injury enhances antibiotic resistance in Pseudomonas aeruginosa through over expression of drug efflux pumps. *Water Res* 156, 366–371
142. Jin, M. *et al.* (2020) Chlorine disinfection promotes the exchange of antibiotic resistance genes across bacterial genera by natural transformation. *ISME J* 14, 1847–1856
143. Utomo, L. *et al.* (2016) Cartilage inflammation and degeneration is enhanced by pro-inflammatory (M1) macrophages in vitro, but not inhibited directly by anti-inflammatory (M2) macrophages. *Osteoarthritis Cartilage* 24, 2162–2170
144. Kaikkonen, M.U. *et al.* (2013) Remodeling of the enhancer landscape during macrophage activation is coupled to enhancer transcription. *Mol Cell* 51, 310–325
145. Ghisletti, S. *et al.* (2010) Identification and characterization of enhancers controlling the inflammatory gene expression program in macrophages. *Immunity* 32, 317–328
146. Heinz, S. *et al.* (2010) Simple combinations of lineage-determining transcription factors prime cis-regulatory elements required for macrophage and B cell identities. *Mol Cell* 38, 576–589
147. Urban, L.A. *et al.* (2021) The impact of age-related hypomethylated DNA on immune signaling upon cellular demise. *Trends in Immunology* 42, 464–468
148. Deptuch, T. *et al.* (2022) In vivo study of the immune response to bioengineered spider silk spheres. *Sci Rep* 12, 13480
149. Bygd, H.C. *et al.* (2014) The significance of macrophage phenotype in cancer and biomaterials. *Clin Transl Med* 3, 62
150. Kim, Y.K. *et al.* (2016) Biomolecular strategies to modulate the macrophage response to implanted materials. *J. Mater. Chem. B* 4, 1600–1609

151. Jin, F. *et al.* (2021) Targeting epigenetic modifiers to reprogramme macrophages in non-resolving inflammation-driven atherosclerosis. *Eur Heart J Open* 1, oeab022
152. Qin, W. *et al.* (2021) Role of Myeloid Tet Methylcytosine Dioxygenase 2 in Pulmonary and Peritoneal Inflammation Induced by Lipopolysaccharide and Peritonitis Induced by Escherichia coli. *Cells* 11, 82
153. Previtera, M.L. and Sengupta, A. (2015) Substrate Stiffness Regulates Proinflammatory Mediator Production through TLR4 Activity in Macrophages. *PLoS One* 10, e0145813
154. Meli, V.S. *et al.* (2020) YAP-mediated mechanotransduction tunes the macrophage inflammatory response. *Sci Adv* 6, eabb8471
155. Blakney, A.K. *et al.* (2012) The effects of substrate stiffness on the in vitro activation of macrophages and in vivo host response to poly(ethylene glycol)-based hydrogels. *J Biomed Mater Res A* 100, 1375–1386
156. Wang, J. *et al.* (2022) Matrix stiffness exacerbates the proinflammatory responses of vascular smooth muscle cell through the DDR1-DNMT1 mechanotransduction axis. *Bioact Mater* 17, 406–424
157. Ponnaluri, V.K.C. *et al.* (2017) Association of 5-hydroxymethylation and 5-methylation of DNA cytosine with tissue-specific gene expression. *Epigenetics* 12, 123–138
158. Dieckmann, L. *et al.* (2022) Reliability of a novel approach for reference-based cell type estimation in human placental DNA methylation studies. *Cell Mol Life Sci* 79, 115
159. Chakravarthy, A. *et al.* (2018) Pan-cancer deconvolution of tumour composition using DNA methylation. *Nat Commun* 9, 3220
160. Arneson, D. *et al.* (2020) MethylResolver-a method for deconvoluting bulk DNA methylation profiles into known and unknown cell contents. *Commun Biol* 3, 422
161. Houseman, E.A. *et al.* (2016) Reference-free deconvolution of DNA methylation data and mediation by cell composition effects. *BMC Bioinformatics* 17, 259
162. Farrant, K.V. *et al.* (2020) Response of Pseudomonas aeruginosa to the Innate Immune System-Derived Oxidants Hypochlorous Acid and Hypothiocyanous Acid. *J Bacteriol* 203, e00300-20
163. Fargier, E. *et al.* (2012) MexT Functions as a Redox-Responsive Regulator Modulating Disulfide Stress Resistance in Pseudomonas aeruginosa. *J Bacteriol* 194, 3502–3511
164. Rodríguez-Rojas, A. *et al.* (2020) Non-lethal exposure to H2O2 boosts bacterial survival and evolvability against oxidative stress. *PLoS Genet* 16, e1008649